

**A CONTINUUM THEORY OF MULTIPHASE MIXTURES FOR
MODELLING BIOLOGICAL GROWTH**

by
Harish Narayanan

A dissertation submitted in partial fulfillment
of the requirements for the degree of
Doctor of Philosophy
(Mechanical Engineering and Scientific Computing)
in The University of Michigan
2007

Doctoral Committee:

Associate Professor Krishnakumar R. Garikipati, Chair
Professor Ellen M. Arruda
Professor Karl Grosh
Associate Professor Trachette L. Jackson

“The truth of a theory is in your mind, not in your eyes.”

— Albert Einstein

© Harish Narayanan
2007

TABLE OF CONTENTS

LIST OF FIGURES	iv
LIST OF TABLES	vi
LIST OF APPENDICES	vii
CHAPTER	
1. Introduction	1
1.1 Background	1
1.2 An overview	3
2. A Lagrangian perspective	7
2.1 Balance laws for an open mixture	7
2.1.1 Balance of mass	9
2.1.2 Balance of linear momentum	11
2.1.3 Balance of angular momentum	14
2.1.4 Balance of energy	16
2.2 The kinematics of growth	20
2.2.1 Saturation and tissue swelling	22
2.3 The entropy inequality and its restrictions on constitutive relations	25
2.3.1 Thermodynamically-consistent constitutive framework	26
2.3.2 An anisotropic network model	29
2.3.3 A nearly incompressible ideal fluid	31
2.3.4 Driving forces for fluid flux	34
2.3.5 Saturation and Fickian diffusion	36
2.3.6 Solute transport	37
2.3.7 Nature of the sources	38
2.4 Algorithmic considerations	41
2.4.1 The role of mass balance in the current configuration	41
2.4.2 Incompressible fluid in a porous solid	43
3. Representative numerical simulations – I	48

3.1	Introducing the computational model	48
3.2	A multiphasic problem based on enzyme-kinetics	51
3.3	Examples exploring the biphasic nature of porous soft tissue	56
3.3.1	The tendon under constriction	56
3.3.2	A swelling problem	65
4.	An Eulerian perspective	69
4.1	Balance laws for an open mixture	70
4.1.1	Balance of mass	71
4.1.2	Balance of linear momentum	73
4.1.3	Balance of angular momentum	75
4.1.4	Balance of energy	77
4.2	Thermodynamically-consistent constitutive framework	80
4.2.1	The Clausius-Duhem form	81
4.2.2	Duhamel’s law of heat conduction	83
4.2.3	Energy-dependent mass source terms	84
4.2.4	A viscoelastic solid	87
4.2.5	Effects of the stress state on tissue growth	91
4.2.6	A Newtonian fluid	92
4.2.7	Frictional interaction forces	94
4.2.8	Diffusive solute fluxes	95
5.	Representative numerical simulations – II	96
5.1	Introducing the computational model	97
5.2	Some simple physical tests	99
5.2.1	An inflating balloon	100
5.2.2	The tissue under constriction	106
5.3	Examples exploring the biphasic nature of porous soft tissues	112
5.3.1	Stress relaxation	114
5.3.2	Hysteresis in the cyclic stress-strain response	117
5.4	Mechanics and the growing tumour	122
5.4.1	Kinematic swelling concomitant with growth	123
5.4.2	A constraining wall and soft contact mechanics	124
5.4.3	The mechanics of the cells	128
5.4.4	The transport of the cells	130
5.4.5	Coupling the phenomena	136
6.	Concluding remarks	141
	APPENDICES	143
	BIBLIOGRAPHY	150

LIST OF FIGURES

Figure

2.1	The tissue idealised as a continuous medium.	8
2.2	Interaction forces, traction and body loads on the tissue.	11
2.3	Energetic interactions the tissue is subject to.	17
2.4	The kinematics of growth.	21
2.5	Stages of tissue saturation.	23
2.6	The eight-chain model incorporating worm-like chains.	32
2.7	Saturation depicted at a microscopic scale.	36
2.8	Growth and strengthening under biochemical influences.	39
2.9	Growth and strengthening under mechanical influences.	40
2.10	Pore structure at the boundary deforming with the tissue.	42
2.11	Spatial oscillations in the numerical solution ($Pe = 100$).	44
2.12	Smooth solution from a stabilised method ($Pe = 100$).	47
3.1	Engineered tendon construct (Calve et al., 2004).	51
3.2	The finite element mesh used in the computations.	52
3.3	Variation of the collagen source with solute concentration.	53
3.4	Constrictive load applied to the tendon immersed in a bath.	54
3.5	The solute concentration (kg.m^{-3}) initially.	55
3.6	The collagen concentration (kg.m^{-3}) at time $t = 5 \times 10^{-2}$ s.	56
3.7	Upper bound model from strain homogenisation.	57
3.8	Upper bound vertical fluid flux ($\text{kg.m}^{-2}.\text{s}^{-1}$) at $t = 1$ s.	58
3.9	Reference fluid concentration (kg.m^{-3}) at time $t = 1$ s.	59
3.10	Relaxation of the top face of the tendon after constriction.	60
3.11	Lower bound model from stress homogenisation.	61
3.12	Lower bound vertical fluid flux ($\text{kg.m}^{-2}.\text{s}^{-1}$) at $t = 1$ s.	61
3.13	The initial collagen concentration (kg.m^{-3}).	65
3.14	The collagen concentration (kg.m^{-3}) after 1800 s.	66
3.15	The stress (Pa) vs stretch curves before and after growth.	67
3.16	The tensile response of tendon constructs (Arruda et al., 2005).	67
3.17	The volume of the tendon (m^3) evolving with time.	68
4.1	An Eulerian point of view.	70
4.2	A thermodynamically-motivated collagen source.	86
5.1	A representative finite element mesh used in the computations.	97
5.2	The inflating balloon at time $t = 0$ s.	103
5.3	The inflating balloon at time $t = 0.6$ s.	103

5.4	The inflating balloon at time $t = 1.2$ s.	104
5.5	The inflating balloon at time $t = 1.8$ s.	104
5.6	The inflating balloon at time $t = 2.4$ s.	105
5.7	The inflating balloon at time $t = 3.0$ s.	105
5.8	The displacement condition on the vertical edges of the tissue.	106
5.9	The constricted tissue at time $t = 0$ s.	108
5.10	The constricted tissue at time $t = 0.32$ s.	108
5.11	The constricted tissue at time $t = 0.66$ s.	109
5.12	The constricted tissue at time $t = 1.0$ s.	109
5.13	The constricted tissue at time $t = 2.0$ s.	110
5.14	The constricted tissue at time $t = 3.0$ s.	110
5.15	Dynamic evolution of the vertical fluid velocity.	111
5.16	Quasistatic evolution of the vertical fluid velocity.	111
5.17	Mechanical response of an explanted ligament (Ma, 2007).	113
5.18	Quasistatic poroelastic model, $\dot{\epsilon} = 0.01$ Hz, $D = 1.037$ MPa.s.mm ⁻²	116
5.19	Quasistatic poroelastic model, $\dot{\epsilon} = 0.02$ Hz, $D = 1.037$ MPa.s.mm ⁻²	116
5.20	Dynamic viscoelastic model, $\dot{\epsilon} = 0.02$ Hz, $\tau = 0.3$ s.	117
5.21	Quasistatic poroelastic model, $\dot{\epsilon} = 0.01$ Hz, $D = 1.037$ MPa.s.mm ⁻²	119
5.22	Dynamic poroelastic model, $\bar{\dot{\epsilon}} = 0.01$ Hz, $D = 1.037$ MPa.s.mm ⁻²	120
5.23	Dynamic poroelastic model, $\bar{\dot{\epsilon}} = 0.001$ Hz, $D = 1.037$ MPa.s.mm ⁻²	120
5.24	Dynamic poroelastic model, $\bar{\dot{\epsilon}} = 0.01$ Hz, $D = 10.37$ MPa.s.mm ⁻²	121
5.25	Dynamic viscoelastic model, $\dot{\epsilon} = 0.01$ Hz, $\tau = 0.3$ s.	121
5.26	A semicircular tumour at time $t = 0$ days.	124
5.27	A semicircular tumour at time $t = 100$ days.	125
5.28	The area of the tumour evolving over 100 days.	125
5.29	The growing tumour constrained by a wall at time $t = 120$ days.	127
5.30	The horizontal stress in the tumour evolving over 120 days.	127
5.31	Homogeneous inward pull due to a uniform distribution of cells.	129
5.32	Heterogeneous traction due to a non-uniform distribution of cells.	129
5.33	The cells diffusing and proliferating at time $t = 0$ days.	131
5.34	The cells diffusing and proliferating at time $t = 33$ days.	131
5.35	The cells diffusing and proliferating at time $t = 67$ days.	132
5.36	The cells diffusing and proliferating at time $t = 100$ days.	132
5.37	Heterogeneous extra-cellular matrix concentration (kg.m ⁻³).	133
5.38	Proliferating cells undergoing haptotaxis at time $t = 0$ days.	134
5.39	Proliferating cells undergoing haptotaxis at time $t = 33$ days.	134
5.40	Proliferating cells undergoing haptotaxis at time $t = 67$ days.	135
5.41	Proliferating cells undergoing haptotaxis at time $t = 100$ days.	135
5.42	A constrained growing tumour at $t = 0$ days.	137
5.43	A constrained growing tumour at $t = 20$ days.	138
5.44	A constrained growing tumour at $t = 40$ days.	138
5.45	A constrained growing tumour at $t = 60$ days.	139
5.46	A constrained growing tumour at $t = 80$ days.	139
5.47	A constrained growing tumour at $t = 100$ days.	140
5.48	An unconstrained growing tumour at $t = 80$ days.	140

LIST OF TABLES

Table

3.1	Material parameters used in the analysis.	53
3.2	Mechanics equation residual norms.	63
5.1	Material parameters used in the analysis.	113

LIST OF APPENDICES

Appendix

A.	A review of mathematical results	144
	A.1 Gauss-Green's divergence theorem	144
	A.2 Reynolds' transport theorem	145
B.	Supplementary topics	148
	B.1 Frame invariance and flux contribution from acceleration	148
	B.2 Stabilisation of the simplified solute transport equation	149

CHAPTER 1

Introduction

This dissertation presents a continuum treatment of growth in biological tissue developed within the context of modern mixture theory. The crux of this work is a careful examination of the assumptions underlying continuum thermodynamics under the condition that multiple interacting species occupy a region of Euclidean space simultaneously. The formal axiomatic treatment presented derives from these assumptions, and provides insight into the sequence of interactions among tissue mechanics, mass transport and biochemical reactions. A computational formulation built upon the theory is used to solve a broad class of numerical examples demonstrating several biophysical aspects of tissue growth.

This initial chapter provides some context for this work (Section 1.1) and an overview of the topics considered in the remainder of the dissertation (Section 1.2).

1.1 Background

Growth involves the addition or depletion of mass in biological tissue. Growth occurs in combination with *remodelling*, which is a change in microstructure, and possibly with *morphogenesis*, which is a change in form in the embryonic state. The physics of these processes are quite distinct, and for modelling purposes can, and must, be separated. In this work, biological growth is formulated on a continuum scale within the context of mixture theory (Truesdell and Toupin, 1960; Truesdell

and Noll, 1965; Bedford and Drumheller, 1983), which allows us to systematically account for the numerous interacting and inter-converting species constituting the tissue. The crux of this work is a careful examination of the assumptions underlying continuum thermodynamics for these mixtures, especially in the presence of supplementary terms which enhance the balance laws from classical mechanics to allow for the complex behaviour of tissues.

There have been a number of significant papers on biological growth (and remodelling), of which we touch upon some whose approaches are either similar to this work in some respects, or differ in important ways.

In the context of biological growth, the notion of a mass source was first introduced in Cowin and Hegedus (1976). Also recognising the importance of mass transport to the growth problem, Epstein and Maugin (2000) introduced a mass flux term to the corresponding transport equation. In their work, they also considered irreversible momentum and entropy contributions from the species flux to account for these aspects of the inter-species interactions, and deduce non-symmetric partial Cauchy stresses, in contrast to the treatment here. (See Sections 2.1.3 and 4.1.3.)

Humphrey and Rajagopal (2002) provided a mathematical treatment of *adaptation* in tissues, which includes growth and remodelling in the sense of this work. They introduced the notion of evolving natural configurations to model the state of material deposited at different instants in time. The treatment of the growth part of the deformation gradient in this work (Section 2.2) bears some resemblance to this idea. This concept also forms the basis for an active field of study within the literature (Skalak, 1981; Skalak et al., 1996; Klisch et al., 2001; Taber and Humphrey, 2001; Lubarda and Hoger, 2002; Ambrosi and Mollica, 2002) focusing on the kinematic aspects of biological growth.

Preziosi and Farina (2002) developed an extension to the classical Darcy’s Law to incorporate mass exchanges between reacting species. This consideration is relevant to growth problems; however, these issues were subsumed in Garikipati et al. (2004), upon which this work is based.

While most of the computational examples in this dissertation are presented in the context of modelling our primary tissues of interest, engineered tendon and ligament constructs (Calve et al., 2004; Ma, 2007), many of the general ideas presented in this work are applicable to modelling tumour growth. The ideas proposed are similar to tumour modelling work that account for mechanical effects (Jackson and Byrne, 2002; Byrne et al., 2006).

The form of the Clausius-Duhem inequality arrived at in Section 4.2 is equivalent to the forms in recent work on mixture theory-based models for biological growth (Loret and Simões, 2005; Ateshian, 2007). However, subsequently varying choices made in the different works, including this one, for the constitutive independent variables result in altered constitutive specification. Moreover, the constitutive choices detailed in this work ensure that the Clausius-Duhem inequality is satisfied *a priori*, are adequately general to handle a fairly large class of physics, and most significantly, have been implemented in a coupled formulation retaining much of their rich detail, as evidenced by the computational examples presented in Chapter 5.

1.2 An overview

The core of this dissertation is divided into two parts.

The first part, consisting of Chapters 2 and 3, develops the theoretical formulation for biological growth from a Lagrangian perspective and presents representative numerical examples demonstrating aspects of the coupled physics using a corre-

sponding computational implementation. This approach, based on our previous work (Garikipati et al., 2004), draws in some measure from Cowin and Hegedus (1976); Epstein and Maugin (2000) and Taber and Humphrey (2001), and works in terms of material quantities defined in the reference configuration of the tissue.

The theoretical treatment presented in Chapter 2 begins by deriving general balance equations governing the behaviour of multi-phase mixtures, and then proceeds to specify constitutive relationships pertinent to growing biological tissue that are thermodynamically-consistent, in the sense that specification of these relations does not violate the Clausius-Duhem dissipation inequality. Two important contributions of this work include a comprehensive account of the coupling between transport and mechanics (stemming from the balance equations, kinematics and constitutive relations), and an improvement to the mathematical treatment that allows for the numerical stabilisation of the advection-diffusion mass transport equation in the advection-dominated regime.

This approach was impaired by some basic deficiencies. Firstly, while the transport equations were posed (consistently) in the reference configuration, for a tissue undergoing finite strains, the physics of fluid-tissue interactions and the imposition of relevant boundary conditions is best understood and represented in the current configuration. Secondly, also stemming from its roots in solid mechanics, the formulation relied upon primitive quantities that are not natural to fluids, such as the *deformation gradient of the fluid*. While such quantities can be formally defined, they are not easily tracked during the course of solving boundary value problems. One final complication with this approach arose from attempting to impose the balance of momentum for the tissue as a whole, as this necessitated additional assumptions on the microstructural mechanics. Accurate modelling of the micromechanics requires

sophisticated homogenisation techniques (e.g., [Idiart and Castaneda \(2003\)](#)) and these assumptions have strong implications for the stiffness of tissue response, the nature of fluid transport, and since nutrients are dissolved in the fluid, ultimately for growth. This meant that without additional, complex, assumptions, the formulation could not provide precise, quantitative results. (The calculations in [Section 3.3.1](#), however, do determine the upper and lower bounds of the solutions.)

It is these drawbacks in the Lagrangian formulation that motivate the work presented in the second half of this dissertation, composed of [Chapters 4 and 5](#).

[Chapter 4](#) is a reflection of our current understanding of the system that has evolved over these past few years. Recognising that the tissue is composed of many phases that undergo long-range transport, the formulation is rederived from an Eulerian perspective; the viewpoint used for formulating the basic laws of fluid mechanics.

In this approach, the balance equations are derived in the current configuration of the tissue in terms of spatial variables enabling a straightforward application of physically-relevant boundary conditions; but more importantly, the governing equations for the fluid phase are recast in terms of primitive variables that are more natural to fluid mechanics: the fluid velocity and pressure. Another significant aspect of this work is that, upon revisiting the Clausius-Duhem inequality in terms of spatial variables, appropriate constitutive choices are made to ensure that the inequality is satisfied a priori.

Accompanying this revised formulation is an improved computational framework, now designed to solve the *detailed* set of momentum balance equations, i.e., for each species separately, eliminating the need for the micromechanics assumptions mentioned earlier. A brief discussion of this framework, along with selected computational examples, is the subject of [Chapter 5](#). This coupled implementation demon-

strates several basic aspects of the physics of biphasic non-reacting mixtures, has been tailored to closely study aspects of the experimentally observed mechanics of ligaments, and has been extended in a straightforward manner to a substantially different class of problem: modelling tumour growth, as evidenced by the examples in Chapter 5.

The computational framework thus furnishes a powerful tool that can possibly be tailored to answer specific questions—ranging from those pertinent to viscoelastic aspects of the mechanical response of growing tendons under different loading conditions, to quantitative investigations of the efficacy of drugs based on how they are administered, to understanding the cellular processes associated with tumour growth.

CHAPTER 2

A Lagrangian perspective

Tracing its origins to mechanics theories for solid continua, the following formulation for biological growth is developed naturally in terms of *material quantities* defined in the *reference configuration* of the tissue. During the course of this chapter, the fundamental field equations of a continuum idealisation of tissues are derived from general principles governing the behaviour of multiphase mixtures. Specifically, Section 2.1 helps define the system and formally introduces fundamental quantities characterising it, before deriving the balance laws from fundamental axioms. Section 2.2 presents the kinematics associated with finite deformation growth. A fundamental axiom of Thermodynamics, the entropy inequality, and the restrictions it places on functional forms of constitutive relationships is the subject of Section 2.3. The chapter concludes with key algorithmic considerations (Section 2.4) which play an important role in the computational formulation underlying the numerical experiments presented in Chapter 3.

2.1 Balance laws for an open mixture

The tissue of interest is idealised as an open subset of \mathbb{R}^3 with a piecewise smooth boundary. At a reference placement of the tissue, Ω_0 , points in the tissue are identified by their reference positions, $\mathbf{X} \in \Omega_0$. The motion of the tissue is a sufficiently smooth bijective map $\varphi : \bar{\Omega}_0 \times [0, T] \rightarrow \mathbb{R}^3$, where $\bar{\Omega}_0 := \overline{\Omega_0 \cup \partial\Omega_0}$; $\partial\Omega_0$ being

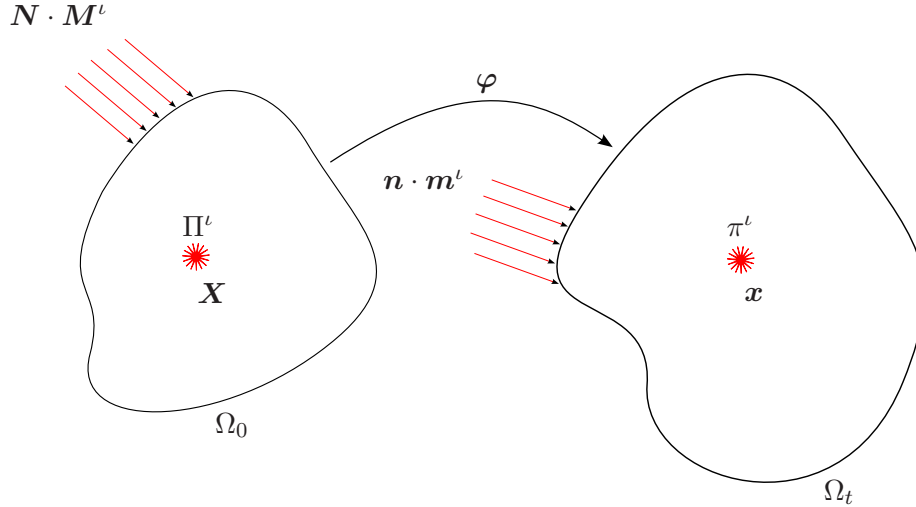


Figure 2.1: The tissue idealised as a continuous medium.

the boundary of Ω_0 . At a typical time instant $t \in [0, T]$, $\varphi(\mathbf{X}, t)$ maps a point \mathbf{X} to its current position, \mathbf{x} . In its current configuration, the tissue occupies a region $\Omega_t = \varphi_t(\Omega_0)$. These details are depicted in Figure 2.1. The deformation gradient $\mathbf{F} := \partial\varphi/\partial\mathbf{X}$ is the tangent map of φ .

The tissue consists of numerous species, of which the following groupings are of importance for the models: A solid species, consisting of solid *collagen fibrils* and *cells*,¹ denoted by c , an extra-cellular *fluid* species, denoted by f , consisting primarily of water, and *solute* species, consisting of precursors to reactions, byproducts, nutrients, and other regulatory chemicals. A generic solute will be denoted by s . In the treatment that follows, an arbitrary species will be denoted by ι , where $\iota = c, f, s$.

The fundamental quantities of interest are mass concentrations, $\rho_0^\iota(\mathbf{X}, t)$. These are the masses of each species per unit system volume in Ω_0 . Formally, these quantities can also be thought of in terms of the maps $\rho_0^\iota : \bar{\Omega}_0 \times [0, T] \rightarrow \mathbb{R}$, upon which the formulation imposes some smoothness requirements. By definition, the total *mate-*

¹At this point, the solid species is not differentiated any further. This is a good approximation to the physiological setting for tendons, which are relatively acellular and whose dry mass consists of up to 75% collagen (Nordin et al., 2001). When modelling tumour growth in a later chapter (Section 5.4), where cell mechanics and migration are significant (Namy et al., 2004), the solid phase is further distinguished.

rial density of the tissue at a point is a summation of these concentrations over all species $\sum_{\iota} \rho_0^{\iota} = \rho_0$.

The system is open with respect to mass. Other than the solid species, c , all phases have mass fluxes, \mathbf{M}^{ι} .² These are mass flow rates per unit cross-sectional area in the reference configuration *defined relative to the solid phase*. The species have mass sources (or sinks), Π^{ι} . The sources specify mass production rates per unit volume of the body in its reference configuration, Ω_0 .

2.1.1 Balance of mass

As a result of mass transport (via the flux terms) and inter-conversion of species (via the source/sink terms) introduced above, the concentrations, ρ_0^{ι} , change with time. Written in integral form, the balance of mass for an arbitrary species over Ω_0 states

$$(2.1) \quad \underbrace{\frac{d}{dt} \int_{\Omega_0} \rho_0^{\iota}(\mathbf{X}, t) dV}_{\text{Rate of change of mass}} = \underbrace{\int_{\Omega_0} \Pi^{\iota}(\mathbf{X}, t) dV}_{\text{Mass being created}} - \underbrace{\int_{\partial\Omega_0} \mathbf{M}^{\iota}(\mathbf{X}, t) \cdot \mathbf{N} dA}_{\text{Mass leaving the domain}},$$

where \mathbf{N} is the unit outward normal to the boundary, $\partial\Omega_0$.

Applying Gauss' Divergence Theorem (Appendix A.1) to the surface integral term, and localising the result (recalling that since Ω_0 is a fixed volume, the time derivative on the first term can be simply moved into the integral), we arrive at the following local form of the balance of mass for an arbitrary species in the reference configuration,

²As previously mentioned, when modelling certain physiological processes such as tumour growth or wound healing, where migration of cells within the extra-cellular matrix is consequential, the solid phase is further differentiated and cell migration is modelled as mass transport.

$$(2.2) \quad \frac{\partial \rho_0^\iota}{\partial t} = \Pi^\iota - \text{DIV}[\mathbf{M}^\iota], \quad \forall \iota.$$

Here, $\text{DIV}[\bullet]$ is the divergence operator in the reference configuration. The functional forms of Π^ι are abstractions of the underlying biochemistry; physiologically relevant examples of which are discussed in Section 2.3.7. The fluxes, \mathbf{M}^ι , are determined from the thermodynamically-motivated constitutive relations described in Section 2.3.4. Recall that, in particular, $\mathbf{M}^c = \mathbf{0}$.

The sources, Π^ι for various species, satisfy a relation $\sum_\iota \Pi^\iota = 0$, which is derived as follows. Firstly, summing Equation (2.1) over all species leads to the law of mass balance for the system,

$$(2.3) \quad \frac{d}{dt} \sum_\iota \int_{\Omega_0} \rho_0^\iota dV = \sum_\iota \int_{\Omega_0} \Pi^\iota dV - \sum_\iota \int_{\partial\Omega_0} \mathbf{M}^\iota \cdot \mathbf{N} dA.$$

An alternate way of arriving at the mass balance equation for the system is to envision an external observer accounting only for the fluxes at the boundary, not aware of any processes internal to the system. Following this viewpoint, we neglect the interconversion terms (sources/sinks) which exist within the system, and arrive at,

$$(2.4) \quad \frac{d}{dt} \sum_\iota \int_{\Omega_0} \rho_0^\iota dV = - \sum_\iota \int_{\partial\Omega_0} \mathbf{M}^\iota \cdot \mathbf{N} dA.$$

Comparing the equivalent forms (2.3) and (2.4), it emerges (upon localisation) that the sources and sinks satisfy

$$(2.5) \quad \sum_\iota \Pi^\iota = 0,$$

a conclusion that is consistent with classical mixture theory (Truesdell and Noll, 1965) in the absence of a net production term for the system.

2.1.2 Balance of linear momentum

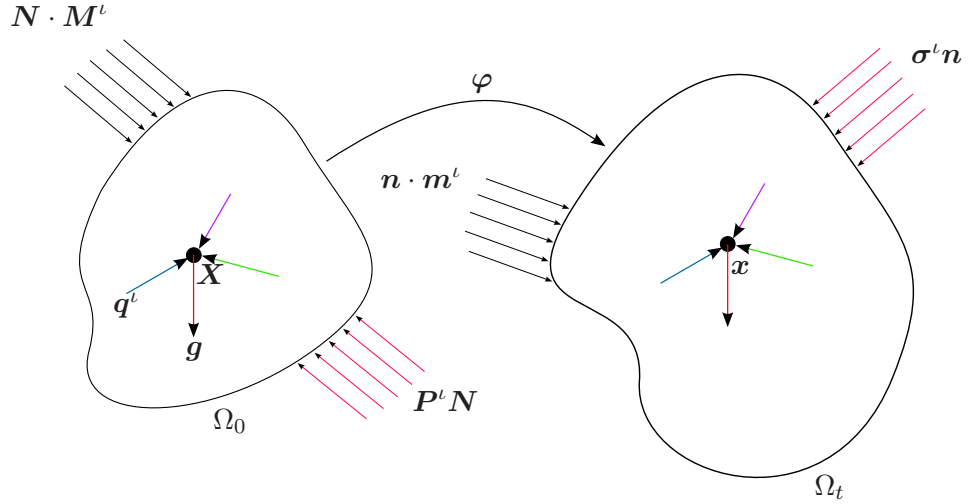


Figure 2.2: Interaction forces, traction and body loads on the tissue.

In soft tissues, the species production rate and flux that appear on the right hand-side in Equation (2.2) are strongly dependent on the local state of stress. To correctly model this coupling, the balance of linear momentum should be solved to determine the local state of strain and stress.

Recall that the deformation of the tissue is characterised by the map $\varphi(\mathbf{X}, t)$. Since we are working under the assumption that the solid collagen fibrils and fibroblasts do not undergo mass transport, the material velocity of this species, $\mathbf{V} = \partial\varphi/\partial t$, is used as the primitive variable for mechanics. Each remaining species can undergo mass transport relative to the solid collagen. For this purpose, it is useful to define the material velocity of a species ι relative to the solid phase as: $\mathbf{V}^\iota = (1/\rho_0^\iota)\mathbf{F}\mathbf{M}^\iota$. Thus, the total material velocity of a species ι is $\mathbf{V} + \mathbf{V}^\iota$.

The tissue is subjected to a surface traction, \mathbf{T} , and a body force per unit mass, \mathbf{g} . We define the partial first Piola-Kirchhoff stress tensor corresponding to species ι as

the portion of the total stress borne by the species. Denoting this quantity by \mathbf{P}^ι , the natural boundary condition then implies that $\mathbf{T} = \sum_\iota \mathbf{P}^\iota \mathbf{N}$ on $\partial\Omega_0$. Thus, $\mathbf{P}^\iota \mathbf{N}$ is the corresponding partial traction, as depicted in Figure 2.2.

Recognising that the concentrations of solutes are low, and consequently that they do not bear appreciable stress, the partial stresses and momentum balance equations are defined only for the solid collagen and fluid phases. Written in integral form, the balance of momentum of species ι over Ω_0 is,

$$(2.6) \quad \underbrace{\frac{d}{dt} \int_{\Omega_0} \rho_0^\iota (\mathbf{V} + \mathbf{V}^\iota) dV}_{\text{Rate of change of momentum}} = \underbrace{\int_{\Omega_0} \rho_0^\iota \mathbf{g} dV + \int_{\Omega_0} \rho_0^\iota \mathbf{q}^\iota dV}_{\text{Resultant body force}} + \underbrace{\int_{\Omega_0} \Pi^\iota (\mathbf{V} + \mathbf{V}^\iota) dV}_{\text{Momentum being created}} \\ + \underbrace{\int_{\partial\Omega_0} \mathbf{P}^\iota \mathbf{N} dA}_{\text{Boundary traction}} - \underbrace{\int_{\partial\Omega_0} (\mathbf{V} + \mathbf{V}^\iota) \mathbf{M}^\iota \cdot \mathbf{N} dA}_{\text{Momentum leaving the domain}},$$

where \mathbf{q}^ι is the force per unit mass exerted upon ι by the other species present. Note the contributions of the mass source distributed through the volume and the influx over the boundary to the rate of change of momentum in Equation (2.6).

Writing $(\mathbf{V} + \mathbf{V}^\iota) \mathbf{M}^\iota \cdot \mathbf{N}$ as $((\mathbf{V} + \mathbf{V}^\iota) \otimes \mathbf{M}^\iota) \mathbf{N}$, and using Gauss' Divergence Theorem (Appendix A.1), one obtains:

$$\int_{\Omega_0} \left(\frac{\partial \rho_0^\iota}{\partial t} (\mathbf{V} + \mathbf{V}^\iota) + \rho_0^\iota \frac{\partial}{\partial t} (\mathbf{V} + \mathbf{V}^\iota) \right) dV = \int_{\Omega_0} \rho_0^\iota (\mathbf{g} + \mathbf{q}^\iota) dV \\ + \int_{\Omega_0} (\Pi^\iota (\mathbf{V} + \mathbf{V}^\iota) + \text{DIV}[\mathbf{P}^\iota]) dV \\ - \int_{\Omega_0} \text{DIV} [(\mathbf{V} + \mathbf{V}^\iota) \otimes \mathbf{M}^\iota] dV.$$

Applying the product rule to the last term and using the mass balance equation (2.2)

gives

$$\begin{aligned} \int_{\Omega_0} \rho_0^\iota \frac{\partial}{\partial t} (\mathbf{V} + \mathbf{V}^\iota) dV &= \int_{\Omega_0} \rho_0^\iota (\mathbf{g} + \mathbf{q}^\iota) dV \\ &+ \int_{\Omega_0} (\text{DIV} [\mathbf{P}^\iota] - (\text{GRAD} [\mathbf{V} + \mathbf{V}^\iota]) \mathbf{M}^\iota) dV, \end{aligned}$$

where $\text{GRAD}[\bullet]$ is the gradient operator in the reference configuration. Localising this result gives the balance of linear momentum for a single species in Ω_0 :

$$(2.7) \quad \begin{aligned} \rho_0^\iota \frac{\partial}{\partial t} (\mathbf{V} + \mathbf{V}^\iota) &= \rho_0^\iota (\mathbf{g} + \mathbf{q}^\iota) + \text{DIV}[\mathbf{P}^\iota] \\ &- (\text{GRAD} [\mathbf{V} + \mathbf{V}^\iota]) \mathbf{M}^\iota, \quad \iota = \text{c, f}. \end{aligned}$$

The final term with the gradient of total species velocity identifies the contribution of the flux to the balance of momentum. In practise, when the relative magnitude of the fluid mobility (and hence flux) is small, the final term on the right hand-side of Equation (2.7) is negligible, resulting in a more classical form of the balance of momentum. Furthermore, in the absence of significant acceleration of the tissue during growth, the left hand-side can also be neglected, reducing (2.7) to the quasi-static balance of linear momentum.

The interaction forces, \mathbf{q}^ι , satisfy a relation with the mass sources, Π^ι , that is elucidated by the following argument. One way of arriving at the balance of momentum of the entire tissue is by summing Equation (2.6) over $\iota = \text{c, f}$

$$(2.8) \quad \begin{aligned} \sum_\iota \frac{d}{dt} \int_{\Omega_0} \rho_0^\iota (\mathbf{V} + \mathbf{V}^\iota) dV &= \sum_\iota \int_{\Omega_0} \rho_0^\iota \mathbf{g} dV + \sum_\iota \int_{\Omega_0} \rho_0^\iota \mathbf{q}^\iota dV \\ &+ \sum_\iota \int_{\Omega_0} \Pi^\iota (\mathbf{V} + \mathbf{V}^\iota) dV + \sum_\iota \int_{\partial\Omega_0} \mathbf{P}^\iota \mathbf{N} dA \\ &- \sum_\iota \int_{\partial\Omega_0} (\mathbf{V} + \mathbf{V}^\iota) \mathbf{M}^\iota \cdot \mathbf{N} dA. \end{aligned}$$

As in Section 2.1.1, recall that for an external observer, the rate of change of momentum of the entire system is affected only by external agents, and is independent of internal interactions of any nature (\mathbf{q}^ι and Π^ι). This observation leads to the following equivalent expression for the rate of change of linear momentum of the system:

$$(2.9) \quad \sum_{\iota} \frac{d}{dt} \int_{\Omega_0} \rho_0^\iota (\mathbf{V} + \mathbf{V}^\iota) dV = \int_{\Omega_0} \rho_0 \mathbf{g} dV + \int_{\partial\Omega_0} \mathbf{P} \mathbf{N} dA - \sum_{\iota} \int_{\partial\Omega_0} (\mathbf{V} + \mathbf{V}^\iota) \mathbf{M}^\iota \cdot \mathbf{N} dA.$$

Here, $\mathbf{P} = \sum_{\iota} \mathbf{P}^\iota$ and $\rho_0 = \sum_{\iota} \rho_0^\iota$. Since both (2.8) and (2.9) represent the balance of linear momentum of the system, it follows upon inspection that:

$$\sum_{\iota} \int_{\Omega_0} \rho_0^\iota \mathbf{q}^\iota dV + \sum_{\iota} \int_{\Omega_0} \Pi^\iota (\mathbf{V} + \mathbf{V}^\iota) dV = 0,$$

which, upon localisation (recalling Equation (2.5)), leads to

$$(2.10) \quad \sum_{\iota} (\rho_0^\iota \mathbf{q}^\iota + \Pi^\iota \mathbf{V}^\iota) = 0,$$

a result that is also consistent with classical mixture theory (Truesdell and Noll, 1965).

2.1.3 Balance of angular momentum

The balance of angular momentum in a purely mechanical theory implies that the Cauchy stress is symmetric: $\boldsymbol{\sigma} = \boldsymbol{\sigma}^T$. This result is now examined in context of an open system comprising of multiple interacting and inter-converting species.

The balance of angular momentum about the origin of a species ι over Ω_0 , as observed from an inertial reference frame, requires,

$$\begin{aligned}
 \underbrace{\frac{d}{dt} \int_{\Omega_0} \boldsymbol{\varphi} \times \rho_0^\iota (\mathbf{V} + \mathbf{V}^\iota) dV}_{\text{Rate of change of angular momentum}} &= \underbrace{\int_{\Omega_0} \boldsymbol{\varphi} \times [\rho_0^\iota (\mathbf{g} + \mathbf{q}^\iota) + \Pi^\iota (\mathbf{V} + \mathbf{V}^\iota)] dV}_{\text{Moment from body forces and angular momentum being created}} \\
 (2.11) \quad &+ \underbrace{\int_{\partial\Omega_0} \boldsymbol{\varphi} \times (\mathbf{P}^\iota - (\mathbf{V} + \mathbf{V}^\iota) \otimes \mathbf{M}^\iota) \mathbf{N} dA}_{\text{Moment from traction and angular momentum leaving the domain}}
 \end{aligned}$$

Applying properties of the cross product, the product rule and Gauss' Divergence Theorem (Appendix A.1) gives

$$\begin{aligned}
 \int_{\Omega_0} \mathbf{V} \times \rho_0^\iota \mathbf{V}^\iota + \boldsymbol{\varphi} \times \left(\frac{\partial \rho_0^\iota}{\partial t} (\mathbf{V} + \mathbf{V}^\iota) + \rho_0^\iota \frac{\partial}{\partial t} (\mathbf{V} + \mathbf{V}^\iota) \right) dV = \\
 \int_{\Omega_0} \boldsymbol{\varphi} \times \rho_0^\iota (\mathbf{g} + \mathbf{q}^\iota + \Pi^\iota (\mathbf{V} + \mathbf{V}^\iota)) dV \\
 + \int_{\Omega_0} (\boldsymbol{\varphi} \times \text{DIV}[\mathbf{P}^\iota] - \boldsymbol{\varphi} \times (\text{GRAD}[\mathbf{V} + \mathbf{V}^\iota] \mathbf{M}^\iota)) dV \\
 - \int_{\Omega_0} (-\boldsymbol{\varphi} \times (\mathbf{V} + \mathbf{V}^\iota) \text{DIV}[\mathbf{M}^\iota]) dV \\
 - \int_{\Omega_0} \boldsymbol{\epsilon} : ((\mathbf{P}^\iota - (\mathbf{V} + \mathbf{V}^\iota) \otimes \mathbf{M}^\iota) \mathbf{F}^\text{T}) dV,
 \end{aligned}$$

where $\boldsymbol{\epsilon}$ is the permutation symbol, and $\boldsymbol{\epsilon} : \mathbf{A}$ is written as $\epsilon_{ijk} A_{jk} \mathbf{e}_i$ in indicial form for any second-order tensor \mathbf{A} ; \mathbf{e}_i being the i^{th} basis vector. Using the mass balance equation (2.2), and balance of linear momentum (2.7), we have

$$\int_{\Omega_0} \mathbf{V} \times \rho_0^\iota \mathbf{V}^\iota dV = - \int_{\Omega_0} \boldsymbol{\epsilon} : \left(\left(\mathbf{P}^\iota - (\mathbf{V} + \mathbf{V}^\iota) \otimes \underbrace{\mathbf{M}^\iota}_{\rho_0^\iota \mathbf{F}^{-1} \mathbf{V}^\iota} \right) \mathbf{F}^\text{T} \right) dV.$$

Recalling the relation of the permutation symbol to the cross product, and the indicated relation between \mathbf{M}^ι and \mathbf{V}^ι leads to

$$\mathbf{0} = - \int_{\Omega_0} \boldsymbol{\epsilon} : ((\mathbf{P}^\iota - \mathbf{V}^\iota \otimes \rho_0^\iota \mathbf{F}^{-1} \mathbf{V}^\iota) \mathbf{F}^T) dV.$$

Localising this result and again applying the properties of the permutation symbol leads to the symmetry condition,

$$(2.12) \quad (\mathbf{P}^\iota - \mathbf{V}^\iota \otimes \rho_0^\iota \mathbf{F}^{-1} \mathbf{V}^\iota) \mathbf{F}^T = \mathbf{F} (\mathbf{P}^\iota - \mathbf{V}^\iota \otimes \rho_0^\iota \mathbf{F}^{-1} \mathbf{V}^\iota)^T.$$

But, $(\mathbf{V}^\iota \otimes \mathbf{F}^{-1} \mathbf{V}^\iota) \mathbf{F}^T = \mathbf{V}^\iota \otimes \mathbf{V}^\iota$, and thus, the symmetry $\mathbf{P}^\iota \mathbf{F}^T = \mathbf{F} (\mathbf{P}^\iota)^T$ that results from conservation of angular momentum for a purely mechanical theory is retained in this case of a mixture. The partial Cauchy stresses are therefore symmetric: $\boldsymbol{\sigma}^\iota = \boldsymbol{\sigma}^{\iota T}$, and this is also seen directly in terms of spatial quantities in Section 4.1.3.

Disparate results on the symmetry of stress stem primarily from the exact definitions of the fundamental quantities involved in the analysis. This is especially true of how the total stress in the system is distributed as partial stresses borne by the species comprising the system. For e.g., [Epstein and Maugin \(2000\)](#) incorporate an “irreversible” contribution from their species flux into their local measure of partial Cauchy stress. This results in their deduction of a non-symmetric partial Cauchy stress, in contrast to the result shown above.

2.1.4 Balance of energy

Since the masses of the various species constituting the system are allowed to change as a result of mass transport and interconversion, it is appropriate to work

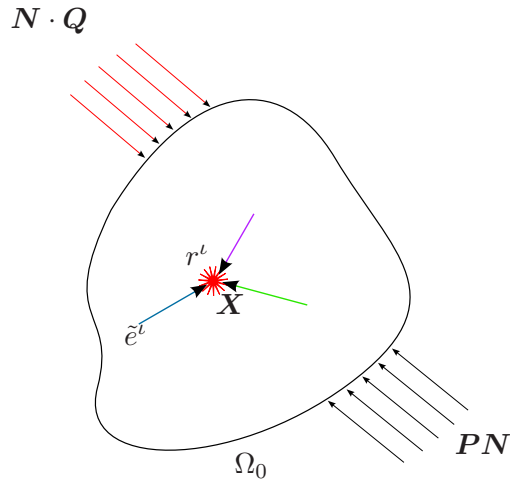


Figure 2.3: Energetic interactions the tissue is subject to.

with energy and energy-like quantities per unit mass. In addition to the terms introduced previously, the internal energy per unit mass of species ι is denoted e^ι , the heat supply to species ι per unit mass of that species is r^ι , and the partial heat flux vector of ι is Q^ι , defined on Ω_0 . An interaction energy, \tilde{e}^ι , appears between species and accounts for the energy transferred to ι by all other species, per unit mass of ι . These quantities are shown in Figure 2.3.

Working in Ω_0 , the rate of change of internal and kinetic energies of species ι is related to the work done on it by mechanical loads, processes of mass production and transport, heating and energy transfer as:

$$\begin{aligned}
& \underbrace{\frac{d}{dt} \int_{\Omega_0} \rho_0^\iota \left(e^\iota + \frac{1}{2} \|\mathbf{V} + \mathbf{V}^\iota\|^2 \right) dV}_{\text{Rate of change of energy}} = \underbrace{\int_{\Omega_0} (\rho_0^\iota \mathbf{g} \cdot (\mathbf{V} + \mathbf{V}^\iota) + \rho_0^\iota r^\iota) dV}_{\text{Work done by body forces and heat supplied}} \\
& \quad + \underbrace{\int_{\Omega_0} \rho_0^\iota \mathbf{q}^\iota \cdot (\mathbf{V} + \mathbf{V}^\iota) dV}_{\text{Work done by interaction forces}} \\
& \quad + \underbrace{\int_{\Omega_0} \left(\Pi^\iota \left(e^\iota + \frac{1}{2} \|\mathbf{V} + \mathbf{V}^\iota\|^2 \right) + \rho_0^\iota \tilde{e}^\iota \right) dV}_{\text{Energy from species creation and interaction}} \\
(2.13) \quad & + \underbrace{\int_{\partial\Omega_0} \left((\mathbf{V} + \mathbf{V}^\iota) \cdot \mathbf{P}^\iota - \mathbf{M}^\iota \left(e^\iota + \frac{1}{2} \|\mathbf{V} + \mathbf{V}^\iota\|^2 \right) - \mathbf{Q}^\iota \right) \cdot \mathbf{N} dA}_{\text{Work done by applied traction and energy leaving the domain as mass and heat flux}}.
\end{aligned}$$

The above equation for the rate of change of energy of a single species can be further simplified by applying the product rule and Gauss' Divergence Theorem (Appendix A.1), giving first,

$$\begin{aligned}
& \int_{\Omega_0} \left(\frac{\partial \rho_0^\iota}{\partial t} \left(e^\iota + \frac{1}{2} \|\mathbf{V} + \mathbf{V}^\iota\|^2 \right) + \rho_0^\iota \frac{\partial}{\partial t} \left(e^\iota + \frac{1}{2} \|\mathbf{V} + \mathbf{V}^\iota\|^2 \right) \right) dV = \\
& \quad \int_{\Omega_0} \left(\rho_0^\iota \mathbf{g} \cdot (\mathbf{V} + \mathbf{V}^\iota) + \rho_0^\iota r^\iota + \Pi^\iota \left(e^\iota + \frac{1}{2} \|\mathbf{V} + \mathbf{V}^\iota\|^2 \right) + \rho_0^\iota \tilde{e}^\iota \right) dV \\
& \quad + \int_{\Omega_0} \rho_0^\iota \mathbf{q}^\iota \cdot (\mathbf{V} + \mathbf{V}^\iota) dV \\
& \quad + \int_{\Omega_0} \left((\mathbf{V} + \mathbf{V}^\iota) \cdot \text{DIV} [\mathbf{P}^\iota] + \mathbf{P}^\iota : \text{GRAD} [\mathbf{V} + \mathbf{V}^\iota] \right) dV \\
& \quad - \int_{\Omega_0} \left(\text{DIV} [\mathbf{M}^\iota] \left(e^\iota + \frac{1}{2} \|\mathbf{V} + \mathbf{V}^\iota\|^2 \right) \right) dV \\
& \quad - \int_{\Omega_0} \left((\text{GRAD} [e^\iota] + (\mathbf{V} + \mathbf{V}^\iota) \cdot \text{GRAD} [\mathbf{V} + \mathbf{V}^\iota]) \cdot (\mathbf{M}^\iota) - \text{DIV} [\mathbf{Q}^\iota] \right) dV.
\end{aligned}$$

Applying the balance of mass (2.2) and the balance of momentum (2.7) to the equation above and localising the result, we have,

$$\begin{aligned}
\rho_0^\iota \frac{\partial e^\iota}{\partial t} &= \mathbf{P}^\iota : \text{GRAD} [\mathbf{V} + \mathbf{V}^\iota] - \text{DIV} [\mathbf{Q}^\iota] + \rho_0^\iota r^\iota + \rho_0^\iota \tilde{e}^\iota \\
(2.14) \qquad \qquad \qquad &\quad - \text{GRAD} [e^\iota] \cdot \mathbf{M}^\iota, \quad \forall \iota.
\end{aligned}$$

a final form of the balance of energy of a species ι which is most convenient for combining with the entropy inequality, leading to the Clausius-Duhem form of the dissipation inequality (Section 2.3).

Analogous to the results obtained in Sections 2.1.1 and 2.1.2, the inter-species energy transfers, \tilde{e}^ι , are related to interaction forces, \mathbf{q}^ι , and mass sources, Π^ι . To arrive at this relation, we first obtain the balance of mass of the entire system by summing Equation (2.13) over all species:

$$\begin{aligned}
\sum_\iota \frac{d}{dt} \int_{\Omega_0} \rho_0^\iota \left(e^\iota + \frac{1}{2} \|\mathbf{V} + \mathbf{V}^\iota\|^2 \right) dV &= \sum_\iota \int_{\Omega_0} (\rho_0^\iota \mathbf{g} \cdot (\mathbf{V} + \mathbf{V}^\iota) + \rho_0^\iota r^\iota) dV \\
&\quad + \sum_\iota \int_{\Omega_0} \rho_0^\iota \mathbf{q}^\iota \cdot (\mathbf{V} + \mathbf{V}^\iota) dV \\
(2.15) \qquad \qquad \qquad &\quad + \sum_\iota \int_{\Omega_0} \left(\Pi^\iota \left(e^\iota + \frac{1}{2} \|\mathbf{V} + \mathbf{V}^\iota\|^2 \right) + \rho_0^\iota \tilde{e}^\iota \right) dV \\
&\quad + \sum_\iota \int_{\partial\Omega_0} \left((\mathbf{V} + \mathbf{V}^\iota) \cdot \mathbf{P}^\iota - \mathbf{M}^\iota \left(e^\iota + \frac{1}{2} \|\mathbf{V} + \mathbf{V}^\iota\|^2 \right) - \mathbf{Q}^\iota \right) \cdot \mathbf{N} dA.
\end{aligned}$$

Then, expressing the rate of change of energy of the system interacting with its environment from the point of view of an external observer unaware of internal interactions between species (interaction forces, mass interconversion and inter-species energy transfers), we have,

$$\begin{aligned} \sum_{\iota} \frac{d}{dt} \int_{\Omega_0} \rho_0^{\iota} \left(e^{\iota} + \frac{1}{2} \|\mathbf{V} + \mathbf{V}^{\iota}\|^2 \right) dV &= \sum_{\iota} \int_{\Omega_0} (\rho_0^{\iota} \mathbf{g} \cdot (\mathbf{V} + \mathbf{V}^{\iota}) + \rho_0^{\iota} r^{\iota}) dV \\ &+ \sum_{\iota} \int_{\partial\Omega_0} \left((\mathbf{V} + \mathbf{V}^{\iota}) \cdot \mathbf{P}^{\iota} - \mathbf{M}^{\iota} \left(e^{\iota} + \frac{1}{2} \|\mathbf{V} + \mathbf{V}^{\iota}\|^2 \right) - \mathbf{Q}^{\iota} \right) \cdot \mathbf{N} dA. \end{aligned}$$

Since the equation above and (2.15) are equivalent statements of the balance of energy, it follows upon inspection and localisation that,

$$(2.16) \quad \sum_{\iota} \left(\rho_0^{\iota} \mathbf{q}^{\iota} \cdot (\mathbf{V} + \mathbf{V}^{\iota}) + \Pi^{\iota} \left(e^{\iota} + \frac{1}{2} \|\mathbf{V} + \mathbf{V}^{\iota}\|^2 \right) + \rho_0^{\iota} \tilde{e}^{\iota} \right) = 0.$$

This result, relating the interaction energies to interaction forces between species, their sources and relative velocities, is identical to that obtained from classical mixture theory (Truesdell and Noll, 1965), ensuring consistency of the present formulation with mixture theory.

2.2 The kinematics of growth

Local volumetric changes are associated with changes in the concentrations of solid collagen and fluid, $\iota = c, f$, and one important aspect of the coupling between mass transport and mechanics stems from this phenomenon.³ If the material of the solid collagen or fluid remains stress free, it swells with an increase in concentration (mass of the species per unit system volume), and shrinks as its concentration decreases. This leads to the notion of the *growth component* of the deformation gradient. This observation has led to an active field of study within the literature on biological growth (Skalak, 1981; Skalak et al., 1996; Klisch et al., 2001; Taber and

³Another important facet of this coupling arises from the thermodynamically-motivated constitutive relationship for species fluxes, as detailed in Section 2.3.4

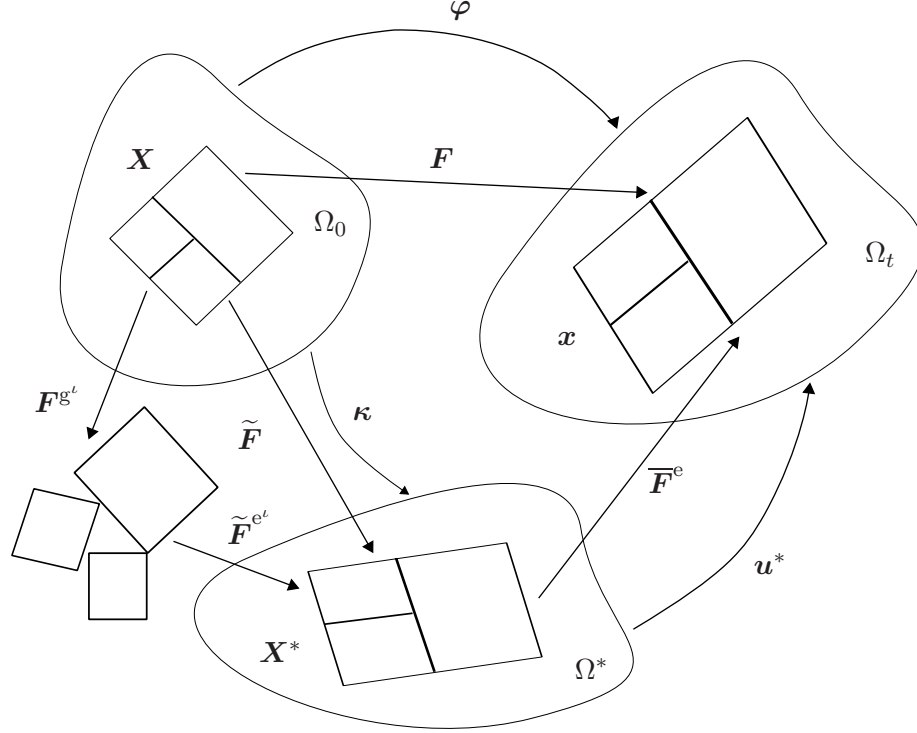


Figure 2.4: The kinematics of growth.

Humphrey, 2001; Lubarda and Hoger, 2002; Ambrosi and Mollica, 2002), and the treatment below follows in the same vein.

In the setting of finite strain kinematics, the total deformation gradient, \mathbf{F} , is decomposed into the growth component of the solid collagen, \mathbf{F}^{g^c} , a *geometrically-necessitated elastic component* accompanying growth, $\tilde{\mathbf{F}}^{\text{e}^c}$ and an *additional elastic component due to external stress*, $\bar{\mathbf{F}}^{\text{e}^c}$. Later, we will write $\mathbf{F}^{\text{e}^c} = \bar{\mathbf{F}}^{\text{e}^c} \tilde{\mathbf{F}}^{\text{e}^c}$. This elastic-growth decomposition is visualised in Figure 2.4 and is elaborated upon below.

This split of the total deformation gradient is analogous to the classical decomposition of multiplicative plasticity (Bilby and Smith, 1956; Lee, 1969). As explained in Section 2.4.1, we assume that the fluid-filled pores also deform with \mathbf{F} , and that a component, \mathbf{F}^{e^f} , of this total deformation gradient tensor, determines the fluid stress. We also assume a fluid growth component, \mathbf{F}^{g^f} , which is detailed below, and that $\mathbf{F}^{\text{e}^f} \mathbf{F}^{\text{g}^f} = \mathbf{F}$. As with the solid collagen we admit $\mathbf{F}^{\text{e}^f} = \bar{\mathbf{F}}^{\text{e}^f} \tilde{\mathbf{F}}^{\text{e}^f}$, the sub-

components carrying the same interpretation as for the solid collagen. However, this last decomposition is not explicitly used.

Assuming that the volume changes associated with growth described above are isotropic, a simple form for the growth part of the deformation gradient tensor is

$$(2.17) \quad \mathbf{F}^{\text{g}^\iota} = \left(\frac{\rho_0^\iota}{\rho_{0,\text{ini}}^\iota} \right)^{\frac{1}{3}} \mathbf{1}, \quad \iota = \text{c, f}$$

where $\rho_{0,\text{ini}}^\iota(\mathbf{X})$ is the reference concentration at the initial time, and $\mathbf{1}$ is the second-order isotropic tensor.⁴ In the state $\mathbf{F} = \mathbf{F}^{\text{g}^\iota}$, the species would be stress free. The kinematics being local, the action of $\mathbf{F}^{\text{g}^\iota}$ alone can result in incompatibility, which is eliminated by the geometrically-necessary elastic deformation $\tilde{\mathbf{F}}^{\text{e}^\iota}$, which causes an internal, self-equilibrated stress. The component $\bar{\mathbf{F}}^{\text{e}^\iota}$ is associated with a separate elastic deformation due to an external stress.

2.2.1 Saturation and tissue swelling

The degree of saturation of the solid phase plays a fundamental role in determining whether the tissue responds to an infusion (expulsion) of fluid by swelling (shrinking). In particular, the isotropic swelling law defined by Equation (2.17) has to be generalised to treat the case in which the solid phase is not saturated by fluid.

Figure 2.5 schematically depicts two possible scenarios. If the tissue is unsaturated in its current configuration, as in A, then, on a microscopic scale, it contains unfilled voids. It is thus capable of allowing an influx of fluid, which tends to increase its degree of saturation until fully saturated, as in B. This increase does not cause swelling of the tissue in the local stress-free state, as there is free volume for incoming

⁴This choice is only the simplest possible. Given the highly directional micro-structure and mechanical properties of many tissues, it seems likely that anisotropic growth is actually more common, as suggested by the thermodynamic arguments presented in Section 4.2.5.

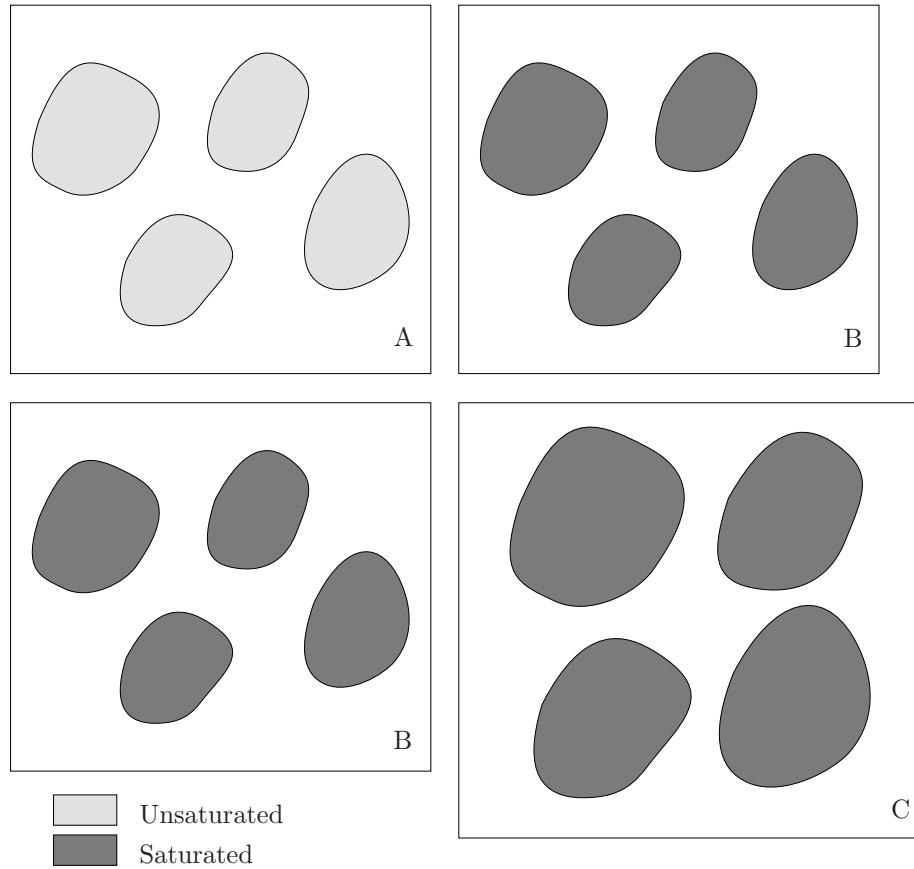


Figure 2.5: Stages of tissue saturation.

Unsaturated tissue in the current configuration (A) allows influx of fluid without swelling until it is completely saturated (B). Initially saturated tissue (B), in general, swells with influx of fluid (C).

fluid to occupy. However, once the tissue is saturated in the current configuration, an increase in the fluid content causes swelling in the stress-free state, as depicted in C, since there is no free volume for the entering fluid to occupy. It is this second case that is modelled by (2.17).

It is worth emphasising that this argument holds for $\mathbf{F}^{\text{g}^{\text{f}}}$, which is the local stress-free state of deformation of the fluid-containing pores at a point. The actual deformation gradient, $\mathbf{F} = \mathbf{F}^{\text{e}^{\text{f}}} \mathbf{F}^{\text{g}^{\text{f}}}$, also depends on the elastic part, $\mathbf{F}^{\text{e}^{\text{f}}}$, which is determined by the constitutive response of the fluid. Under stress, an incompressible fluid will have $\det(\mathbf{F}^{\text{e}^{\text{f}}}) = 1$, where $\det(\bullet)$ denotes the determinant of

a second-order tensor. Therefore, a fluid-saturated tissue will swell with fluid influx, $\det(\mathbf{F}) = \det(\mathbf{F}^{\text{gf}}) > 1$. A compressible fluid may have $\det(\mathbf{F}^{\text{ef}}) < 1$ allowing $\det(\mathbf{F}) < 1$ even with $\det(\mathbf{F}^{\text{gf}}) > 1$. But, even in this case, in the stress-free state there will be swelling.

Thus, for the fluid phase, the isotropic swelling law can be extended to the unsaturated case by introducing a degree of saturation, \tilde{v}^ι , defined in the current configuration, Ω_t , because it is in this configuration that it is physically relevant to discuss system saturation. We have $\tilde{v}^\iota = \rho^\iota / \tilde{\rho}^\iota$, where $\tilde{\rho}^\iota$ is the intrinsic density in Ω_t and is given by $\tilde{\rho}^\iota = \tilde{\rho}_0^\iota / \det(\mathbf{F})$. Note that the intrinsic reference density, $\tilde{\rho}_0^\iota$, is a material property. Upon solution of the mass balance equation (2.40) for ρ^ι , the species volume fractions, \tilde{v}^ι , can be computed in a straightforward fashion. The sum of these volume fractions is our required measure of saturation defined in Ω_t . We also recognise that for the dilute solutions obtained with physiologically-relevant solute concentrations, the saturation condition is very well approximated by $\tilde{v}^{\text{f}} + \tilde{v}^{\text{c}} = 1$. So, we proceed to redefine the fluid growth-induced component of the pore deformation gradient tensor as follows:

$$(2.18) \quad \mathbf{F}^{\text{gf}} = \begin{cases} \left(\frac{\rho_0^{\text{f}}}{\rho_{0\text{sat}}^{\text{f}}} \right)^{\frac{1}{3}} \mathbf{1}, & \tilde{v}^{\text{f}} + \tilde{v}^{\text{c}} = 1 \\ \mathbf{1}, & \text{otherwise.} \end{cases}$$

In Equation (2.18), $\rho_{0\text{sat}}^{\text{f}}$ is the reference concentration value at which the tissue attains saturation in the current configuration.

With this redefinition of \mathbf{F}^{gf} , it is implicit that $\tilde{v}^{\text{f}} + \tilde{v}^{\text{c}} > 1$ is non-physical. Saturation holds in the sense that $\tilde{v}^{\text{f}} + \tilde{v}^{\text{c}} = 1$. It has been common in soft tissue literature to assume that, under normal physiological conditions, soft tissues are fully saturated by the fluid and Equation (2.17) is appropriate for $\iota = \text{f}$. However,

this treatment of saturation and swelling induced by the fluid phase is necessary background for Section 2.3.3, where we examine the response of the fluid phase under tension. This approach also holds relevance for partial drying, which *ex vivo* or *in vitro* tissue may be subject to under certain laboratory conditions. It also significantly expands the relevance of the formulation by making it applicable to the mechanics of drained porous media other than biological tissue; most prominently, soils.

2.3 The entropy inequality and its restrictions on constitutive relations

The treatment presented in this section builds upon certain fundamental assumptions underlying the system under consideration. Firstly, the Second Law of thermodynamics (or the entropy production inequality) is assumed to hold at a continuum point for all species as a whole, but, in general, not for each individual species. Differing views on the spatial scale at which a continuum point is defined lead to varying interpretations of the Second Law. The spatial scale of our continuum point is chosen such that the following arguments are valid. Another assumption that is tied to this spatial scale, and consequently to the degree of observed homogeneity between mixed species, is that all species occupying a continuum point in the tissue have the same absolute temperature, θ .

With these assumptions, and denoting by η^ι the entropy per unit mass of species ι , the entropy inequality, when written out for the entire system in the reference configuration from the viewpoint of an external observer, reads:

$$\begin{aligned}
\underbrace{\sum_{\iota} \frac{d}{dt} \int_{\Omega_0} \rho_0^{\iota} \eta^{\iota} dV}_{\text{Rate of change of entropy}} &\geq \underbrace{\sum_{\iota} \int_{\Omega_0} \frac{\rho_0^{\iota} r^{\iota}}{\theta} dV}_{\text{Entropy added through heat supply}} \\
(2.19) \quad &- \underbrace{\sum_{\iota} \int_{\partial\Omega_0} \left(\mathbf{M}^{\iota} \cdot \mathbf{N} \eta^{\iota} + \frac{\mathbf{Q}^{\iota}}{\theta} \cdot \mathbf{N} \right) dA}_{\text{Entropy lost through mass and heat flux}}.
\end{aligned}$$

Applying Gauss' Divergence Theorem (Appendix A.1), using the mass balance equation (2.2), and localising the result, we have the following form of the entropy inequality,

$$\begin{aligned}
\sum_{\iota} \left(\rho_0^{\iota} \frac{\partial \eta^{\iota}}{\partial t} + \Pi^{\iota} \eta^{\iota} \right) &\geq \sum_{\iota} \left(\frac{\rho_0^{\iota} r^{\iota}}{\theta} - \text{GRAD} [\eta^{\iota}] \cdot \mathbf{M}^{\iota} \right) \\
(2.20) \quad &- \sum_{\iota} \left(\frac{\text{DIV} [\mathbf{Q}^{\iota}]}{\theta} - \frac{\text{GRAD} [\theta] \cdot \mathbf{Q}^{\iota}}{\theta^2} \right).
\end{aligned}$$

Now, multiplying Equation (2.20) by the temperature field, θ , subtracting it from the balance of energy (2.14) and using the balance of momentum (2.7) for $\rho_0^{\iota} \mathbf{q}^{\iota}$ gives,

$$\begin{aligned}
&\sum_{\iota} \rho_0^{\iota} \left(\frac{\partial e^{\iota}}{\partial t} - \theta \frac{\partial \eta^{\iota}}{\partial t} \right) + \sum_{\iota} \left(\Pi^{\iota} \left(\psi^{\iota} + \frac{1}{2} \|\mathbf{V} + \mathbf{V}^{\iota}\|^2 \right) + \frac{\text{GRAD} [\theta] \cdot \mathbf{Q}^{\iota}}{\theta} \right) \\
&+ \sum_{\iota} \left(\rho_0^{\iota} \frac{\partial}{\partial t} (\mathbf{V} + \mathbf{V}^{\iota}) - \rho_0^{\iota} \mathbf{g} - \text{DIV} [\mathbf{P}^{\iota}] + \text{GRAD} [\mathbf{V} + \mathbf{V}^{\iota}] \mathbf{M}^{\iota} \right) \cdot (\mathbf{V} + \mathbf{V}^{\iota}) \\
(2.21) \quad &- \sum_{\iota} \left(\mathbf{P}^{\iota} : \dot{\mathbf{F}} - \mathbf{P}^{\iota} : \text{GRAD} [\mathbf{V}^{\iota}] + (\text{GRAD} [e^{\iota}] - \theta \text{GRAD} [\eta^{\iota}]) \cdot \mathbf{M}^{\iota} \right) \leq 0,
\end{aligned}$$

the Clausius-Duhem (or reduced dissipation) inequality for the growth process. Here, $\psi^{\iota} = e^{\iota} - \theta \eta^{\iota}$ is the mass-specific Helmholtz free energy of species ι .

2.3.1 Thermodynamically-consistent constitutive framework

As is customary in field theories of continuum physics, the Clausius-Duhem inequality (2.21) derived above is used to obtain restrictions on constitutive relation-

ships governing the behaviour of the system.

We assume the following functional form of the internal energy per unit mass of species ι :⁵ $e^\iota = \hat{e}^\iota(\mathbf{F}^{\text{e}\iota}, \eta^\iota, \rho_0^\iota)$ and substitute this into the Clausius-Duhem inequality. Upon applying the chain rule of differentiation and regrouping some terms, (2.21) becomes,

$$\begin{aligned}
& \sum_{\iota} \left(\rho_0^\iota \frac{\partial e^\iota}{\partial \mathbf{F}^{\text{e}\iota}} - \mathbf{P}^\iota \mathbf{F}^{\text{g}\iota\text{T}} \right) : \dot{\mathbf{F}}^{\text{e}\iota} + \sum_{\iota} \rho_0^\iota \left(\frac{\partial e^\iota}{\partial \eta^\iota} - \theta \right) \frac{\partial \eta^\iota}{\partial t} \\
& + \sum_{\iota} \left(\rho_0^\iota \frac{\partial}{\partial t} (\mathbf{V} + \mathbf{V}^\iota) - \rho_0^\iota \mathbf{g} - \text{DIV} [\mathbf{P}^\iota] + \text{GRAD} [\mathbf{V} + \mathbf{V}^\iota] \mathbf{M}^\iota \right) \cdot (\mathbf{V}^\iota + \mathbf{V}) \\
& + \sum_{\iota} \left(\rho_0^\iota \mathbf{F}^{\text{r}\text{T}} (\text{GRAD} [e^\iota] - \theta \text{GRAD} [\eta^\iota]) \right) \cdot \mathbf{V}^\iota \\
& + \sum_{\iota} \Pi^\iota \left(\psi^\iota + \frac{1}{2} \|\mathbf{V} + \mathbf{V}^\iota\|^2 \right) + \sum_{\iota} \frac{\text{GRAD} [\theta] \cdot \mathbf{Q}^\iota}{\theta} \\
(2.22) \quad & + \sum_{\iota} \rho_0^\iota \frac{\partial e^\iota}{\partial \rho_0^\iota} \frac{\partial \rho_0^\iota}{\partial t} - \sum_{\iota} \mathbf{P}^\iota : (\text{GRAD} [\mathbf{V}^\iota] + \mathbf{F}^{\text{e}\iota} \dot{\mathbf{F}}^{\text{g}\iota}) \leq 0,
\end{aligned}$$

which represents a fundamental restriction upon the physical processes underlying biological growth. Any constitutive relationships that are prescribed must satisfy this restriction, as is well-known (Truesdell and Toupin, 1960). And so, making selections that ensure some terms on the left hand-side of (2.22) vanish (ensuring that they satisfy the relationship *a priori*), we prescribe the following constitutive relations which close the system of differential equations governing our tissue:

$$(2.23) \quad \mathbf{P}^\iota \mathbf{F}^{\text{g}\iota\text{T}} = \rho_0^\iota \frac{\partial e^\iota}{\partial \mathbf{F}^{\text{e}\iota}},$$

⁵This initial choice is one of the simplest possible (incorporating one field variable from each of the different kinds of physics considered: Mechanics, heat transfer and mass transport) and results in a restricted class of constitutive relationships. As seen in Section 4.2, mass-specific Helmholtz free energies of species dependent upon other variables, such as internal variables arising from mechanics, lead to a more general class of constitutive relationships, such as viscoelastic materials (Section 4.2.4).

which specifies that the constitutive relation for $\mathbf{P}^\iota \mathbf{F}^{g^{\iota T}}$ has the form of a hyperelastic material (Details regarding the specific hyperelastic model used for the computations in Chapter 3 have been discussed in the following section.),

$$(2.24) \quad \theta = \frac{\partial e^\iota}{\partial \eta^\iota},$$

which implies that the absolute temperature, following the definition normally employed in thermal physics, is uniform across all species,

$$(2.25) \quad \begin{aligned} \rho_0^\iota \mathbf{V}^\iota = & - \frac{\tilde{\mathbf{D}}^\iota}{\rho_0^\iota} (\rho_0^\iota \mathbf{g} - \text{DIV} [\mathbf{P}^\iota] + \text{GRAD} [\mathbf{V}] \mathbf{M}^\iota) \\ & - \frac{\tilde{\mathbf{D}}^\iota}{\rho_0^\iota} (\rho_0^\iota \mathbf{F}^{-T} (\text{GRAD} [e^\iota] - \theta \text{GRAD} [\eta^\iota])), \end{aligned}$$

which provides a constitutive relationship for the species fluxes⁶ in terms of a product of a positive semi-definite mobility tensor, $\tilde{\mathbf{D}}^\iota$, and a summation of different driving forces (which is discussed in greater detail at a later section (2.3.4)), and finally,

$$(2.26) \quad \mathbf{Q}^\iota = -\mathbf{K}^\iota \text{GRAD} [\theta],$$

which states that the heat flux in species ι is given by the product of a positive semi-definite conductivity tensor, \mathbf{K}^ι , and the negative of the temperature gradient field. This relationship is identical to the Fourier Law of heat conduction.

With these constitutive relations (2.23–2.26) ensuring that certain terms of the dissipation inequality vanish, (2.22) is further reduced to

⁶A careful comparison of this relation (2.25) with the motivating term in the Clausius-Duhem inequality (2.22) will reveal that a driving force from the acceleration of the solid phase does not appear in the constitutive relationship for the species flux. Appendix B.1 discusses this absence in greater detail.

$$\begin{aligned}
(2.27) \quad & \sum_i \left(\rho_0^i \frac{\partial e^i}{\partial \rho_0^i} \frac{\partial \rho_0^i}{\partial t} - \mathbf{P}^i : (\text{GRAD} [\mathbf{V}^i] + \mathbf{F}^{e^i} \dot{\mathbf{F}}^{g^i}) \right) \\
& + \sum_i \left(\rho_0^i \mathbf{V}^i \cdot \left(\frac{\partial}{\partial t} (\mathbf{V} + \mathbf{V}^i) + (\text{GRAD} [\mathbf{V}^i]) \mathbf{F}^{-1} \mathbf{V}^i \right) + \Pi^i \left(\psi^i + \frac{1}{2} \|\mathbf{V} + \mathbf{V}^i\|^2 \right) \right) \\
& + \sum_i \left(\rho_0^i \frac{\partial}{\partial t} (\mathbf{V} + \mathbf{V}^i) - \rho_0^i \mathbf{g} - \text{DIV} [\mathbf{P}^i] + \text{GRAD} [\mathbf{V} + \mathbf{V}^i] \mathbf{M}^i \right) \cdot \mathbf{V} \leq 0.
\end{aligned}$$

The left hand-side of (2.27) is the dissipation, \mathcal{D} , a quantity whose non-positiveness has to be numerically verified when performing computations to ensure that additional constitutive choices (such as those for the source terms, Π^i , are thermodynamically valid).

When the dissipation inequality is revisited while deriving the growth formulation from an Eulerian perspective in a later chapter (Section 4.2), additional constitutive relations will be introduced which ensure that all terms in the dissipation, \mathcal{D} , are satisfied a priori. But now, we will take a detailed look at the specific forms of the constitutive relations used in the computations presented in Chapter 3. In particular, Section 2.3.2 discusses the strain energy density function for collagen derived from an anisotropic network model based on entropic elasticity, Section 2.3.3 describes the pressure response of an ideal, nearly-incompressible fluid, Section 2.3.4 details the constitutive relationship for the fluid flux, Section 2.3.6, in a similar manner, discusses solute transport, and finally, Section 2.3.7 provides some examples and physiological motivation for different kinds of collagen sources.

2.3.2 An anisotropic network model

From Equation (2.23), the partial first Piola-Kirchhoff stress of collagen, modelled as a hyperelastic material, is $\mathbf{P}^c = \rho_0^c \frac{\partial e^c}{\partial \mathbf{F}^{e^c}} \mathbf{F}^{g^c}{}^{-\text{T}}$. Recall from Section 2.2 that

$\mathbf{F}^{\text{e}^c} = \mathbf{F}\mathbf{F}^{\text{g}^c}{}^{-1}$ is the elastic part, and \mathbf{F}^{g^c} is the growth part, respectively, of the deformation gradient of collagen. Along the lines of Equation (2.17), if we were considering unidirectional growth of collagen along a unit vector \mathbf{e} , we would have $\mathbf{F}^{\text{g}^c} = \frac{\rho_0^c}{\rho_{0\text{ini}}^c} \mathbf{e} \otimes \mathbf{e}$, with $\rho_{0\text{ini}}^c$ denoting the initial concentration of collagen at the point.

The mechanical response of tendons in tension is determined primarily by their dominant structural component: highly oriented fibrils of collagen. In this formulation, the strain energy density for collagen has been obtained from hierarchical multi-scale considerations based upon an entropic elasticity-based worm-like chain (WLC) model (Kratky and Porod, 1949). The WLC model has been widely used for long chain single molecules, most prominently for DNA (Marko and Siggia, 1995; Rief et al., 1997; Bustamante et al., 2003), and for the collagen monomer (Sun et al., 2002). The central parameters of this model are the chain's contour length, L , and persistence length, A . The latter is a measure of its stiffness and given by $A = \chi/k\theta$, where χ is the bending rigidity, k is Boltzmann's constant and θ is the temperature. See Landau and Lifshitz (1951) for a general formulation of statistical mechanics models of long chain molecules. Fitting the WLC response function derived by Marko and Siggia (1995) to the collagen *fibril* data of Graham et al. (2004) results in values of $A = 6$ nm and $L = 3480$ nm. This is to be compared with $A = 14.5$ nm and $L = 309$ nm, reported by Sun et al. (2002), for a *single* collagen molecule. Taken together, these results demonstrate that the WLC analysis correctly predicts a collagen fibril to be longer and more compliant than its constituent molecule due to compliant intermolecular cross-links in fibrils.

To model a collagen network structure, the WLC model has been embedded as a single constituent chain of an eight-chain model (Bischoff et al., 2002a,b), depicted in Figure 2.6. Homogenisation via averaging then leads to the following functional

form for the internal energy density, \hat{e}^c :⁷

(2.28)

$$\begin{aligned} \rho_0^c \hat{e}^c(\mathbf{F}^{ec}, \rho_0^c) &= \frac{Nk\theta L}{4A} \left(\frac{2r^2}{L^2} + \frac{1}{1-r/L} - \frac{r}{L} \right) \\ &\quad + \frac{\gamma}{\beta} (J^{ec^{-2\beta}} - 1) + \gamma \mathbf{1} : (\mathbf{C}^{ec} - \mathbf{1}) \\ &\quad - \frac{Nk\theta}{4\sqrt{2L/A}} \left(\sqrt{\frac{2A}{L}} + \frac{1}{4(1-\sqrt{2A/L})} - \frac{1}{4} \right) \log \left(\lambda_1^{e^{a^2}} \lambda_2^{e^{b^2}} \lambda_3^{e^{c^2}} \right). \end{aligned}$$

Here, N is the density of chains, and a, b and c are lengths of the unit cell sides aligned with the principal stretch directions. The material model is isotropic only if $a = b = c$. The elastic stretches along the unit cell axes are denoted by λ_1^e, λ_2^e and λ_3^e , respectively, and $\mathbf{C}^{ec} = \mathbf{F}^{ec\text{T}} \mathbf{F}^{ec}$ is the elastic right Cauchy-Green tensor of collagen. The factors γ and β control the bulk compressibility of the model. The end to end chain length is given by $r = \frac{1}{2} \sqrt{a^2 \lambda_1^{e^2} + b^2 \lambda_2^{e^2} + c^2 \lambda_3^{e^2}}$, where $\lambda_I^e = \sqrt{\mathbf{N}_I \cdot \mathbf{C}^{ec} \mathbf{N}_I}$, and $\mathbf{N}_I, I = 1, 2, 3$ are the unit vectors along the three unit cell axes, respectively. Since the quantities L, A and r occur only as the ratios L/A and r/L in this model (2.28), Table 3.1 lists the lengths L, A, a, b, c used in the computations in a non-dimensionalised manner.

2.3.3 A nearly incompressible ideal fluid

In this work, the fluid phase is treated as nearly incompressible and ideal, i.e., inviscid. The partial Cauchy stress in the fluid is:

$$(2.29) \quad \boldsymbol{\sigma}^f = \det(\mathbf{F}^{ef})^{-1} \mathbf{P}^f \mathbf{F}^{ef\text{T}} = h(\rho^f) \mathbf{1},$$

where a large value of $h'(\rho^f)$ ensures near-incompressibility.

⁷Under the isothermal conditions assumed here, \hat{e}^c is independent of θ . Accordingly, we have the parametrisation $e^c = \hat{e}^c(\mathbf{F}^{ec}, \rho_0^c)$.

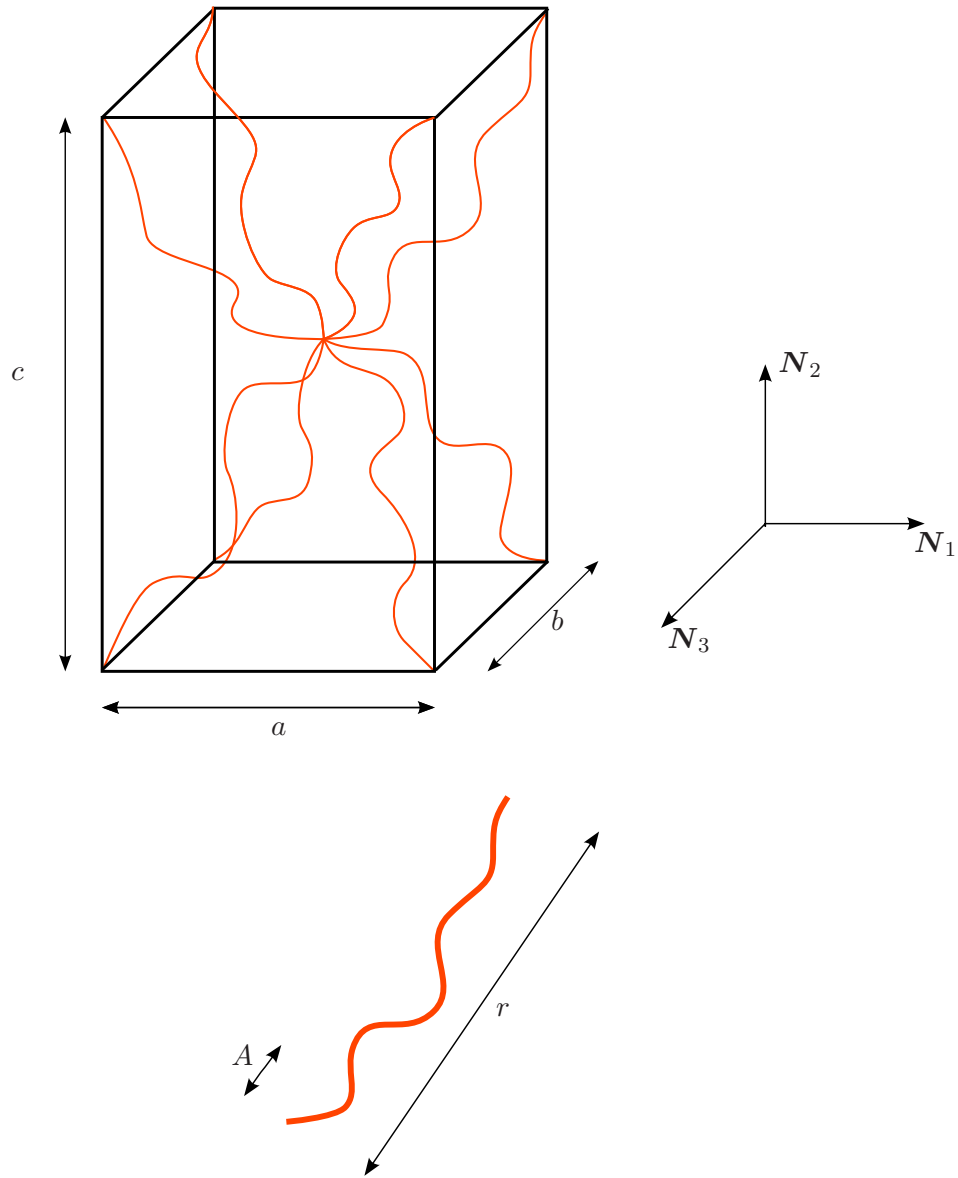


Figure 2.6: The eight-chain model incorporating worm-like chains.

Response of the fluid in tension; cavitation

The response of an ideal fluid, as defined by Equation (2.29), does not distinguish between tension and compression, i.e., whether $\det(\mathbf{F}^{\text{ef}}) \gtrless 1$. Being (nearly) incompressible, the fluid can develop compressive hydrostatic stress without bound—a case that is modelled accurately. However, the fluid can develop at most a small tensile hydrostatic stress (Brennen, 1995),⁸ and the tensile stiffness of the tissue is mainly from the collagen phase. This is not accurately represented by (2.29), which models a symmetric response in tension and compression.

Here, we preclude all tensile load carrying by the fluid by limiting $\det(\mathbf{F}^{\text{ef}}) \leq 1$ as follows. We first introduce an additional component to the relation between deformation of the pore space, given by \mathbf{F} , the fluid stress-determining tensor, \mathbf{F}^{ef} and the growth tensor for the fluid, \mathbf{F}^{gf} . Consider the cavitation (void forming) tensor, \mathbf{F}^{v} , defined by

$$(2.30) \quad \mathbf{F}^{\text{ef}} \mathbf{F}^{\text{gf}} \mathbf{F}^{\text{v}} = \mathbf{F}.$$

We restrict the formulation to include only saturated current configurations at the initial time. Following Section 2.2.1, we have $\tilde{v}^{\text{f}} + \tilde{v}^{\text{c}} = 1$ at $t = 0$, the saturation condition in Ω_t when solutes are at low concentrations. At later times, Equation (2.18) holds for \mathbf{F}^{gf} . If $\det(\mathbf{F}(\mathbf{F}^{\text{gf}})^{-1}) \leq 1$ we set $\mathbf{F}^{\text{ef}} = \mathbf{F}(\mathbf{F}^{\text{gf}})^{-1}$ and $\mathbf{F}^{\text{v}} = \mathbf{1}$ for no cavitation. Otherwise, since $\det(\mathbf{F}(\mathbf{F}^{\text{gf}})^{-1}) > 1$, we specify $\mathbf{F}^{\text{ef}} = \det(\mathbf{F}(\mathbf{F}^{\text{gf}})^{-1})^{-1/3} \mathbf{F}(\mathbf{F}^{\text{gf}})^{-1}$, thus restricting \mathbf{F}^{ef} to be unimodular and allow cavitation by writing $\mathbf{F}^{\text{v}} = \mathbf{F}(\mathbf{F}^{\text{ef}} \mathbf{F}^{\text{gf}})^{-1}$.

⁸Where, we are referring to the fluid being subject to net tension, not just a reduction in fluid compressive stress from reference ambient pressure.

These conditional relations are summarised as:

$$(2.31) \quad \mathbf{F}^{\text{ef}} = \begin{cases} \mathbf{F}(\mathbf{F}^{\text{gf}})^{-1}, \mathbf{F}^{\text{v}} = \mathbf{1} & \text{if } \det(\mathbf{F}(\mathbf{F}^{\text{gf}})^{-1}) \leq 1, \\ \det(\mathbf{F}(\mathbf{F}^{\text{gf}})^{-1})^{-1/3} \mathbf{F}(\mathbf{F}^{\text{gf}})^{-1}, & \\ \mathbf{F}^{\text{v}} = \mathbf{F}(\mathbf{F}^{\text{ef}} \mathbf{F}^{\text{gf}})^{-1} & \text{otherwise.} \end{cases}$$

2.3.4 Driving forces for fluid flux

Returning to the constitutive relation for species flux (2.25), we first recognise that $\mathbf{M}^\ell = \rho_0^\ell \mathbf{F}^{-1} \mathbf{V}^\ell$ is an implicit relation for \mathbf{V}^ℓ . Rewriting this instead as an explicit one for $\rho_0^\ell \mathbf{V}^\ell$ we have,

$$\rho_0^\ell \mathbf{V}^\ell = \left(\mathbf{1} + \frac{\tilde{\mathbf{D}}^\ell \text{GRAD}[\mathbf{V}] \mathbf{F}^{-1}}{\rho_0^\ell} \right)^{-1} \frac{\tilde{\mathbf{D}}^\ell}{\rho_0^\ell} \left(\rho_0^\ell \mathbf{g} + \text{DIV}[\mathbf{P}^\ell] - \rho_0^\ell \mathbf{F}^{-\text{T}} (\text{GRAD}[e^\ell] - \theta \text{GRAD}[\eta^\ell]) \right).$$

From this, the constitutive relationship for mass flux is written as a product of a mobility tensor and a thermodynamic driving force,

$$(2.32) \quad \mathbf{M}^\ell = \underbrace{\mathbf{F}^{-1} \left(\mathbf{1} + \frac{\tilde{\mathbf{D}}^\ell \text{GRAD}[\mathbf{V}] \mathbf{F}^{-1}}{\rho_0^\ell} \right)^{-1} \frac{\tilde{\mathbf{D}}^\ell}{\rho_0^\ell} \mathbf{F}^{-\text{T}}}_{\mathbf{D}^\ell} \underbrace{\left(\rho_0^\ell \mathbf{F}^{\text{T}} \mathbf{g} + \mathbf{F}^{\text{T}} \text{DIV}[\mathbf{P}^\ell] - \rho_0^\ell (\text{GRAD}[e^\ell] - \theta \text{GRAD}[\eta^\ell]) \right)}_{\mathcal{F}^\ell}.$$

In particular, the constitutive relation for the flux of extra-cellular fluid relative to collagen in the reference configuration takes the following form,

$$(2.33) \quad \mathbf{M}^{\text{f}} = \mathbf{D}^{\text{f}} \left(\rho_0^{\text{f}} \mathbf{F}^{\text{T}} \mathbf{g} + \mathbf{F}^{\text{T}} \text{DIV}[\mathbf{P}^{\text{f}}] - \rho_0^{\text{f}} \text{GRAD}[\psi^{\text{f}}] \right),$$

where \mathbf{D}^f is the positive semi-definite mobility of the fluid, and isothermal conditions are assumed in order to approximate the physiological ones.⁹

Experimentally determined transport coefficients (e.g. for mouse tail skin (Swartz et al., 1999) and rabbit Achilles tendons (Han et al., 2000)) are used for the fluid mobility values. Recall that the terms in the parenthesis on the right hand-side of Equation (2.33) sum to give the total driving force for transport. The first term is the contribution due to gravitational acceleration. In order to maintain physiological relevance, this term has been neglected in the following treatment. The second term arises from stress divergence. In the case of a non-uniform partial stress, \mathbf{P}^t , there exists a thermodynamic driving force for transport along \mathbf{P}^t . For an ideal fluid, it reduces to a pressure gradient, thereby specifying that the fluid moves down a compressive pressure gradient, which is Darcy's Law. The third term is the gradient of the Helmholtz free energy potential, $\psi^f = e^f - \theta\eta^f$, where e^f is the mass-specific internal energy, θ is temperature and η^f is the mass-specific entropy. The entropy gradient included in this term results in classical Fickian diffusion if only mixing entropy exists, as discussed in the following section.

In practice, since the driving forces in (2.33) originate from different physics, it proves useful (also seen in the following section) to rewrite (2.33) as

$$(2.34) \quad \mathbf{M}^f = \mathbf{D}_P^f \mathbf{F}^T \text{DIV} [\mathbf{P}^f] - \mathbf{D}_\psi^f \text{GRAD} [\psi^f],$$

where \mathbf{D}_P^f is now the permeability of the tissue, corresponding to stress gradient-driven transport, and \mathbf{D}_ψ^f is the mobility, corresponding to transport of the fluid phase through the porous solid driven by the gradient of the Helmholtz free energy.

⁹Additionally, this assumption allows application of the Legendre transformation $\psi^t = e^t - \theta\eta^t$ to rewrite $\text{GRAD} [e^t] - \theta \text{GRAD} [\eta^t]$ as $\text{GRAD} [\psi^t] |_\theta$ (at uniform temperature), where ψ^t is the Helmholtz free energy potential.

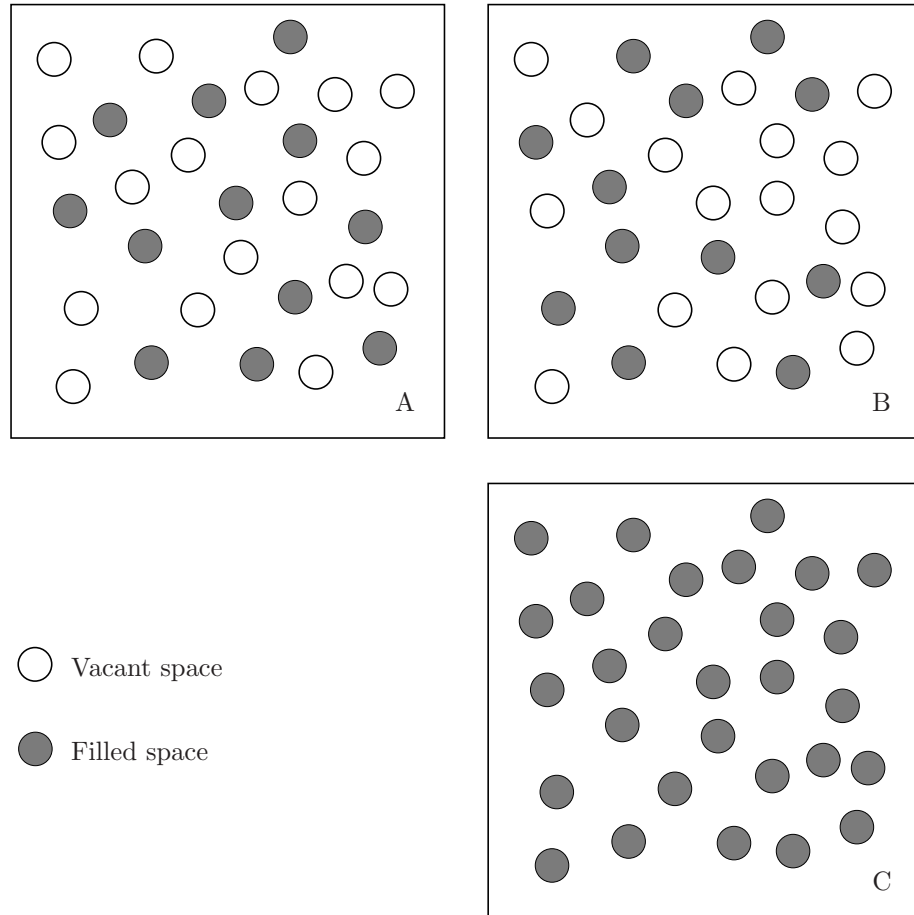


Figure 2.7: Saturation depicted at a microscopic scale.

Depicted at a microscopic scale, only unsaturated tissues A and B can undergo Fickian diffusion of the fluid. C is saturated.

2.3.5 Saturation and Fickian diffusion

As depicted in Figure 2.7, only when pores are unsaturated are there multiple configurations available to the fluid molecules at a fixed fluid concentration. This leads to a non-zero mixing entropy. In contrast, if saturated, there is only a single available configuration (degeneracy), resulting in zero mixing entropy. Consequently, Fickian diffusion, which arises from the gradient of mixing entropy can exist only in the unsaturated case. However, even a saturated pore structure can demonstrate concentration gradient-dependent mass transport phenomenologically: The fluid stress

depends on fluid concentration (see Equation (2.29)), and fluid stress gradient-driven flux appears as a concentration gradient-driven flux.

The saturation dependence of Fickian diffusion is modelled by using the measure of saturation introduced in Section 2.2.1. We rewrite the free energy potential as:

$$(2.35) \quad \begin{aligned} \psi^f &= e^f - \theta \eta^f, \text{ and} \\ \eta^f &\rightarrow 0, \text{ as } \tilde{v}^f + \tilde{v}^c \rightarrow 1. \end{aligned}$$

It is again important to note that under physiological conditions, soft tissues are fully saturated by fluid, and it is appropriate to set $\psi^f = e^f$.

2.3.6 Solute transport

The dissolved solute species, denoted by s , undergo long range transport primarily by being advected by the fluid. In addition to this, they undergo diffusive transport relative to the fluid. This motivates an additional velocity split of the form $\mathbf{V}^s = \widetilde{\mathbf{V}}^s + \mathbf{V}^f$, where $\widetilde{\mathbf{V}}^s$ denotes the velocity of the solute relative to the fluid. The constitutive relation for the corresponding flux, denoted by $\widetilde{\mathbf{M}}^s$, has the following form, similar to Equation (2.33) defined for the fluid flux.

$$(2.36) \quad \widetilde{\mathbf{M}}^s = \mathbf{D}^s (-\rho_0^s \text{GRAD} [\psi^s]),$$

where \mathbf{D}^s is the positive semi-definite mobility of the solute *relative to the fluid*, and again, isothermal conditions are assumed to approximate the physiological ones. Following Section 2.1.2, there are no stress-dependent contributions to $\widetilde{\mathbf{M}}^s$.

2.3.7 Nature of the sources

There exists a large body of literature, (Cowin and Hegedus, 1976; Epstein and Maugin, 2000; Ambrosi and Mollica, 2002), that addresses growth in biological tissue mainly based upon a single species undergoing transport and production/annihilation. However, from a biochemical point of view, growth in soft biological tissue is the production and resorption of the tissue's collagen phase as a result of a complex cascade of biochemical reactions taking place within the cells (Alberts et al., 2002). These processes involve several species, and additionally involve intimate coupling between mass transfer, biochemistry and mechanics.

An example of this chemo-mechanical coupling is seen in Figure 2.8 (from the experimental work of Calve et al. (2007)), where the implantation of tendon-like engineered collagenous constructs into live rats, and their conditioning in vivo (denoted by the blue curve) leads to significant increases in the collagen strength and stiffness (when compared to the in vitro control in green); highlighting the importance of the biochemical environment on the processes underlying growth.

The modelling approach followed in this work is to select appropriate functional forms of the source/sink terms, Π^t , that abstract the complexity of the biochemistry. Some specific examples follow.

(i) *First-order chemical kinetics* is one of the simplest possible choices for the collagen source, and assumes that the production of collagen is governed by a first-order rate law. Newly-produced collagen has proteoglycan molecules bound to it, and they in turn bind water. This effect is modelled by associating a loss of nutrient-bearing free fluid along with collagen production. A fluid sink Π^f is introduced following first order kinetics,

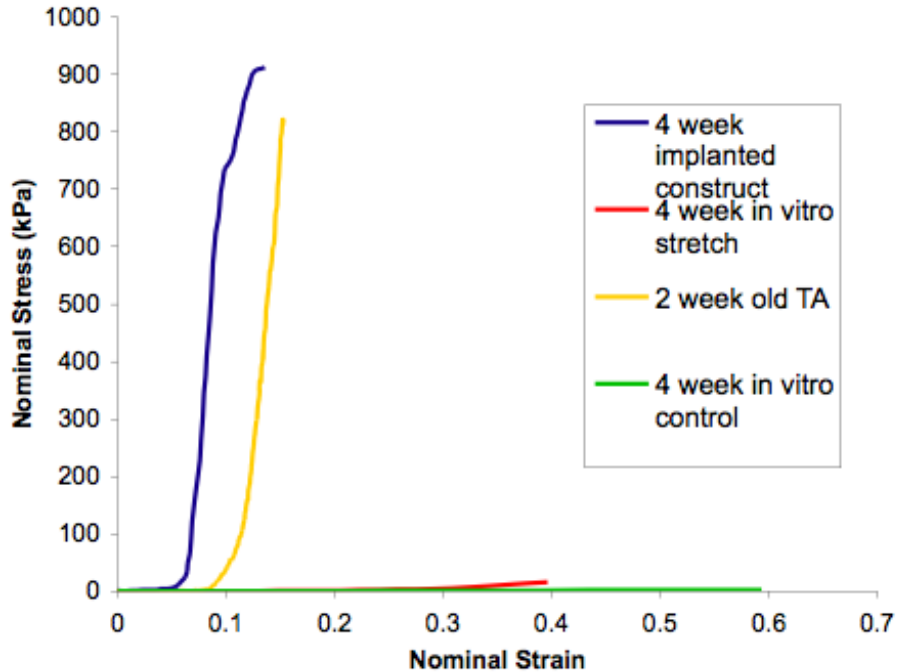


Figure 2.8: Growth and strengthening under biochemical influences.

$$(2.37) \quad \Pi^f = -k^f(\rho_0^f - \rho_{0\text{ini}}^f),$$

and the collagen source is mathematically equivalent to the fluid sink: $\Pi^c = -\Pi^f$. For this functional form, when $\rho_0^f > \rho_{0\text{ini}}^f$, a certain reference value of the fluid concentration, collagen is produced.

(ii) *Michaelis-Menten* enzyme kinetics (see, for e.g., [Sengers et al. \(2004\)](#)), which involves a two-step reaction, introduces collagen and solute source terms given by

$$(2.38) \quad \Pi^s = \frac{-(k_{\text{max}}\rho^s)}{(\rho_m^s + \rho^s)}\rho_{\text{cell}}, \quad \Pi^c = -\Pi^s,$$

where ρ_{cell} is the concentration of fibroblasts, k_{max} is the maximum value of the solute production reaction rate constant, and ρ_m^s is half the solute concentration

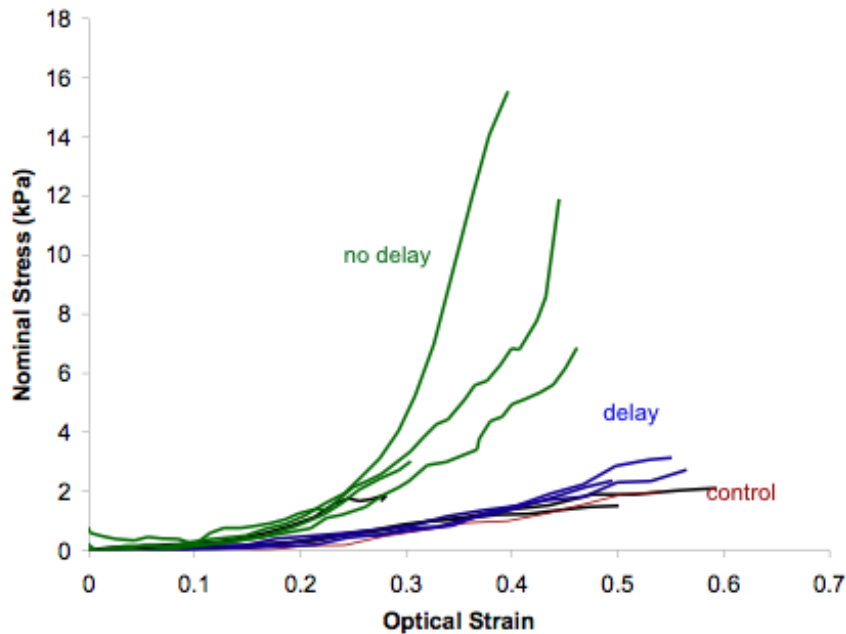


Figure 2.9: Growth and strengthening under mechanical influences.

corresponding to k_{\max} . For details on the chemistry modelled by the Michaelis-Menten model, see, for e.g., [Bromberg and Dill \(2002\)](#).

(iii) *Strain energy-dependent* sources induce growth at a point when the energy density deviates from a reference value. Figure 2.9 (also from the experimental work of [Calve et al. \(2007\)](#)) provides an example of the effect of mechanical influences on the strengths and stiffnesses of tendons by comparing the stress-strain responses of unloaded control specimens with those subjected to two different load cases (denoted *delay* and *no delay* in the figure).

An example of source terms of this form was originally proposed in the context of bone growth ([Harrigan and Hamilton, 1993](#)). I am not aware of studies that have developed similar functional forms for soft tissue, and therefore have adapted this example from the bone growth literature, recognising that this topic is in need of further study. Suitably weighted by a relative concentration ratio, and written for

collagen, this source term has the form

$$(2.39) \quad \Pi^c = \left(\frac{\rho_0^c}{\rho_{0\text{ini}}^c} \right)^{-m} e^c - e_*^c,$$

where m is a non-negative exponent, e^c is the mass-specific strain energy function of collagen, and e_*^c is a reference value of this strain energy density. Equation (2.39) models collagen production when the strain energy density (weighted by a concentration ratio) at a point exceeds this reference value, and models annihilation otherwise.

2.4 Algorithmic considerations

Concluding the analytic formulation for biological growth presented in this chapter, the following sections discuss some algorithmic details that are specific to our system of interest, and underly the numerical examples of Chapter 3.

2.4.1 The role of mass balance in the current configuration

Before proceeding, let us first consider the central kinematic assumption underlying the formulation: We assume that the pore structure deforms with the collagenous phase. Therefore, the deformation gradient, \mathbf{F} , is common to c and the fluid-filled pore spaces. Furthermore, in what follows, we will treat the fluid as ideal and nearly-incompressible, i.e. as elastic (Section 2.3.3). This combination of kinematic and constitutive assumptions to be elaborated upon, implies that the stress in the fluid phase is determined by the elastic part of \mathbf{F} (see Sections 2.2 and 2.3.3). For clarity we denote it as \mathbf{F}^{e^f} . Importantly, the pore-filling fluid under stress can also undergo transport relative to the pore network; i.e., relative to the collagenous phase. This is the fluid flux, denoted by \mathbf{M}^f in the reference configuration. At the outset, we preclude stress in any of the solute species, s . Only the solid collagen and fluid

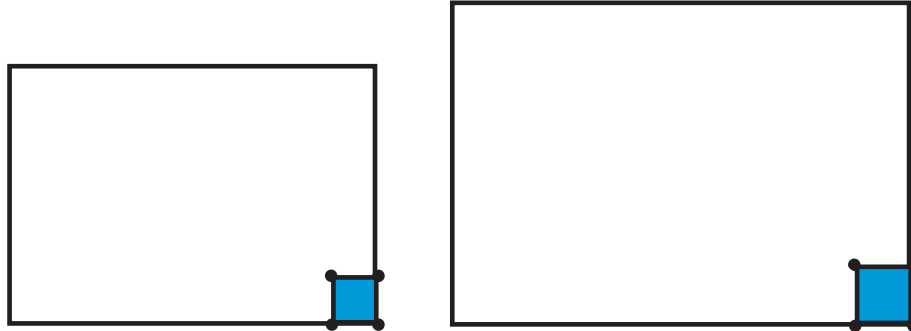


Figure 2.10: Pore structure at the boundary deforming with the tissue.

If the pore structure at the boundary deforms with the tissue and this boundary is in contact with a fluid bath, the fluid concentration with respect to the current configuration, i.e., ρ^f , remains constant.

bear stress.

Although the initial/boundary value problem of mass transport can be consistently posed in the reference configuration, the evolving current configuration, Ω_t , is of greater interest from a physical standpoint for growth problems. It follows from the discussion in the preceding paragraph that the shape and size of pores in Ω_t is determined by \mathbf{F} . Therefore, at the boundary, the fluid concentration with respect to Ω_t remains constant if the boundary is in contact with a fluid bath. Accordingly, this is the appropriate Dirichlet boundary condition to impose under normal physiological conditions. This is shown in an idealised manner in Figure 2.10.

In the interest of applying boundary conditions (either specification of species flux or concentration) that are physically meaningful, we use the local form of the balance of mass in the current configuration,

$$(2.40) \quad \frac{d\rho^l}{dt} = \pi^l - \operatorname{div}[\mathbf{m}^l] - \rho^l \operatorname{div}[\mathbf{v}], \quad \forall l,$$

obtained by pushing-forward the balance of mass in the reference configuration (2.2) to the current configuration, and is identical to the form derived from an Eulerian

perspective in Section 4.1.1. Here, $\rho^\iota(\mathbf{x}, t)$, $\pi^\iota(\mathbf{x}, t)$, and $\mathbf{m}^\iota(\mathbf{x}, t)$ are the current mass concentration, source and mass flux of species ι respectively and $\mathbf{v}(\mathbf{x}, t)$ is the velocity of the solid phase. They are related to corresponding reference quantities as $\rho^\iota = (\det(\mathbf{F}))^{-1} \rho_0^\iota$, $\pi^\iota = (\det(\mathbf{F}))^{-1} \Pi^\iota$ and $\mathbf{m}^\iota = (\det(\mathbf{F}))^{-1} \mathbf{F} \mathbf{M}^\iota$. $\text{div}[\bullet]$ denotes the spatial divergence operator, and the left hand-side in Equation (2.40) is the material time derivative relative to the solid, which may be written explicitly as $\frac{\partial}{\partial t}|_X$, implying that the reference position of the solid collagenous skeleton is held fixed.

2.4.2 Incompressible fluid in a porous solid

Upon incorporation of the additional velocity split, $\mathbf{v}^s = \tilde{\mathbf{v}}^s + \mathbf{v}^f$, described in Section 2.3.6, the resulting mass transport equation (2.40) in the current configuration for the solute species is:

$$(2.41) \quad \frac{d\rho^s}{dt} = \pi^s - \text{div} \left[\tilde{\mathbf{m}}^s + \frac{\rho^s}{\rho^f} \mathbf{m}^f \right] - \rho^s \text{div}[\mathbf{v}].$$

In the hyperbolic limit, where advection dominates, spatial oscillations emerge in numerical solutions of this equation (Brooks and Hughes, 1982; Hughes et al., 1987). Figure 2.11 demonstrates this oscillation for a simple advection-diffusion problem at a large *Péclet number*, which is a measure of the relative magnitude of advection to diffusion. However, Equation (2.41) is not in standard advection-diffusion form, and is thus not amenable to the application of standard stabilisation techniques (Hughes et al., 1987). In part, this is because although the (near) incompressibility of the fluid phase is embedded in the balance of linear momentum via the fluid stress, it has not yet been explicitly incorporated into the transport equations. This section proceeds to impose the fluid incompressibility condition and deduces implications for

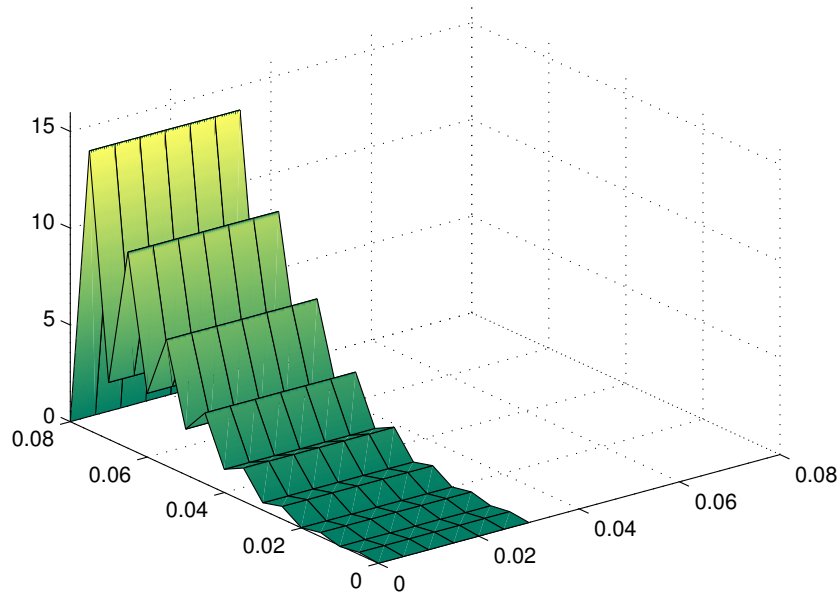


Figure 2.11: Spatial oscillations in the numerical solution ($Pe = 100$).

The standard Galerkin method for the advection-diffusion equation at large Péclet numbers is unstable.

the solute mass transport equation, including a crucial simplification allowing for its straightforward numerical stabilisation.

From Equation (2.40), the local form of the balance of mass for the fluid species (assuming that the fluid species does not take part in reactions, i.e. $\pi^f = 0$) in the current configuration is

$$(2.42) \quad \frac{d\rho^f}{dt} = -\operatorname{div} [\mathbf{m}^f] - \rho^f \operatorname{div} [\mathbf{v}].$$

In order to impose the incompressibility of the fluid, we first denote by $\rho_{0\text{ini}}^f$ the *initial* value of the fluid reference concentration. Recall that the fluid concentration with respect to the reference configuration evolves in time; $\rho_0^f = \rho_0^f(\mathbf{X}, t)$. Therefore we can precisely, and non-trivially, define $\rho_{0\text{ini}}^f(\mathbf{X})$:

$$\begin{aligned}
(2.43) \quad \rho_0^f(\mathbf{X}, 0) &=: \rho_{0_{\text{ini}}}^f(\mathbf{X}) \\
&= \rho_{\text{ini}}^f(\mathbf{x} \circ \boldsymbol{\varphi}) J(\mathbf{X}, t) \\
&= \frac{\rho^f(\mathbf{x} \circ \boldsymbol{\varphi}, t)}{J^{f_g}(\mathbf{X}, t)} J(\mathbf{X}, t) \\
&= \rho^f(\mathbf{x} \circ \boldsymbol{\varphi}, t) J^{f_e}(\mathbf{X}, t) \overset{\approx 1 \forall t}{\approx} \rho^f(\mathbf{x} \circ \boldsymbol{\varphi}, t).
\end{aligned}$$

In (2.43), $J := \det(\mathbf{F})$ and $J^{f_g} := \det(\mathbf{F}^{g^f})$. The quantity ρ_{ini}^f is defined by the right hand-sides of the first and second lines of (2.43). To follow the argument, consider, momentarily, a *compressible* fluid. If the current concentration, ρ^f , changes due to elastic deformation of the fluid and by transport, then ρ_{ini}^f as defined is not a physically-realised fluid concentration. It bears a purely mathematical relation to the current concentration, ρ^f , since the latter quantity represents the effect of deformation of a tissue point as well as change in mass due to transport at that point.

If the contribution due to mass change at a point is scaled out of ρ^f the quotient is identical to the result of dividing ρ_{ini}^f by the deformation only. This is expressed in the relation between the right hand-sides of the second and third lines of (2.43). The elastic component of fluid volume change in a pore is $J^{f_e} := \det(\mathbf{F}^{e^f})$, which appears in the third line of (2.43) via the preceding arguments. Clearly then, for a fluid demonstrating near incompressibility intrinsically (i.e., the true density is nearly constant), we have $J^{f_e} \approx 1$ as indicated. Equation (2.43) therefore shows that for a nearly incompressible fluid occupying the pores of a tissue, if we further assume that the pore structure deforms as the solid collagenous skeleton, $\rho_0^f(\mathbf{X}, 0) \approx \rho^f(\mathbf{x} \circ \boldsymbol{\varphi}, t)$; i.e., the fluid concentration as measured in the current configuration is approximately

constant in space and time. This allows us to write,

$$(2.44) \quad \frac{\partial}{\partial t} \left(\rho_{0\text{ini}}^f(\mathbf{X}) \right) \equiv 0 \Rightarrow \frac{\partial}{\partial t} \left(\rho^f(\mathbf{x} \circ \boldsymbol{\varphi}, t) \right) \Big|_{\mathbf{X}} = 0,$$

which is a hidden implication of our assumption of a homogeneous deformation, i.e., \mathbf{F} is the deformation gradient of solid collagen and the pore spaces. This leads to $\frac{d\rho^f}{dt} = 0$.¹⁰

We therefore proceed to treat our fluid mass transport at steady state. Rewriting the flux \mathbf{m}^f from Equation (2.42) as the product $\rho^f \mathbf{v}^f$ and using the result derived above,

$$(2.45) \quad \begin{aligned} 0 &= \frac{\partial \rho^f}{\partial t} \Big|_{\mathbf{X}} \\ &= -\text{div} [\rho^f \mathbf{v}^f] - \rho^f \text{div} [\mathbf{v}]. \end{aligned}$$

Returning to the solute mass transport relation (2.41) with this result,

$$(2.46) \quad \begin{aligned} \frac{d\rho^s}{dt} &= \pi^s - \text{div} \left[\widetilde{\mathbf{m}}^s + \frac{\rho^s}{\rho^f} \mathbf{m}^f \right] - \rho^s \text{div} [\mathbf{v}] \\ &= \frac{\rho^s}{\rho^f} \left(\underbrace{-\text{div} [\rho^f \mathbf{v}^f] - \rho^f \text{div} [\mathbf{v}]}_0 \right) \\ &\quad + \pi^s - \text{div} [\widetilde{\mathbf{m}}^s] - \mathbf{m}^f \cdot \text{grad} \left[\frac{\rho^s}{\rho^f} \right]. \end{aligned}$$

Thus, using the incompressibility condition (2.45), we get the simplified form of the balance of mass for an arbitrary solute species, s,

$$(2.47) \quad \frac{d\rho^s}{dt} = \pi^s - \text{div} [\widetilde{\mathbf{m}}^s] - \frac{\mathbf{m}^f \cdot \text{grad} [\rho^s]}{\rho^f} + \frac{\rho^s \mathbf{m}^f \cdot \text{grad} [\rho^f]}{\rho^{f2}}.$$

Using the pushed-forward form of the constitutive relationship for solute flux with respect to the fluid (2.36), this is now in standard advection-diffusion form,

¹⁰Which results in a very large pressure gradient driven flux due to incompressibility.

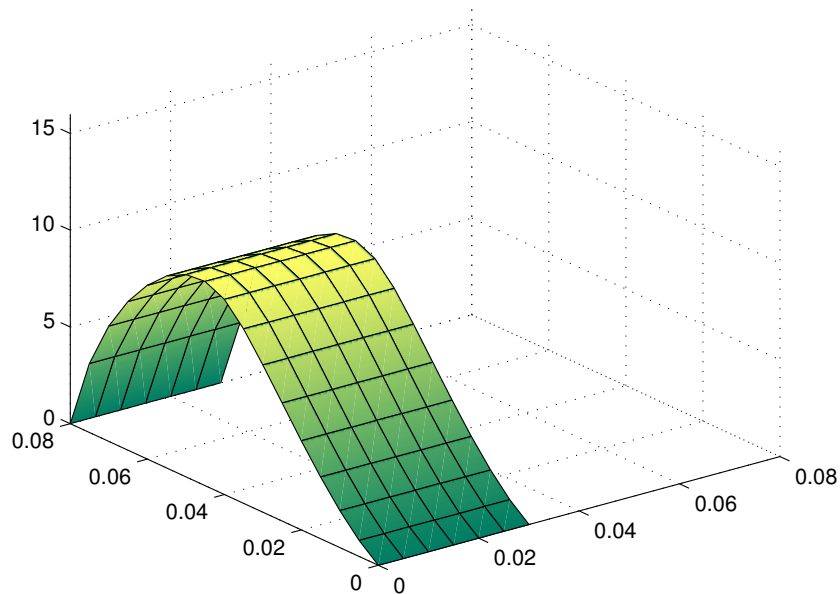


Figure 2.12: Smooth solution from a stabilised method ($Pe = 100$).

The streamline upwind Petrov-Galerkin method for the advection-diffusion equation is stable even at large Péclet numbers.

$$\begin{aligned}
 (2.48) \quad \frac{d\rho^s}{dt} - \underbrace{\operatorname{div} [\bar{\mathbf{D}}^s \operatorname{grad} [\rho^s]]}_{\text{Diffusion term}} - \underbrace{\pi^s}_{\text{Source term}} = \\
 - \underbrace{\frac{\mathbf{m}^f \cdot \operatorname{grad} [\rho^s]}{\rho^f}}_{\text{Advection term}} + \underbrace{\frac{\rho^s \mathbf{m}^f \cdot \operatorname{grad} [\rho^f]}{\rho^{f^2}}}_{\text{Additional, } \rho^s\text{-dependent source term}},
 \end{aligned}$$

where $\bar{\mathbf{D}}^s$ is a positive semi-definite diffusivity, \mathbf{m}^f/ρ^f is the advective velocity, and π^s is the volumetric source term. This form is well suited for stabilisation schemes such as the streamline upwind Petrov-Galerkin (SUPG) method¹¹ (see, for e.g., [Hughes et al. \(1987\)](#)), which limit spatial oscillations otherwise observed when the element Péclet number is large. Figure 2.12 shows the SUPG-stabilised solution for the simple advection-diffusion problem considered previously at an identical Péclet number.

¹¹Appendix B.2 provides, in weak form, the SUPG-stabilised method for Equation (2.48).

CHAPTER 3

Representative numerical simulations – I

Stemming in no small part from the physical richness of the system under consideration, the theoretical formulation presented in the preceding chapter resulted in a set of coupled, nonlinear partial differential equations governing the interrelated mechanical and biochemical processes underlying biological tissue growth.

In this chapter, a finite element implementation employing a staggered scheme is used to solve this system of equations for a varied class of numerical examples which aim to demonstrate the applicability of the theory, and study aspects of the coupled phenomena as the tissue grows. In Section 3.1, the numerical methods used for coupling reaction, transport and mechanics are outlined, and the computational model used in the simulations is introduced. The opening example, presented in Section 3.2, incorporates all of the theory discussed and acts as a model for localised, bolus delivery of regulatory chemicals to tendons while accounting for mechanical effects. In order to suppress some of the coupled phenomena, and take a closer look at the physics of porous soft tissues, Section 3.3 considers some examples based on a simplified system comprised only of a solid phase and a fluid phase.

3.1 Introducing the computational model

The mathematical formulation developed in Sections 2.1–2.4 has been implemented in a finite element setting using FEAP (Taylor, 1999), a general purpose

nonlinear finite element program. The implementation is in three-dimensions and uses eight-noded hexahedral elements.

The mass balance equation (2.40) for $\iota = f$ is solved to determine the current concentration field of the fluid phase,¹ ρ^f . The current concentration of the solute, ρ^s , is determined from the stabilised form of the mass balance equation provided in weak form in (B.1). The mass balance for the solid phase is solved in the reference configuration (Equation (2.2) for $\iota = c$) to obtain its reference concentration field, ρ_0^c , since there are no boundary conditions associated with this differential equation. Backward Euler is used as the time-stepping scheme for all mass balance equations.

In the implementation presented in this chapter, the tissue is viewed as a single entity when imposing the balance of momentum; and a summation of Equation (2.7) over $\iota = c, f$ is solved using the relation (2.10) for the common displacement field, \mathbf{u} , of the tissue and the fluid-filled pores.² Non-linear projection methods (Simo et al., 1985) based on hexahedral elements are used to treat the near-incompressibility imposed by the fluid, and mixed methods, as described in Garikipati and Rao (2001), are used for stress (and strain) gradient driven fluxes. Since the time scale for mass transport is much larger than that for mechanics, and since we are not focusing on inertial effects for the growth problems presented in this chapter, the momentum equation is solved as a quasi-static problem.³

The coupling between mass transport and mechanics is achieved by an iterative operator-splitting algorithm (Armero, 1999; Garikipati et al., 2001). Illustratively, in the simplest case of a biphasic problem involving no interconversion between species,

¹Recall from Section 2.4.1 that the physics of fluid-tissue interactions and the imposition of relevant boundary conditions are best understood and represented in the current configuration.

²The consequences of this simplification are explored in Section 3.3.1.

³The numerical experiments presented in Section 5.3 contrast the results obtained from quasi-static and dynamic calculations.

this algorithm, in explicit terms, reads:

At each time step, repeat:

- Fix the fluid concentration field; solve the mechanics problem for the displacement field, \mathbf{u}
- Fix the displacement field; solve the mass-transport problem for the concentration field, ρ^f

until both problems converge.

Its generalisation to other cases involving additional differential equations is straightforward.

The model geometry, based on the experimental work of [Calve et al. \(2004\)](#) on the engineering and characterisation of tendon-like constructs (see [Figure 3.1](#)), is a cylinder 12 mm in length and 1 mm² in cross-sectional area. The corresponding finite element mesh using 3840 hexahedral elements is shown in [Figure 3.2](#). The constitutive relation for the solid collagen phase uses the strain energy function arising from the eight-chain model incorporating worm-like chains, as discussed in [Section 2.3.2](#). The constitutive relation for the (ideal) fluid stress follows [\(2.29\)](#) with,

$$(3.1) \quad h(\rho^f) = \frac{1}{2} \kappa^f \left(\frac{\rho_{0\text{ini}}^f}{\rho^f} - 1 \right)^2,$$

where κ^f is the bulk modulus of the fluid.

The tissue is modelled as being fluid saturated in Ω_t at $t = 0$ s, i.e. [\(2.18₁\)](#) holds with $\rho_{0\text{sat}}^f = \rho_{0\text{ini}}^f$. However, the tissue is allowed to become unsaturated in Ω_t for $t > 0$ s due to void formation. Then, the conditions set out in [\(2.31\)](#) apply.

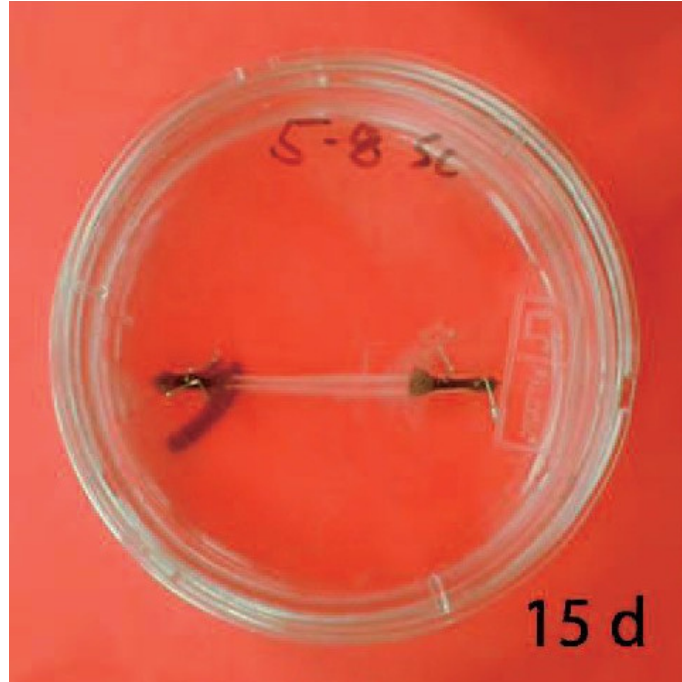


Figure 3.1: Engineered tendon construct (Calve et al., 2004).

The chemical potential is then given by (2.35). The numerical examples that follow discuss further specialisation of the constitutive relations to relevant cases.

The initial and boundary conditions have been chosen in order to model a few common mechanical and chemical interventions on engineered tissue, and the numerical values of parameters⁴ that have been used are relevant to tendons and appear in Table 3.1.

3.2 A multiphasic problem based on enzyme-kinetics

This first example can be viewed as a model for localised, bolus delivery of regulatory chemicals to the tendon while accounting for mechanical (stress) effects. A

⁴The mobility tensor reported in Table 3.1 is an order-of-magnitude estimate recalculated from Han et al. (2000) to correspond to the mobility used in this work. These authors reported a mean value of 0.927×10^{-14} s, with a range of $1.14 \times 10^{-14} - -0.58 \times 10^{-14}$ s in terms of the mobility used here. Theirs is the mobility parallel to the fibre direction in Rabbit Achilles tendon. Here, it is used as an isotropic mobility. Using anisotropic mobilities, or different values from the reported range changes the result quantitatively, but not qualitatively.

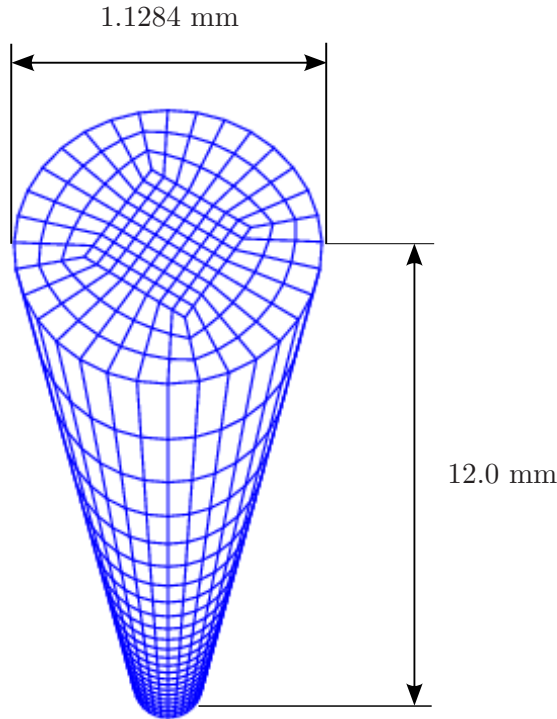


Figure 3.2: The finite element mesh used in the computations.

single solute species⁵, denoted by s , and a uniform distribution of fibroblasts that are characterised by their cell concentration, ρ_{cell} , are considered. Both Fickian diffusion of the solute and stress gradient driven fluid flow are incorporated in this illustration. Michaelis-Menten enzyme kinetics (2.38) is used to determine the rates of solute consumption and collagen production as a function of solute concentration. This nonlinear relationship for our choice of parameters is visualised in Figure 3.3. Here, the fluid phase does not take part in reactions, and hence $\pi^f = 0 \text{ kg}\cdot\text{m}^{-3}\cdot\text{s}^{-1}$.

The tendon immersed in the bath is subjected to a constrictive radial load, such as would be imposed upon manipulating it with a set of tweezers, as depicted in Figure 3.4. The maximum strain in the radial direction—experienced half-way through the height of the tendon—is 10%. The applied strain in the radial direction decreases

⁵Here, we envision the solute to be a protein playing an essential role in growth by catalysing biochemical reactions. An important example of this is a family of proteins, TGF β , which is a multi-functional peptide that controls numerous functions of many cell types (Alberts et al., 2002).

Parameter (Symbol)	Value	Units
Chain density (N)	7×10^{21}	m^{-3}
Temperature (θ)	310.6	K
Persistence length (A)	2.10	–
Fully-stretched length (L)	2.125	–
Unit cell axes (a, b, c)	1.95, 1.95, 2.43	–
Bulk compressibility factors (γ, β)	1000, 4.5	KPa, –
Fluid bulk modulus (κ^f)	1	GPa
Fluid mobility tensor ($D_{ij}^f = D^f \delta_{ij}$)	1×10^{-14}	s
Fibroblast concentration (ρ_{cell})	0.2	$\text{kg} \cdot \text{m}^{-3}$
Max. reaction rate ($k_{\text{max}} = 5$)	5	s^{-1}
Max. solute concentration (ρ_m^s)	0.2	$\text{kg} \cdot \text{m}^{-3}$
Solute diffusivity (D^s)	1×10^{-9}	$\text{m}^{-2} \text{s}$

Table 3.1: Material parameters used in the analysis.

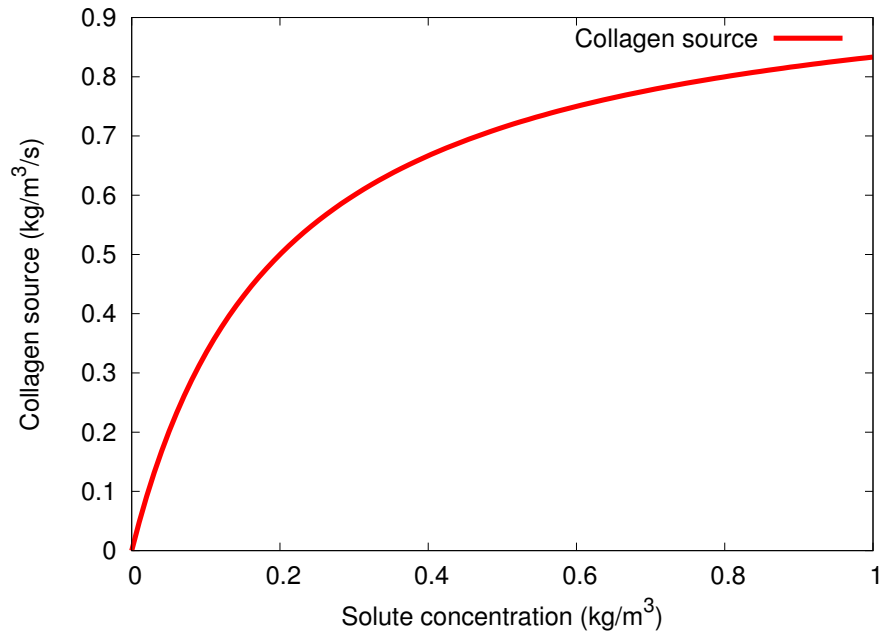


Figure 3.3: Variation of the collagen source with solute concentration.

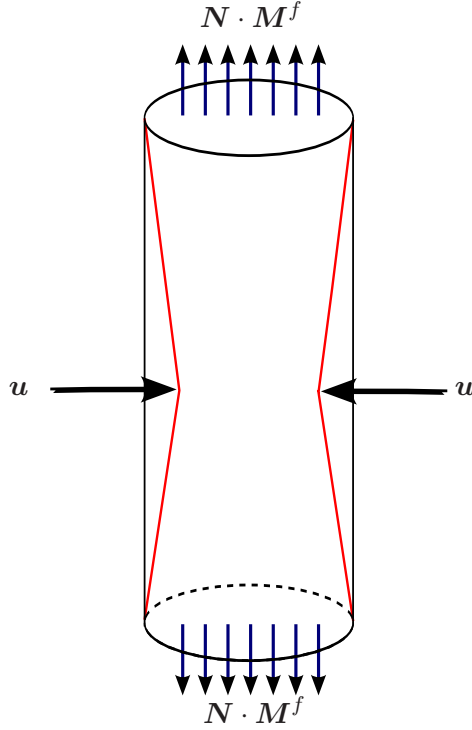


Figure 3.4: Constrictive load applied to the tendon immersed in a bath.

linearly with distance from the central plane, and vanishes at the top and bottom surfaces of the tendon.

The initial collagen concentration and the initial fluid concentration are both $500 \text{ kg}\cdot\text{m}^{-3}$ at every point in the tendon, and the fluid concentration in the bath is $500 \text{ kg}\cdot\text{m}^{-3}$. In addition, a solute-rich bulb of radius 0.15 mm is introduced with its centre on the axis of the tendon and situated 3 mm below the upper circular face of the tendon. The initial solute concentration is $0.05 \text{ kg}\cdot\text{m}^{-3}$ at all points in the tendon other than this solute-rich bulb, where the solute concentration increases linearly with decreasing radius to $1 \text{ kg}\cdot\text{m}^{-3}$ at its centre (see Figure 3.5).

The aim of this example is to compare the influences upon solute transport from two mechanisms: Fluid stress gradient-driven transport, arising from the applied constrictive load, and solute concentration gradient-driven transport. These mechanisms have both been implicated in nutrient supply to cells in soft tissue.

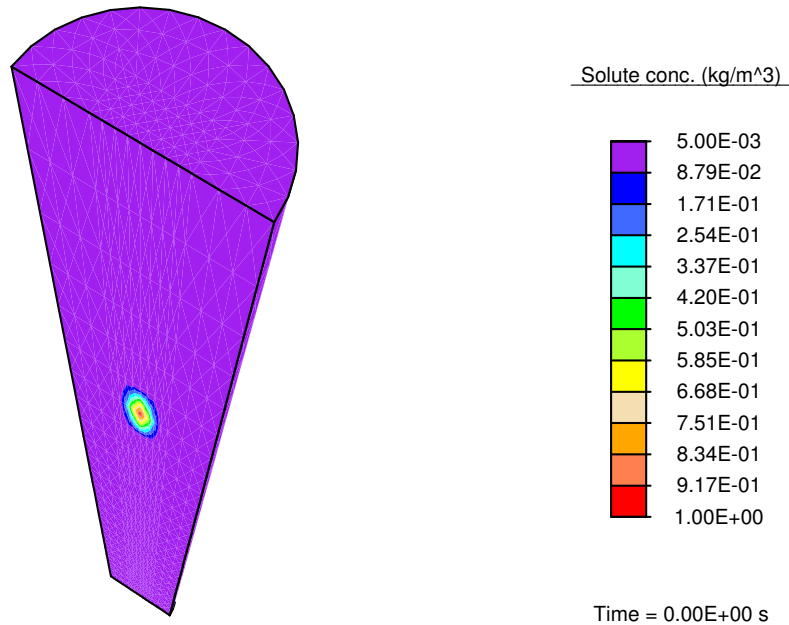


Figure 3.5: The solute concentration ($\text{kg}\cdot\text{m}^{-3}$) initially.

The results of this numerical example demonstrate that because the magnitude of the fluid mobility for stress gradient-driven transport is orders of magnitude smaller than the diffusion coefficient for the solute through the fluid, there is relatively only a small stress gradient-driven flux, and the transport of the solute is diffusion dominated. As a result, the solute diffuses locally, but displays no observable advection along the fluid at the time-scales considered. As the diffusion-driven solute concentration in a region increases, the enzyme-kinetics model results in a small source term for collagen production, and we observe nominal growth. Figure 3.6 shows the collagen concentration at an early time, $t = 5 \times 10^{-2}$ s.

This example incorporates all of the theory discussed in Chapter 2. However, in order to gain a better understanding of the flow-physics underlying this problem, it proves useful to simplify the setting and suppress some of the coupled phenomena. This is the approach followed in the next two numerical examples. The detailed

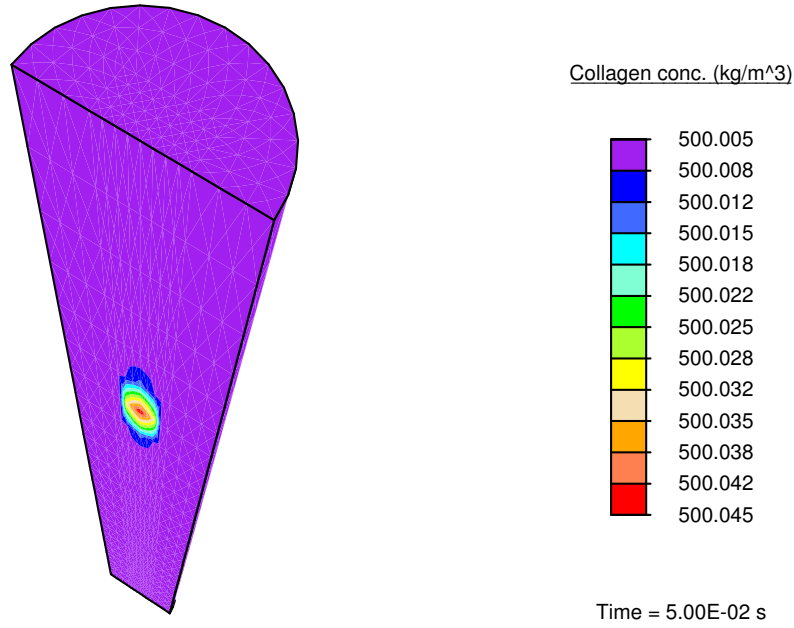


Figure 3.6: The collagen concentration ($\text{kg}\cdot\text{m}^{-3}$) at time $t = 5 \times 10^{-2}$ s.

transport and mechanics induced by the constrictive radial load are discussed first in Section 3.3.1.

3.3 Examples exploring the biphasic nature of porous soft tissue

In these calculations, only two phases—fluid and collagen—are included for the mass transport and mechanics. As before, the parameters used in the analysis are the same as those presented in Table 3.1.

3.3.1 The tendon under constriction

In this example, the tendon immersed in a bath is subjected to the same constrictive radial load as in Section 3.2. Since that example demonstrated an insignificant amount of local collagen production over the time scale of the test, we work with a simplified problem by setting the collagen source term $\Pi^c = 0$. The total duration of the simulation is 10 s, and the radial strain is applied as a displacement boundary

condition, increasing linearly from no strain initially to the maximum strain at time $t = 1$ s. Again, both the initial collagen concentration and the initial fluid concentration are 500 kg.m^{-3} at every point in the tendon. This tendon is exposed to a bath where the fluid concentration is 500 kg.m^{-3} .

As mentioned in Section 3.1, when solving the balance of momentum for the biphasic problem of the solid collagen and a fluid phase, the tissue is currently treated as a single entity, employing a summation of Equation (2.7) over both species. Additionally, condition (2.10) allows us to avoid constitutive prescription of the momentum transfer terms between solid collagen and fluid phases, \mathbf{q}^c and \mathbf{q}^f . This facilitates considerable simplification of the problem, but such a treatment requires additional assumptions on the detailed deformation of the constitutive phases of the tissue.

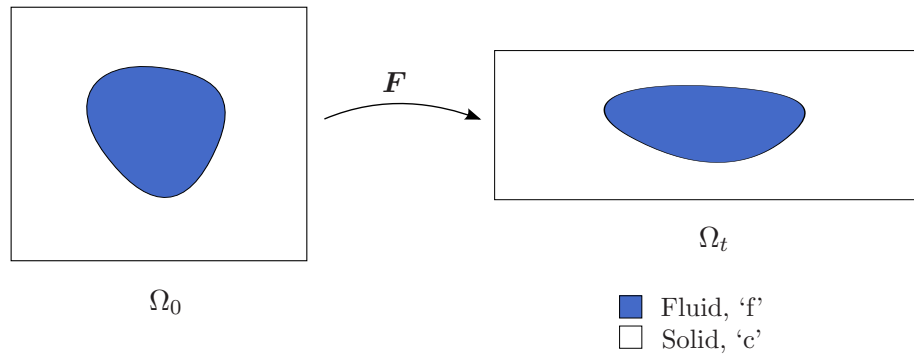


Figure 3.7: Upper bound model from strain homogenisation.

An implicit assumption we have drawn on thus far is the equality of the deformation gradient of the solid collagen and pore spaces, allowing us to use the deformation gradient \mathbf{F} , suitably decomposed to account for change in species concentration, to model the fluid stress. This assumption, depicted in Figure 3.7, had important consequences for the developments in Chapter 2.

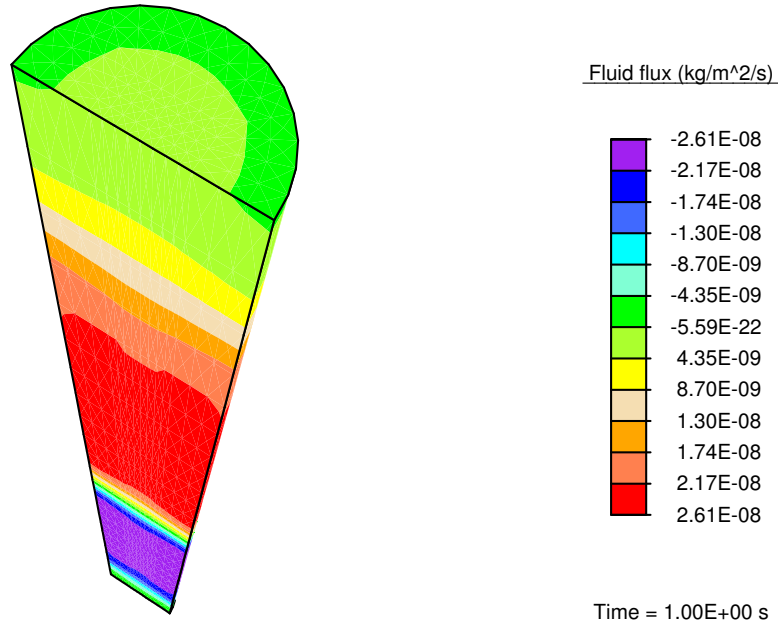


Figure 3.8: Upper bound vertical fluid flux ($\text{kg}\cdot\text{m}^{-2}\cdot\text{s}^{-1}$) at $t = 1$ s.

Since the imposition of a common deformation gradient results in an upper bound for the effective stiffness of the tissue and magnitudes of the fluxes established, we refer to it as the *upper bound model*. This assumption plays a fundamental role in determining the fluid flux driven by the fluid stress gradient.

For this upper bound model, Figure 3.8 shows the fluid flux in the vertical direction at the final stage of the constriction phase of the simulation, i.e. at time $t = 1$ s. The flux values are positive above the central plane, forcing fluid upward, and negative below, forcing fluid downward. This stress-gradient induced fluid flux results in a reference concentration distribution of the fluid that is higher near the top and bottom faces, as seen in Figure 3.9.

As a result, these regions would have seen a higher production of collagen, or preferential growth, in the presence of non-zero source terms. As discussed in Section 2.4.1, the mass transport equations are solved in the current configuration, where

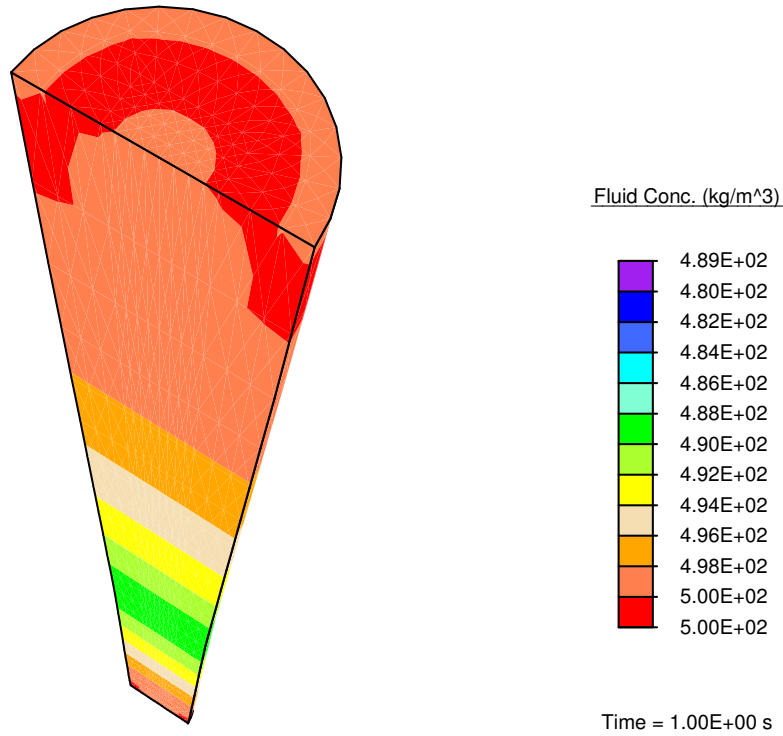


Figure 3.9: Reference fluid concentration ($\text{kg}\cdot\text{m}^{-3}$) at time $t = 1$ s.

physical boundary conditions can be set directly. The values reported in Figure 3.9 are pulled-back from the current configuration. The current concentrations do not change for this boundary value problem.

Solving a problem of this nature in the reference configuration, and setting ρ_0^f to a constant on the boundary to represent immersion of the tendon in a fluid bath yields non-physical results, such as an unbounded flow. This occurs since the imposed strain gradient causes a stress gradient in the fluid that does not decay. The imposed boundary condition on ρ_0^f prevents a redistribution of concentration that would have provided an opposing, internal gradient of stress, which in turn would drive the flux to vanish.

The tendon is held fixed in the radial direction after the constriction phase. The applied stress sets up a pressure wave in the fluid travelling toward the top and

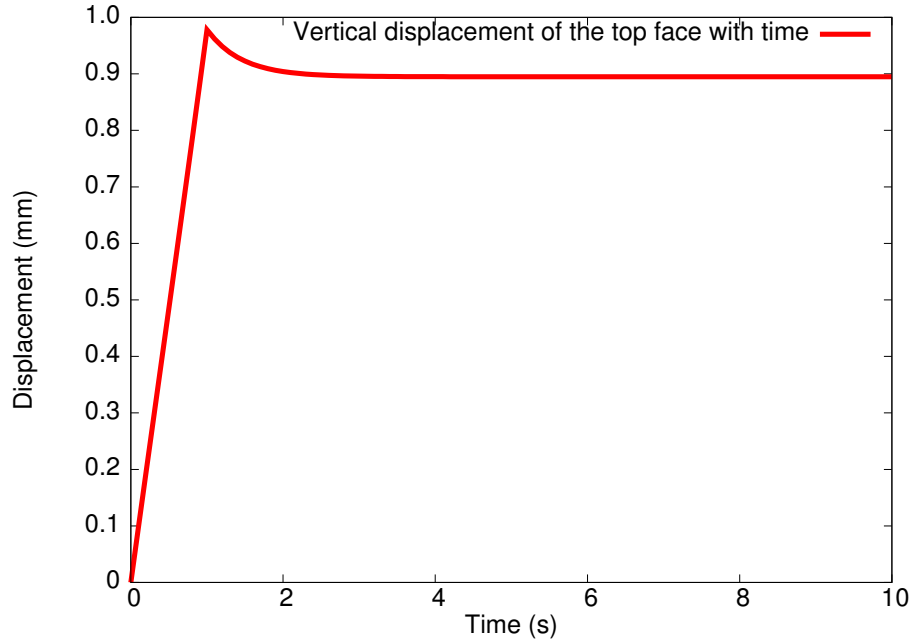


Figure 3.10: Relaxation of the top face of the tendon after constriction.

bottom faces. As the fluid leaves these surfaces, we observe that the tendon relaxes. This is seen in Figure 3.10, which plots the vertical displacement of the top face with time, showing a decrease in height of the tendon after the constriction phase. The centre of the bottom face of the tendon is kept fixed.

In order to define a range of the magnitude of fluid flux, we now introduce the *lower bound model* (on effective stiffness of the tissue and, consequently, the magnitude of the fluid flux). For this lower bound, we replace the earlier strain homogenisation requirement with a stress homogenisation requirement, *viz.* equating the hydrostatic stress of the solid phase and the fluid pressure in the current configuration:

$$(3.2) \quad p^f = \frac{1}{3} \text{tr}[\boldsymbol{\sigma}^c],$$

where p^f is the fluid pressure in the current configuration, $\text{tr}[\bullet]$ is the trace operator, and $\boldsymbol{\sigma}^c = \frac{1}{j^c} \mathbf{P}^c \mathbf{F}^{cT}$ is the Cauchy stress of the solid. The Cauchy stress of an

ideal fluid can be defined from its current pressure as $\sigma^f = p^f \mathbf{1}$. This assumption is depicted in Figure 3.11.

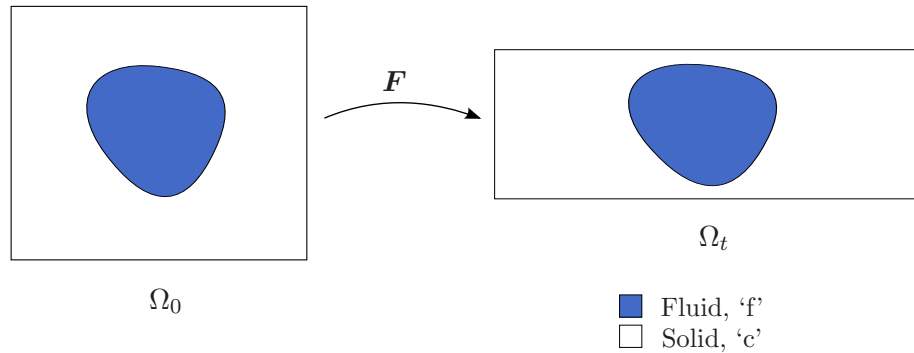


Figure 3.11: Lower bound model from stress homogenisation.

Figure 3.12 reports the value of the vertical flux under the lower bound modelling assumption, using boundary conditions identical to the previous calculation at time $t = 1$ s, the final stage of the constriction phase of the simulation.

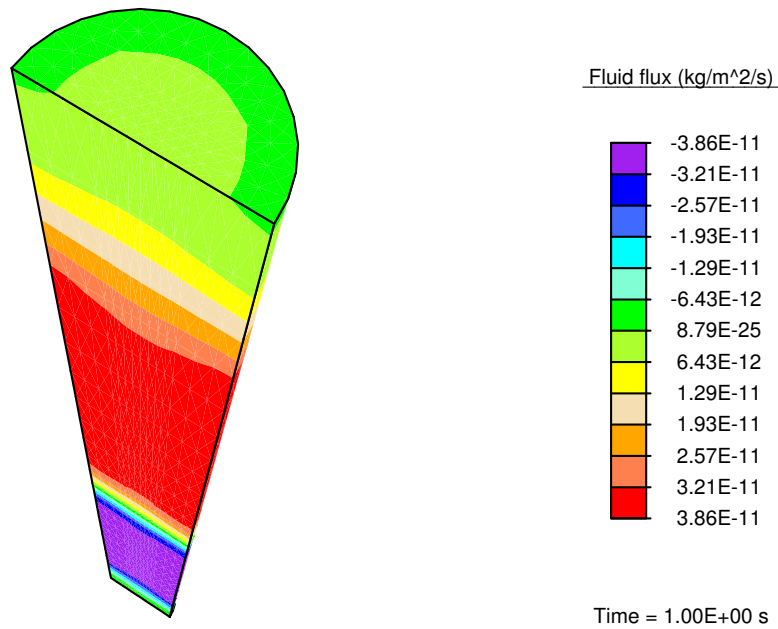


Figure 3.12: Lower bound vertical fluid flux ($\text{kg}\cdot\text{m}^{-2}\cdot\text{s}^{-1}$) at $t = 1$ s.

The fluid flux values reported in Figures 3.8 and 3.12 (corresponding to the upper and lower bound modelling assumptions, respectively) are qualitatively similar, but

differ by about three orders of magnitude. This wide range points to the importance of imposing the appropriate mechanical coupling model between interacting phases.⁶ Note, however, that we now have the range of possible fluid flux values under the specified mechanical loading. Recall, furthermore, that the example in Section 3.2 used the upper bound model, and yet resulted in no discernible advective solute transport. This suggests strongly that, given the parameters in Table 3.1, convective transport of nutrients in tendons is dominated by diffusive transport.

This numerical example also points to the fact that a convenient measure of the strength of coupling between the mechanics and mass transport equations is the ratio of the variation in hydrostatic stress of the fluid to that of the solid. In the lower bound case, where the fluid response is defined by Equation (3.2), it is instructive to note that this ratio is unity. As a result, it is seen that the lower bound case exhibits significantly weaker coupling than the upper bound case. In the latter, variation in the common deformation gradient, $\delta\mathbf{F}$, causes an instantaneous variation in $\delta p^f \approx O(\kappa^f \delta\mathbf{F} : \mathbf{F}^{-T})$ and in $\frac{1}{3}\delta\text{tr}[\boldsymbol{\sigma}^c] \approx O(\kappa^c \delta\mathbf{F} : \mathbf{F}^{-T})$, where κ^c is the bulk modulus of the solid. The ratio $\frac{\delta p^f}{\frac{1}{3}\delta\text{tr}[\boldsymbol{\sigma}^c]}$ is therefore $\approx O(\kappa^f/\kappa^c) \gg 1$.

The strength of coupling between the equations plays a principal role in the rate of convergence of the solution, as observed in Table 3.2, where the residual norms of the equilibrium equation (and corresponding CPU times in seconds for an Intel® Xeon 3.4 GHz machine) are reported for the first 8 iterations of each of the two cases. Recall that the staggered scheme involves solution of the mechanics equation keeping the concentrations fixed, and the mass transport equation keeping the displacements

⁶The computational implementation used in Chapter 5 models the mechanical coupling between the phases by specifying the momentum transfer terms, \mathbf{q}^t , between the solid and fluid phases. It works with these quantities by solving the *detailed* balance of momentum equations (i.e. a pushed-forward form of Equation (2.7) for each species individually), and obviates the need for either of these homogenisation assumptions.

Pass	Strongly coupled		Weakly coupled	
	Residual	CPU (s)	Residual	CPU (s)
1	2.138×10^{-02}	29.16	6.761×10^{-04}	28.5
	3.093×10^{-04}	55.85	1.075×10^{-04}	55.1
	2.443×10^{-06}	82.37	4.984×10^{-06}	81.8
	2.456×10^{-08}	109.61	1.698×10^{-08}	107.9
	4.697×10^{-14}	135.83	3.401×10^{-13}	134.1
	1.750×10^{-16}	163.18	1.152×10^{-17}	161.1
2	5.308×10^{-06}	166.79	5.971×10^{-08}	192.5
	4.038×10^{-10}	193.36	4.285×10^{-11}	218.6
	1.440×10^{-14}	220.45	2.673×10^{-15}	246.1
	4.221×10^{-17}	247.04		
3	5.186×10^{-06}	250.62	2.194×10^{-09}	277.3
	3.852×10^{-10}	277.44	2.196×10^{-13}	304.2
	1.369×10^{-14}	304.16	1.096×10^{-17}	331.6
	4.120×10^{-17}	331.47		
4	5.065×10^{-06}	335.16	8.160×10^{-11}	363.2
	3.674×10^{-10}	362.24	7.923×10^{-15}	390.2
	1.300×10^{-14}	388.79		
	4.021×10^{-17}	416.08		
5	4.948×10^{-06}	419.59	3.078×10^{-12}	421.4
	3.503×10^{-10}	446.24	3.042×10^{-16}	448.6
	1.236×10^{-14}	473.20		
	3.924×10^{-17}	500.85		
6	4.832×10^{-06}	504.65	1.179×10^{-13}	479.9
	3.340×10^{-10}	531.28	1.291×10^{-17}	507.0
	1.174×10^{-14}	558.17		
	3.829×10^{-17}	585.27		
7	4.720×10^{-06}	589.01	4.592×10^{-15}	537.8
	3.184×10^{-10}	616.24	5.152×10^{-18}	564.6
	1.116×10^{-14}	643.29		
	3.737×10^{-17}	670.83		
8	4.609×10^{-06}	674.46	1.816×10^{-16}	595.5
	3.034×10^{-10}	701.74	5.040×10^{-18}	622.3
	1.060×10^{-14}	727.74		
	3.646×10^{-17}	755.58		

Table 3.2: Mechanics equation residual norms.

Mechanics equation residual norms and corresponding CPU times in seconds for the first 8 passes of each of the two cases for a typical time increment, $\Delta t = 0.1$ s.

fixed, in turn, until the solution converges. The table does not report the value of the residual norms arising from the solution of the mass transport equation for the fluid, which occurs after each reported solve of the mechanics equation. Although the initial mechanics residual norms in successive passes are decreasing linearly in both cases, the rapid decrease in this quantity in the weakly-coupled case ensures convergence in far fewer iterations than the strongly coupled case. Thus, the corresponding CPU times reported are also significantly lower for the weakly coupled case, which is advantageous. In addition to being more physical, as argued below, the lower bound, weakly-coupled case makes it feasible to drive problems to longer, physiologically-relevant time-scales through the use of larger time steps. Motivated mainly by this recognition that the lower bound model for solid-fluid mechanical coupling ensures convergence to a self-consistent solution in just a few passes of the staggered solution scheme, it is used in the final example in this chapter.

Note that the individual balance of linear momentum equations for the solid collagenous and fluid phases with the momentum transfer terms ($\mathbf{q}^c, \mathbf{q}^f$ in (2.7)) is a statement of momentum balance between them. There is reason to suppose, therefore, that equating the solid collagen and fluid stress, or some component of these tensors as done in the lower bound model, is a reasonable approximation to explicitly solving the balance of linear momentum for each phase, including the momentum transfers, as carried out in Chapter 5. In contrast, equating the deformation gradient of the solid collagen with deformation of the pore spaces in the upper bound model subjects the fluid to a stress state also determined by this deformation gradient. This approximation does not correspond to an underlying physical principle comparable to the satisfaction of individual balances of linear momentum for the solid collagen and fluid, with momentum transfers.

3.3.2 A swelling problem

In this final example, we study the mechanical effects of growth due to collagen production. In the interest of focusing on this issue, we assume that fibroblasts are available, and that the fluid phase bears the necessary nutrients for collagen production dissolved at a suitable, constant concentration. Collagen production is assumed to be governed by a first-order rate law, as discussed in Section 2.3.7 (i). In this calculation, the reaction rate, k^f , is 0.07 s^{-1} .

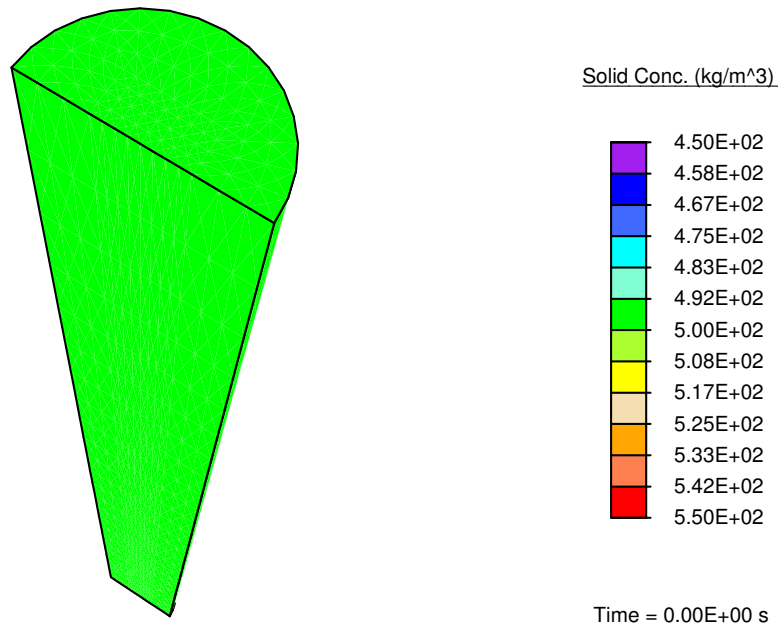


Figure 3.13: The initial collagen concentration ($\text{kg}\cdot\text{m}^{-3}$).

The boundary conditions in this example correspond to immersion of the tendon in a nutrient-rich bath. The initial constant collagen concentration is $500 \text{ kg}\cdot\text{m}^{-3}$ and the fluid concentration is $400 \text{ kg}\cdot\text{m}^{-3}$ at every point in the tendon. When this tendon is exposed to a bath where the fluid concentration is $410 \text{ kg}\cdot\text{m}^{-3}$, i.e. $\rho^f(\mathbf{x}, t) = 410 \text{ kg}\cdot\text{m}^{-3} \forall \mathbf{x} \in \partial\Omega_t$, nutrient-rich fluid is transported into the tissue due to the pressure difference induced by the concentration difference between the

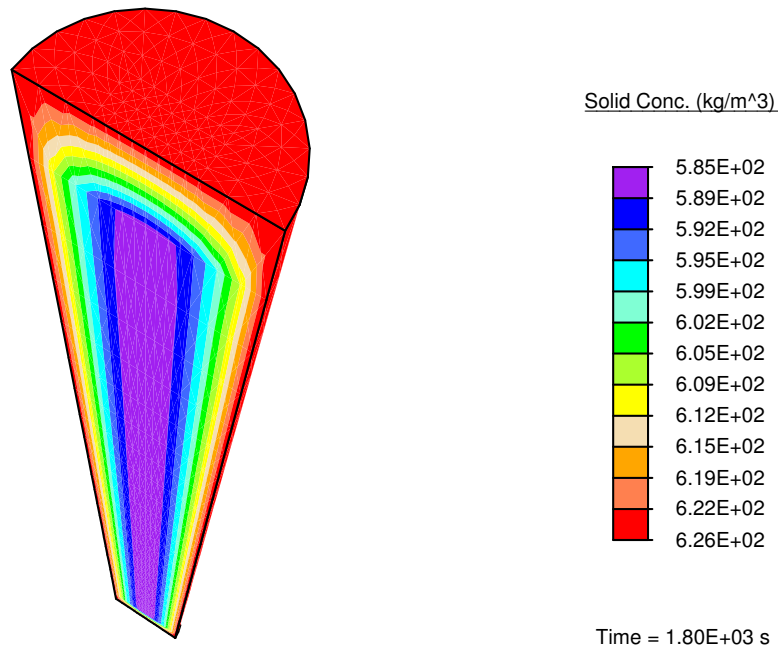


Figure 3.14: The collagen concentration ($\text{kg}\cdot\text{m}^{-3}$) after 1800 s.

fluid in the tendon and in the bath. Thereby, the nutrient concentration is elevated, leading to collagen production, fluid consumption and, eventually, growth due to the addition of collagen.

Figure 3.13 shows the initial collagen concentration in the tendon. After it has been immersed in the nutrient-rich bath for 1800 s, the tendon shows growth and the collagen concentration is higher, as seen in Figure 3.14. On performing a uniaxial tension test on the tendon before and after growth, it is observed (Figure 3.15) that the grown tissue is stiffer and stronger due to its higher collagen concentration. Qualitatively, this compares favourably with the experimental work of Arruda et al. (2005), where self-organised tendon constructs after growth induced by cyclic stretching are found to contain more collagen and become more stiff (see Figure 3.16).

There is a rapid, fluid transport-dominated swelling of the tendon between 0 and 25 s following immersion in the fluid bath (Figure 3.17). This causes a small

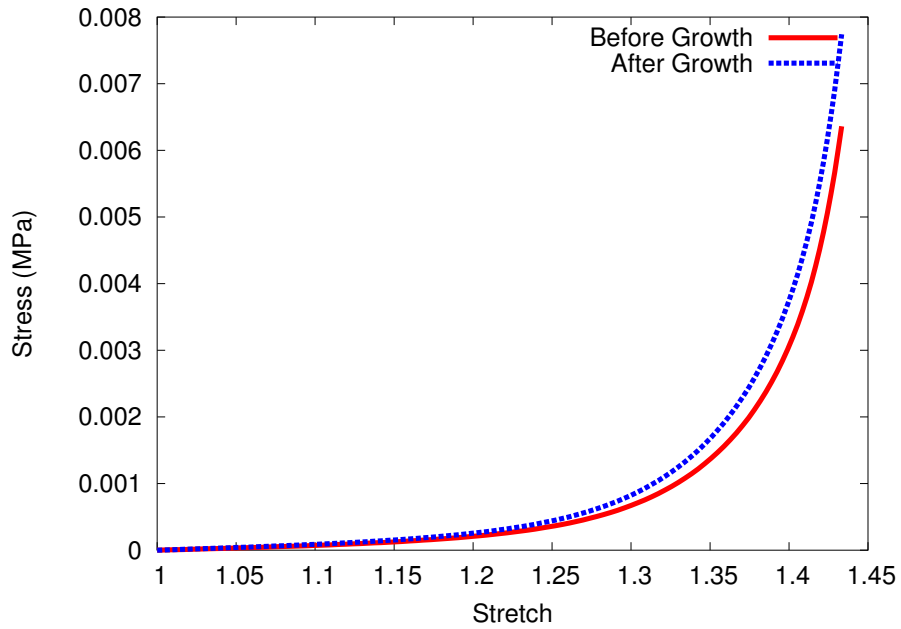


Figure 3.15: The stress (Pa) vs stretch curves before and after growth.

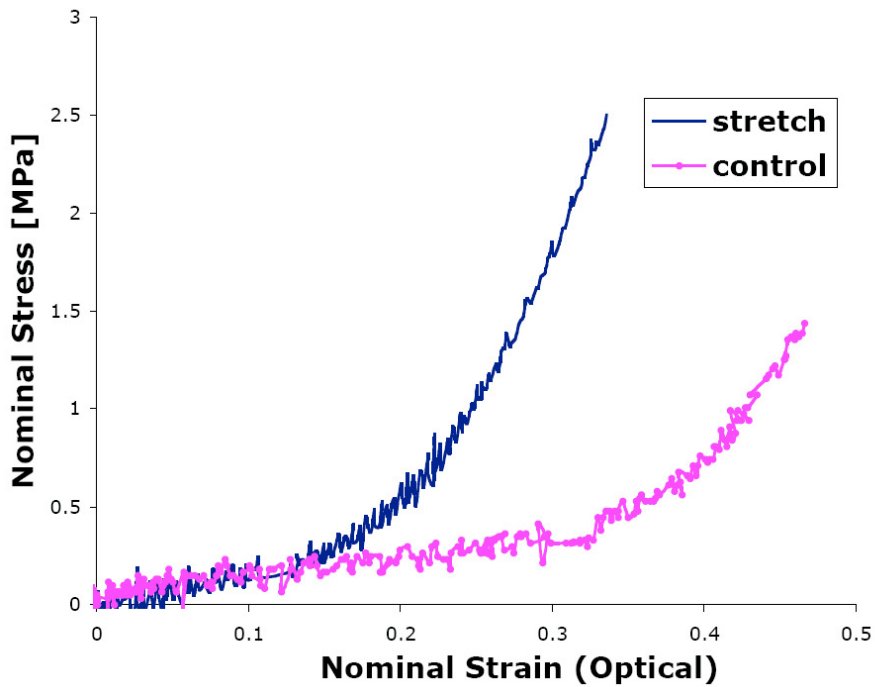


Figure 3.16: The tensile response of tendon constructs (Arruda et al., 2005).

The stress (MPa) vs strain response of self-organised tendon constructs before and after growth induced by cyclic stretching.

volume change of $\approx 1.6\%$. In this transport-dominated regime, the contribution to tendon growth from collagen production is small. However, the fluid-induced swelling saturates, and between 25 and 1800 s, the reaction producing collagen dominates the growth process, producing a further $\approx 6.8\%$ volume change. Noting that the range of collagen concentration in Figure 3.14 is $585 - 626 \text{ kg}\cdot\text{m}^{-3}$, and that (2.17) gives $\mathbf{F}^{\text{g}^c} = \left(\frac{\rho_0^c}{\rho_{0\text{ini}}^c}\right)^{\frac{1}{3}} \mathbf{1}$, this portion of the volume change is quite clearly due to collagen production. The total volume change of 8.4% corresponds to changes in each linear dimension of the tendon by only $\approx 2.7\%$, and is not discernible upon comparing Figures 3.13 and 3.14. It is, however, manifest in Figure 3.17.

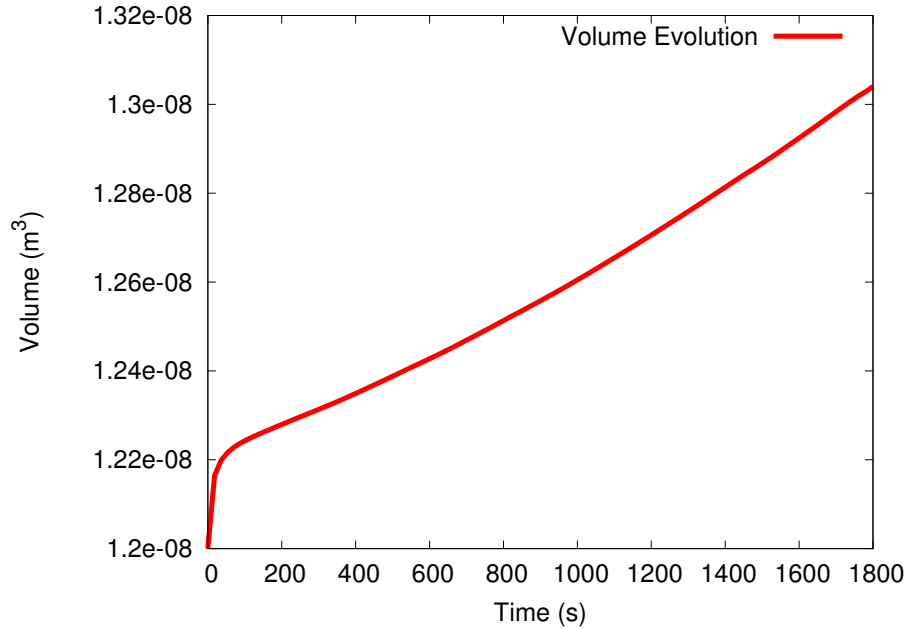


Figure 3.17: The volume of the tendon (m^3) evolving with time.

Note the fluid transported-dominated regime until 25 s, followed by the longer reaction-dominated growth stage.

CHAPTER 4

An Eulerian perspective

As detailed at the outset of Chapter 2, the continuum treatment presented thus far has stemmed from classical theories for solid continua, which are traditionally formulated in a Lagrangian setting. Since our continuum idealisation of tissues includes fluid components, and material coordinates are, in general, not known in fluid mechanics, this chapter revisits the derivation of the governing field equations of growing tissues following an Eulerian approach.

In this *spatial description*, attention is turned to a region of space coinciding with the *current configuration* of the tissue, where the evolution of field variables of interest is studied. Remarkably, this dissimilar approach results in a set of balance equations which is completely equivalent to that deduced in Section 2.1, just *pushed-forward* to the current configuration. But more significantly, the spatial approach presented below naturally leads to the identification of a different set of primitive variables more suitable to physically relevant boundary value problems.

This chapter is divided into two main parts. The first part (Section 4.1) briefly recapitulates the fundamental quantities characterising the tissue, pointing out noteworthy differences from Section 2.1, and derives the balance laws governing finite deformation growth in terms of spatial quantities. The second (Section 4.2), closes this set of balance laws by deducing a set of physiologically relevant constitutive relationships which ensure that the entropy production inequality is satisfied a priori.

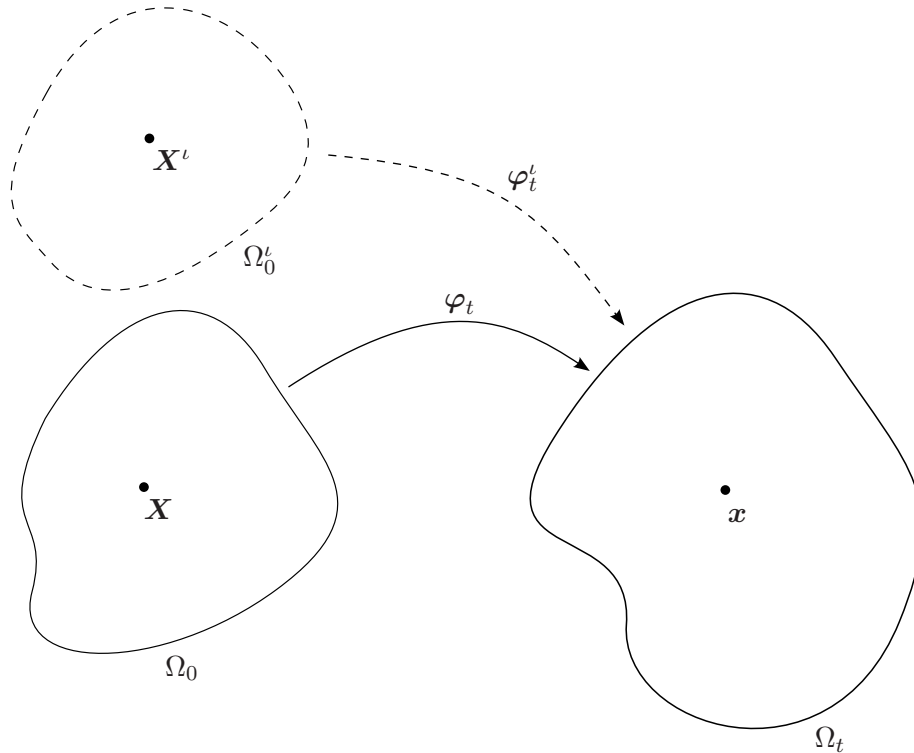


Figure 4.1: An Eulerian point of view.

4.1 Balance laws for an open mixture

We initiate this discussion with the introduction of Ω_t , a temporally-varying closure of an open set in \mathbb{R}^3 with a piecewise smooth boundary, which we define to be our region of interest. This region of interest is constructed to coincide with the current position of the solid component of the tissue, and our primary interest lies in the evolution of various field variables inside Ω_t , as observed from an inertial reference frame (Newton (1726), Corollary V, p. 423).

It is assumed that there exists a C^2 (in space and time), bijective and orientation preserving map $\varphi_t(\mathbf{X}) : \mathbb{R}^3 \times \mathbb{R}^+ \cup \{0\} \rightarrow \mathbb{R}^3$ such that $\Omega_t = \varphi_t(\Omega_0)$ for some convenient, *fixed* subset of \mathbb{R}^3 , Ω_0 . This ensures that Ω_t evolves in a well-behaved manner, disallowing non-physical deformations from being imposed on the tissue, and furthermore, affords the application of Reynolds' Transport Theorem

(Appendix A.2). The map φ_t is visualised in Figure 4.1.

Denoting a point in Ω_t by \mathbf{x} , $\mathbf{v}(\mathbf{x}, t) = \frac{\partial \varphi_t}{\partial t}$ defines the *spatial velocity* of the system domain. In contrast to Section 2.1, it is recognised at the outset that each species of the tissue is capable of undergoing its own motion independent of the tissue's solid component; and so we introduce the spatial velocity of an arbitrary species ι , $\mathbf{v}^\iota(\mathbf{x}, t)$, which is assumed to be C^1 in space and time.¹ Unlike the corresponding quantities defined in Section 2.1.2, these velocities are defined to be the *total* velocities of each species, not velocities relative to the solid component of the tissue.²

The following discussion of balance laws is carried out entirely in terms of an arbitrary species ι , and specialisation to the solid collagenous, fluid and solute phases (i.e. $\iota = c, f, s$) is reintroduced only in Section 4.2 when discussing constitutive relationships specific to these different components of the tissue.

4.1.1 Balance of mass

We now turn our attention to the evolution of the first of our field variables of interest, the current concentration of an arbitrary species ι constituting the system, $\rho^\iota(\mathbf{x}, t) : \mathbb{R}^3 \times \mathbb{R}^+ \cup \{0\} \rightarrow \mathbb{R}$. These are defined as the mass of species ι per unit *system volume*, Ω_t , and are assumed to be C^1 in time and C^2 in space. The total *spatial density* of the tissue can be obtained by their summation, $\sum_\iota \rho^\iota = \rho$.

With these quantities defined, we have from the conservation of matter for species ι over Ω_t ,

¹It is important to note that these quantities are primitive variables in themselves. While these species velocities can be formally understood as $\mathbf{v}^\iota(\mathbf{x}, t) = \frac{\partial \varphi_t^\iota}{\partial t}$, where φ_t^ι is the deformation map of each species ι from an arbitrary reference configuration to Ω_t (shown in the portion of Figure 4.1 constructed using dashed-lines), the quantities φ_t^ι are neither explicitly defined nor tracked.

²And, with the redefinition of these quantities as total velocities, the velocity of the solid phase ceases to be special. This is manifest in the forms of the balance laws deduced in Sections 4.1.1–4.1.4.

$$(4.1) \quad \underbrace{\frac{d}{dt} \left(\int_{\Omega_t} \rho^\iota \, dv \right)}_{\text{Rate of change of mass}} = \underbrace{\int_{\Omega_t} \pi^\iota \, dv}_{\text{Mass being created}} - \underbrace{\int_{\partial\Omega_t} \rho^\iota (\mathbf{v}^\iota - \mathbf{v}) \cdot \mathbf{n} \, da}_{\text{Mass leaving the domain}},$$

where $\pi^\iota(\mathbf{x}, t)$ is the volumetric source (or sink) of species ι , which specifies the species' mass production rate per unit system volume, and \mathbf{n} is the outward normal vector over $\partial\Omega_t$, the boundary of Ω_t . At this point, the only restriction on the source terms, $\pi^\iota(\mathbf{x}, t)$, is that they be integrable.

On applying Reynolds' Transport Theorem (Appendix A.2) to the left hand-side,

$$\int_{\Omega_t} \frac{\partial \rho^\iota}{\partial t} \, dv + \int_{\partial\Omega_t} \rho^\iota \mathbf{v} \cdot \mathbf{n} \, da = \int_{\Omega_t} \pi^\iota \, dv - \int_{\partial\Omega_t} \rho^\iota (\mathbf{v}^\iota - \mathbf{x}) \cdot \mathbf{n} \, da,$$

Gauss' Divergence Theorem (Appendix A.1) to the area integral,

$$\int_{\Omega_t} \frac{\partial \rho^\iota}{\partial t} \, dv = \int_{\Omega_t} \pi^\iota \, dv - \int_{\Omega_t} \operatorname{div}(\rho^\iota \mathbf{v}^\iota) \, dv,$$

and localising, we arrive at the final form of the balance of mass of species ι ,

$$(4.2) \quad \frac{\partial \rho^\iota}{\partial t} = \pi^\iota - \operatorname{div}(\rho^\iota \mathbf{v}^\iota) \quad \text{in } \Omega_t,$$

where $\operatorname{div}(\bullet)$ denotes the spatial divergence operator. This result is consistent with classical mixture theory (Truesdell and Toupin, 1960) and is the current configuration analogue of Equation (2.2).

As in Section 2.1.1, recall that for an external observer, the rate of change of mass of the entire system, affected only by external agents, is independent of interconversion between species. From the viewpoint of such an observer, the balance of mass for the tissue as a whole reads,

$$(4.3) \quad \frac{d}{dt} \sum_{\iota} \left(\int_{\Omega_t} \rho^{\iota} dv \right) = - \sum_{\iota} \int_{\partial\Omega_t} \rho^{\iota} (\mathbf{v}^{\iota} - \mathbf{v}) \cdot \mathbf{n} da.$$

Comparing Equation (4.3) to a summation of Equation (4.1) over all species, both being valid statements of the balance of mass of the tissue as a whole, it is clear that the sources and sinks satisfy,

$$(4.4) \quad \sum_{\iota} \pi^{\iota} = 0,$$

which specifies that, during biochemical interactions between species, the rate of consumption of the reactants equals the rate of creation of the products.

An identical relation is obtained by [Truesdell and Toupin \(1960\)](#) and others who follow their ideas (see, for e.g., [Bowen \(1976\)](#) and [Passman et al. \(1984\)](#)), but their deduction of this result, and other similar results involving quantities internal to the system (Equations (4.8) and (4.14)), stems from a formally stated assumption that “the mean response of a heterogeneous mixture obeys the ordinary equations of a continuum.” While we do not explicitly employ this assumption, it is implicit in our assertion that external observers can quantify field variables characterising species within a system without being aware of phenomena internal to the system.

4.1.2 Balance of linear momentum

We now look at how the momentum of a species evolves under the action of external agents, accounting for mass sources and allowing for the possibility that matter can leave the domain.

As observed from an inertial reference frame, the balance of momentum of a species ι over Ω_t requires,

$$\begin{aligned}
(4.5) \quad \underbrace{\frac{d}{dt} \left(\int_{\Omega_t} \rho^l \mathbf{v}^l \, dv \right)}_{\text{Rate of change of momentum}} &= \underbrace{\int_{\Omega_t} \rho^l (\mathbf{g}^l + \mathbf{q}^l) \, dv}_{\text{Resultant body force}} + \underbrace{\int_{\partial\Omega_t} \boldsymbol{\sigma}^l \mathbf{n} \, da}_{\text{Boundary traction}} \\
&+ \underbrace{\int_{\Omega_t} \pi^l \mathbf{v}^l \, dv}_{\text{Momentum being created}} - \underbrace{\int_{\partial\Omega_t} (\rho^l \mathbf{v}^l) (\mathbf{v}^l - \mathbf{v}) \cdot \mathbf{n} \, da}_{\text{Momentum leaving the domain}},
\end{aligned}$$

where, in addition to the quantities introduced previously, $\mathbf{g}^l(\mathbf{x}, t)$ is the resultant body force of *external* origin acting on species l , $\mathbf{q}^l(\mathbf{x}, t)$ is the resultant body force on species l from all other species *in the mixture*, and $\boldsymbol{\sigma}^l(\mathbf{x}, t)$ is the partial Cauchy stress on species l . The partial Cauchy stress tensor corresponding to species l is the portion of the total stress borne by the species. All of these quantities are assumed to be sufficiently smooth. In particular, \mathbf{g}^l and \mathbf{q}^l are assumed to be integrable, and $\boldsymbol{\sigma}^l$ is assumed to be C^1 in space and time.

Application of Reynolds' Transport Theorem (Appendix A.2) to the left hand-side of Equation (4.5) yields,

$$\begin{aligned}
\int_{\Omega_t} \frac{\partial(\rho^l \mathbf{v}^l)}{\partial t} \, dv + \int_{\partial\Omega_t} \cancel{(\rho^l \mathbf{v}^l) \mathbf{v} \cdot \mathbf{n}} \, da &= \int_{\Omega_t} \rho^l (\mathbf{g}^l + \mathbf{q}^l) \, dv + \int_{\partial\Omega_t} \boldsymbol{\sigma}^l \mathbf{n} \, da \\
&+ \int_{\Omega_t} \pi^l \mathbf{v}^l \, dv - \int_{\partial\Omega_t} (\rho^l \mathbf{v}^l) (\mathbf{v}^l - \boldsymbol{\nu}) \cdot \mathbf{n} \, da.
\end{aligned}$$

Using the product rule, Gauss' Divergence Theorem (Appendix A.1), and the balance of mass³ (Equation 4.2), we have,

$$\begin{aligned}
\int_{\Omega_t} \cancel{\frac{\partial \rho^l}{\partial t} \mathbf{v}^l} \, dv + \int_{\Omega_t} \rho^l \frac{\partial \mathbf{v}^l}{\partial t} \, dv &= \int_{\Omega_t} \rho^l (\mathbf{g}^l + \mathbf{q}^l) \, dv + \int_{\Omega_t} \text{div}(\boldsymbol{\sigma}^l) \, dv \\
&+ \int_{\Omega_t} \cancel{\pi^l \mathbf{v}^l} \, dv - \int_{\Omega_t} \cancel{(\text{div}(\rho^l \mathbf{v}^l) \mathbf{v}^l} + \text{grad}(\mathbf{v}^l) \rho^l \mathbf{v}^l) \, dv,
\end{aligned}$$

³Recognising that the balance of mass need not be satisfied exactly, pointwise, in a numerical implementation.

where $\text{grad}(\bullet)$ denotes the spatial gradient operator. Upon localisation, we obtain the final form of the balance of momentum of species ι ,

$$(4.6) \quad \rho^\iota \frac{\partial \mathbf{v}^\iota}{\partial t} = \rho^\iota (\mathbf{g}^\iota + \mathbf{q}^\iota) + \text{div}(\boldsymbol{\sigma}^\iota) - \text{grad}(\mathbf{v}^\iota) \rho^\iota \mathbf{v}^\iota \quad \text{in } \Omega_t,$$

which is a result consistent with classical mixture theory (Truesdell and Toupin, 1960) and is the current configuration analogue of Equation (2.7).

Neglecting the interaction terms as an external observer, the balance of momentum for the entire system can be written as follows,

$$(4.7) \quad \sum_\iota \frac{d}{dt} \left(\int_{\Omega_t} \rho^\iota \mathbf{v}^\iota \, dv \right) = \sum_\iota \left(\int_{\Omega_t} \rho^\iota \mathbf{g}^\iota \, dv + \int_{\partial\Omega_t} \boldsymbol{\sigma}^\iota \mathbf{n} \, da \right) - \sum_\iota \int_{\partial\Omega_t} (\rho^\iota \mathbf{v}^\iota) (\mathbf{v}^\iota - \mathbf{v}) \cdot \mathbf{n} \, da.$$

Comparing Equation (4.7) to a summation of Equation (4.5) over all species, it is clear that the sources and interaction forces satisfy the relation,

$$(4.8) \quad \sum_\iota (\rho^\iota \mathbf{q}^\iota + \pi^\iota \mathbf{v}^\iota) = 0,$$

which states that the momentum being introduced at a point due to the creation of matter has to be negated by momentum interactions with other species; ensuring that there is no mechanism for momentum production internal to the system.

4.1.3 Balance of angular momentum

Consider the position vector $\mathbf{p}(\mathbf{x})$ of a point on the tissue relative to a fixed point⁴ in space. The balance of angular momentum about \mathbf{p} , as observed from an inertial reference frame, of a species ι over Ω_t requires,

⁴Which may or may not be the origin of the system's Euclidean space.

$$\begin{aligned}
(4.9) \quad \underbrace{\frac{d}{dt} \left(\int_{\Omega_t} \mathbf{p} \times \rho^t \mathbf{v}^t \, dv \right)}_{\text{Rate of change of angular momentum}} &= \underbrace{\int_{\Omega_t} \mathbf{p} \times \rho^t (\mathbf{g}^t + \mathbf{q}^t) \, dv}_{\text{Moment from body forces}} + \underbrace{\int_{\partial\Omega_t} \mathbf{p} \times (\boldsymbol{\sigma}^t \mathbf{n}) \, da}_{\text{Moment from traction}} \\
&+ \underbrace{\int_{\Omega_t} \mathbf{p} \times \pi^t \mathbf{v}^t \, dv}_{\text{Angular momentum being created}} \\
&- \underbrace{\int_{\partial\Omega_t} (\mathbf{p} \times \rho^t \mathbf{v}^t) (\mathbf{v}^t - \mathbf{v}) \cdot \mathbf{n} \, da}_{\text{Angular momentum leaving the domain}},
\end{aligned}$$

since it is reasonable to assume that the material comprising the tissue is not a *polar material*.⁵

On applying Reynolds' Transport Theorem (Appendix A.2), Equation (4.9) reduces to,

$$\begin{aligned}
\int_{\Omega_t} \frac{\partial}{\partial t} (\mathbf{p} \times \rho^t \mathbf{v}^t) \, dv &= \int_{\Omega_t} \mathbf{p} \times \rho^t (\mathbf{g}^t + \mathbf{q}^t) \, dv + \int_{\partial\Omega_t} \mathbf{p} \times (\boldsymbol{\sigma}^t \mathbf{n}) \, da \\
&+ \int_{\Omega_t} \mathbf{p} \times \pi^t \mathbf{v}^t \, dv - \int_{\partial\Omega_t} (\mathbf{p} \times \rho^t \mathbf{v}^t) \mathbf{v}^t \cdot \mathbf{n} \, da.
\end{aligned}$$

Using Gauss' Divergence Theorem (Appendix A.1) and the product rule, we have the following relations:

$$\int_{\partial\Omega_t} \mathbf{p} \times (\boldsymbol{\sigma}^t \mathbf{n}) \, da = \int_{\Omega_t} \mathbf{p} \times \text{div} (\boldsymbol{\sigma}^t) \, dv + \int_{\Omega_t} \boldsymbol{\epsilon} : \boldsymbol{\sigma}^{tT} \, dv,$$

where $\boldsymbol{\epsilon}$ is the permutation symbol (introduced in Section 2.1.3),

$$\int_{\Omega_t} \frac{\partial}{\partial t} (\mathbf{p} \times \rho^t \mathbf{v}^t) \, dv = \int_{\Omega_t} \frac{\partial \rho^t}{\partial t} \mathbf{p} \times \mathbf{v}^t \, dv + \int_{\Omega_t} \rho^t \mathbf{p} \times \frac{\partial \mathbf{v}^t}{\partial t} \, dv, \quad \text{and}$$

$$\int_{\partial\Omega_t} (\mathbf{p} \times \rho^t \mathbf{v}^t) \mathbf{v}^t \cdot \mathbf{n} \, da = \int_{\Omega_t} \mathbf{p} \times \mathbf{v}^t \text{div} (\rho^t \mathbf{v}^t) \, dv + \int_{\Omega_t} \mathbf{p} \times (\text{grad} (\mathbf{v}^t) \rho^t \mathbf{v}^t) \, dv,$$

⁵Some materials, such as liquid crystals, become polarised under the presence of electric fields and consequently have additional global torque contributions to their balance of momentum equations (Truesdell and Noll, 1965).

since $\rho^t \mathbf{v}^t \times \mathbf{v}^t = 0$. Substituting these relations above and invoking the balance of mass (4.2) and the balance of linear momentum (4.6), we obtain on localisation that,

$$(4.10) \quad \boldsymbol{\epsilon} : \boldsymbol{\sigma}^{\prime T} = 0,$$

or the partial Cauchy stress tensor, $\boldsymbol{\sigma}^t$, is symmetric. This classical result is the pushed-forward form of the synonymous result derived earlier (Section 2.1.3) in terms of the partial first Piola-Kirchhoff stress tensor.

When the balance of angular momentum of the entire system, deduced by neglecting the interaction terms, is compared to the form of the equation obtained by summation of the individual balance of angular momenta (4.9) over all species present, one obtains a relationship between the interaction forces and interconversion terms that is identical to Equation (4.8).

4.1.4 Balance of energy

Recall from Section 2.1.4 that the internal energy per unit mass of species ι is denoted e^ι , the external heat supply to species ι per unit mass of that species is r^ι and the interaction energy, \tilde{e}^ι , accounts for the energy transferred to ι by all other species, also per unit mass of ι . We now denote the partial heat flux vector of ι defined on Ω_t as \mathbf{h}^ι , and for notational simplicity, introduce the total energy of each species ι per unit mass: $E^\iota = e^\iota + \frac{1}{2} \|\mathbf{v}^\iota\|^2$.

With these quantities defined, the rate of change of internal and kinetic energies of species ι under the action of mechanical loads, processes of mass production and transport, and heating and energy transfer, in Ω_t , is,

$$\begin{aligned}
(4.11) \quad \underbrace{\frac{d}{dt} \left(\int_{\Omega_t} \rho^\iota E^\iota \, dv \right)}_{\text{Rate of change of energy}} &= \underbrace{\int_{\Omega_t} \rho^\iota (\mathbf{g}^\iota + \mathbf{q}^\iota) \cdot \mathbf{v}^\iota \, dv}_{\text{Work done by body forces}} + \underbrace{\int_{\partial\Omega_t} (\boldsymbol{\sigma}^\iota \mathbf{n}) \cdot \mathbf{v}^\iota \, da}_{\text{Work done by boundary traction}} \\
&+ \underbrace{\int_{\Omega_t} \pi^\iota E^\iota \, dv}_{\text{Energy being created}} - \underbrace{\int_{\partial\Omega_t} (\rho^\iota E^\iota) (\mathbf{v}^\iota - \mathbf{v}) \cdot \mathbf{n} \, da}_{\text{Energy lost due to mass flux}} \\
&+ \underbrace{\int_{\Omega_t} \rho^\iota (r^\iota + \tilde{e}^\iota) \, dv}_{\text{Energy supplied}} - \underbrace{\int_{\partial\Omega_t} \mathbf{h}^\iota \cdot \mathbf{n} \, da}_{\text{Heat outflux}}.
\end{aligned}$$

On applying Reynolds' Transport Theorem (Appendix A.2) to the left hand-side and Gauss' Divergence Theorem (Appendix A.1) to the area integrals, we have,

$$\begin{aligned}
\int_{\Omega_t} \frac{\partial(\rho^\iota E^\iota)}{\partial t} \, dv &= \int_{\Omega_t} \rho^\iota (\mathbf{g}^\iota + \mathbf{q}^\iota) \cdot \mathbf{v}^\iota \, dv + \int_{\Omega_t} (\text{div}(\boldsymbol{\sigma}^\iota) \cdot \mathbf{v}^\iota + \boldsymbol{\sigma}^\iota : \text{grad}(\mathbf{v}^\iota)) \, dv \\
&+ \int_{\Omega_t} \pi^\iota E^\iota \, dv - \int_{\Omega_t} \text{div}(E^\iota \rho^\iota \mathbf{v}^\iota) \, dv \\
&+ \int_{\Omega_t} \rho^\iota (r^\iota + \tilde{e}^\iota) \, dv - \int_{\Omega_t} \text{div}(\mathbf{h}^\iota) \, dv.
\end{aligned}$$

Upon further simplification with the product rule and the balance of mass (4.2), we are left with:

$$\begin{aligned}
\int_{\Omega_t} \rho^\iota \frac{\partial E^\iota}{\partial t} \, dv &= \int_{\Omega_t} \rho^\iota (\mathbf{g}^\iota + \mathbf{q}^\iota) \cdot \mathbf{v}^\iota \, dv + \int_{\Omega_t} (\text{div}(\boldsymbol{\sigma}^\iota) \cdot \mathbf{v}^\iota + \boldsymbol{\sigma}^\iota : \text{grad}(\mathbf{v}^\iota)) \, dv \\
&- \int_{\Omega_t} \rho^\iota \mathbf{v}^\iota \cdot \text{grad}(E^\iota) \, dv \\
&+ \int_{\Omega_t} \rho^\iota (r^\iota + \tilde{e}^\iota) \, dv - \int_{\Omega_t} \text{div}(\mathbf{h}^\iota) \, dv.
\end{aligned}$$

We now expand the total energy of each species ι , $E^\iota = e^\iota + \frac{1}{2} \|\mathbf{v}^\iota\|^2$, and take its spatial and temporal derivatives to give,

$$\begin{aligned}
\int_{\Omega_t} \rho^\iota \left(\frac{\partial e^\iota}{\partial t} + \mathbf{v}^\iota \cdot \frac{\partial \mathbf{v}^\iota}{\partial t} \right) dv &= \int_{\Omega_t} \rho^\iota (\mathbf{g}^\iota + \mathbf{q}^\iota) \cdot \mathbf{v}^\iota dv \\
&+ \int_{\Omega_t} (\operatorname{div}(\boldsymbol{\sigma}^\iota) \cdot \mathbf{v}^\iota + \boldsymbol{\sigma}^\iota : \operatorname{grad}(\mathbf{v}^\iota)) dv \\
&- \int_{\Omega_t} \rho^\iota \mathbf{v}^\iota \cdot (\operatorname{grad}(e^\iota) + \operatorname{grad}(\mathbf{v}^\iota)^T \mathbf{v}^\iota) dv \\
&+ \int_{\Omega_t} \rho^\iota (r^\iota + \tilde{e}^\iota) dv - \int_{\Omega_t} \operatorname{div}(\mathbf{h}^\iota) dv.
\end{aligned}$$

Finally, we apply the balance of linear momentum (4.6) to the equation above and, upon localisation, arrive at:

$$(4.12) \quad \rho^\iota \frac{\partial e^\iota}{\partial t} = \boldsymbol{\sigma}^\iota : \operatorname{grad}(\mathbf{v}^\iota) + \rho^\iota (r^\iota + \tilde{e}^\iota) - \operatorname{div}(\mathbf{h}^\iota) - \rho^\iota \mathbf{v}^\iota \cdot \operatorname{grad}(e^\iota) \quad \text{in } \Omega_t,$$

the form of the balance of energy of a species ι in Ω_t which is most convenient for combining with the entropy inequality, leading to the Clausius-Duhem form of the dissipation inequality (4.17) in the following section. This result is consistent with classical mixture theory (Truesdell and Toupin, 1960) and is the current configuration analogue of Equation (2.14).

In order to obtain a relationship between the momentum transfer, mass interconversion and inter-species energy transfer terms within the system, we first express the rate of change of energy of the system interacting with its environment from the point of view of an external observer unaware of these internal interactions, as:

$$\begin{aligned}
\sum_\iota \frac{d}{dt} \left(\int_{\Omega_t} \rho^\iota E^\iota dv \right) &= \sum_\iota \int_{\Omega_t} \rho^\iota \mathbf{g}^i \cdot \mathbf{v}^\iota dv + \sum_\iota \int_{\partial\Omega_t} (\boldsymbol{\sigma}^\iota \mathbf{n}) \cdot \mathbf{v}^\iota da \\
(4.13) \quad &- \sum_\iota \int_{\partial\Omega_t} (\rho^\iota E^\iota) (\mathbf{v}^\iota - \mathbf{v}) \cdot \mathbf{n} da \\
&+ \sum_\iota \int_{\Omega_t} \rho^\iota r^\iota dv - \sum_\iota \int_{\partial\Omega_t} \mathbf{h}^\iota \cdot \mathbf{n} da.
\end{aligned}$$

Since the equation above, and a summation of Equation (4.11) over all ι are equivalent statements of the balance of energy for the entire system, it follows upon inspection and localisation that,

$$(4.14) \quad \sum_{\iota} (\rho^{\iota} \mathbf{q}^{\iota} \cdot \mathbf{v}^{\iota} + \pi^{\iota} E^{\iota} + \rho^{\iota} \tilde{e}^{\iota}) = 0,$$

which ensures that there is no net energy production mechanism internal to the system.

4.2 Thermodynamically-consistent constitutive framework

In order to close the system of balance equations deduced in Sections 4.1.1–4.1.4, and make thermodynamically-valid constitutive choices pertinent to biological tissues, we turn to the principles of entropy growth and material frame-indifference. The following treatment builds upon the same fundamental assumptions underlying our system of interest as those stated in Section 2.3:

- (i) The entropy production inequality is assumed to hold at a continuum point for all species as a whole, but, in general, not for each individual species.⁶
- (ii) All species occupying a continuum point in the tissue have the same absolute temperature, θ .

Additionally, in the derivation of the Clausius-Duhem form of the Second Law of Thermodynamics in Section 4.2.1 immediately below, we assume the viewpoint of an observer external to the system unaware of any internal interactions.

⁶Enforcing the entropy inequality separately for each of the individual constituents of the mixture imposes unrealistic constraints on the mixture (Bedford and Drumheller, 1983).

4.2.1 The Clausius-Duhem form

With the assumptions introduced above, and denoting by η^t the entropy per unit mass of species ι , the entropy inequality, when written out for the entire system in Ω_t reads,

$$(4.15) \quad \sum_{\iota} \underbrace{\frac{d}{dt} \left(\int_{\Omega_t} \rho^t \eta^t \, dv \right)}_{\text{Rate of change of entropy}} \geq \sum_{\iota} \underbrace{\int_{\Omega_t} \frac{\rho^t r^t}{\theta} \, dv}_{\text{Entropy supplied}} - \sum_{\iota} \underbrace{\int_{\partial\Omega_t} \frac{\mathbf{h}^t \cdot \mathbf{n}}{\theta} \, da}_{\text{Entropy outflux}} - \sum_{\iota} \underbrace{\int_{\partial\Omega_t} (\rho^t \eta^t) (\mathbf{v}^t - \mathbf{v}) \cdot \mathbf{n} \, da}_{\text{Entropy lost due to mass flux}}.$$

On applying Reynolds' Transport Theorem (Appendix A.2) to the left hand-side and Gauss' Divergence Theorem (Appendix A.1) to the area integrals, we have,

$$\begin{aligned} \sum_{\iota} \int_{\Omega_t} \frac{\partial(\rho^t \eta^t)}{\partial t} \, dv &\geq \sum_{\iota} \int_{\Omega_t} \frac{\rho^t r^t}{\theta} \, dv - \sum_{\iota} \int_{\Omega_t} \left(\frac{\text{div}(\mathbf{h}^t)}{\theta} - \frac{\mathbf{h}^t \cdot \text{grad}(\theta)}{\theta^2} \right) \, dv \\ &\quad - \sum_{\iota} \int_{\Omega_t} (\eta^t \text{div}(\rho^t \mathbf{v}^t) + \rho^t \mathbf{v}^t \cdot \text{grad}(\eta^t)) \, dv. \end{aligned}$$

Applying the product rule and the balance of mass (4.2),

$$\begin{aligned} \sum_{\iota} \int_{\Omega_t} \left(\rho^t \frac{\partial \eta^t}{\partial t} + \overset{\pi^t \eta^t}{\cancel{\eta^t \frac{\partial \rho^t}{\partial t}}} \right) \, dv &\geq \sum_{\iota} \int_{\Omega_t} \frac{\rho^t r^t}{\theta} \, dv \\ &\quad - \sum_{\iota} \int_{\Omega_t} \left(\frac{\text{div}(\mathbf{h}^t)}{\theta} - \frac{\mathbf{h}^t \cdot \text{grad}(\theta)}{\theta^2} \right) \, dv \\ &\quad - \sum_{\iota} \int_{\Omega_t} \left(\cancel{\eta^t \text{div}(\rho^t \mathbf{v}^t)} + \rho^t \mathbf{v}^t \cdot \text{grad}(\eta^t) \right) \, dv, \end{aligned}$$

and rearranging terms and localising, we have the following form of the entropy inequality for the entire system:

$$(4.16) \quad \sum_{\iota} \left(\rho^{\iota} \frac{\partial \eta^{\iota}}{\partial t} + \pi^{\iota} \eta^{\iota} \right) \geq \sum_{\iota} \left(\frac{\rho^{\iota} r^{\iota}}{\theta} - \rho^{\iota} \mathbf{v}^{\iota} \cdot \text{grad}(\eta^{\iota}) \right) - \sum_{\iota} \left(\frac{\text{div}(\mathbf{h}^{\iota})}{\theta} - \frac{\mathbf{h}^{\iota} \cdot \text{grad}(\theta)}{\theta^2} \right).$$

Now, multiplying Equation (4.16) by the temperature field, θ , and subtracting it from a summation of the balance of energy (4.12) over all species ι , we obtain,

$$\sum_{\iota} (\rho^{\iota} \dot{e}^{\iota} - \rho^{\iota} \dot{\eta}^{\iota} \theta - \pi^{\iota} \eta^{\iota} \dot{\theta}) \leq \sum_{\iota} \left(\boldsymbol{\sigma}^{\iota} : \text{grad}(\mathbf{v}^{\iota}) - \frac{\mathbf{h}^{\iota} \cdot \text{grad}(\theta)}{\theta} \right) + \sum_{\iota} \left(\rho^{\iota} \tilde{e}^{\iota} - \rho^{\iota} \mathbf{v}^{\iota} \cdot (\text{grad}(e^{\iota}) - \text{grad}(\eta^{\iota}) \theta) \right),$$

where $\dot{\bullet}$ denotes the partial derivative with respect to time. Using Equation (4.14) to eliminate the species interaction energy, \tilde{e}^{ι} , we deduce that

$$\sum_{\iota} (\rho^{\iota} \dot{e}^{\iota} - \rho^{\iota} \dot{\eta}^{\iota} \theta - \pi^{\iota} \eta^{\iota} \dot{\theta}) \leq \sum_{\iota} \left(\boldsymbol{\sigma}^{\iota} : \text{grad}(\mathbf{v}^{\iota}) - \frac{\mathbf{h}^{\iota} \cdot \text{grad}(\theta)}{\theta} \right) - \sum_{\iota} \rho^{\iota} \mathbf{v}^{\iota} \cdot (\text{grad}(e^{\iota}) - \text{grad}(\eta^{\iota}) \theta) - \sum_{\iota} \left(\rho^{\iota} \mathbf{q}^{\iota} \cdot \mathbf{v}^{\iota} + \pi^{\iota} \left(e^{\iota} + \frac{1}{2} \|\mathbf{v}^{\iota}\|^2 \right) \right).$$

Introducing the Helmholtz free energy per unit mass of species ι , $\psi^{\iota} = e^{\iota} - \theta \eta^{\iota}$, and regrouping terms, the relation above reduces to,

$$(4.17) \quad \sum_{\iota} \left(\rho^{\iota} \dot{e}^{\iota} - \rho^{\iota} \dot{\eta}^{\iota} \theta - \boldsymbol{\sigma}^{\iota} : \text{grad}(\mathbf{v}^{\iota}) + \frac{\mathbf{h}^{\iota} \cdot \text{grad}(\theta)}{\theta} \right) + \sum_{\iota} \left(\rho^{\iota} (\mathbf{q}^{\iota} + \text{grad}(e^{\iota}) - \text{grad}(\eta^{\iota}) \theta) \cdot \mathbf{v}^{\iota} + \pi^{\iota} \left(\psi^{\iota} + \frac{1}{2} \|\mathbf{v}^{\iota}\|^2 \right) \right) \leq 0.$$

the Clausius-Duhem (or reduced dissipation) inequality for the growth process; a rule which any prescribed constitutive relationship must satisfy (Truesdell and Toupin, 1960).

The form of the Clausius-Duhem inequality arrived at in (4.17) is equivalent to the forms in recent work on mixture theory-based models for biological growth (Loret and Simões, 2005; Ateshian, 2007). However, subsequently varying choices made in the different works, including this one, for the constitutive independent variables result in altered constitutive specification. I believe it is significant, and must be emphasised at this point that not only do the constitutive choices detailed in the following sections ensure that the Clausius-Duhem inequality is satisfied *a priori*, but also that they are general enough to handle a fairly large class of physics, and most significantly, have been implemented in a coupled formulation retaining much of their rich detail, as evidenced by the computational examples in Chapter 5.

4.2.2 Duhamel's law of heat conduction

A suitable constitutive relation motivated by experiment which relates the Cauchy heat flux vector $\mathbf{h}^\iota(\mathbf{x}, t)$ to the spatial temperature gradient $\text{grad}(\theta)(\mathbf{x}, t)$ is the classical heat conduction law of Duhamel:

$$(4.18) \quad \mathbf{h}^\iota = -\boldsymbol{\kappa}^\iota \text{grad}(\theta), \quad \forall \iota,$$

where $\boldsymbol{\kappa}^\iota(\mathbf{x}, t)$, the spatial thermal conductivity tensor, is positive semi-definite. The relation above states that heat flows down a temperature gradient, and using it ensures that the following portion of the Clausius-Duhem inequality (4.17),

$$\sum_{\iota} \left(\frac{\mathbf{h}^\iota \cdot \text{grad}(\theta)}{\theta} \right) \leq 0,$$

is satisfied since the heat conduction law (4.18) is valid for all species in the mixture.

In fact, the constitutive form (4.18) specified above was motivated directly by virtue of it being sufficient to ensure that the corresponding portion of the Clausius-

Duhem inequality had the appropriate sign. Another approach that can be followed to arrive at Duhamel's law (and, similarly, the constitutive relations that follow) is to first define a general set of independent variables upon which the various field variables can depend (such as in [Truesdell and Toupin \(1960\)](#)). One then proceeds to consider a scenario where the functional forms of some of the terms in the dissipation inequality are fixed, and examine the implications of entropy production on the remaining terms, assuming they can be varied independently.

In practice, the two approaches outlined above are mathematically equivalent, and the former is employed in the following treatment.

While Duhamel's law [\(4.18\)](#) is indeed useful in a general setting, our primary interest lies in specialising concepts from classical thermodynamics to biological systems, where the temperature field under most physiological scenarios is relatively uniform and constant in time. In what follows, we will restrict our attention to this case. Additionally, the general nature of the analysis thus far has resulted in it being presented in terms of an arbitrary species ι . Recall, from [Section 2.1](#), that the various species constituting the tissue are grouped into a solid species, consisting of solid *collagen fibrils* and *cells*, denoted by c , an extra-cellular *fluid* species, denoted by f , consisting primarily of water, and *solute* species, consisting of precursors to reactions, byproducts, nutrients, and other regulatory chemicals, denoted by s . We now return to this earlier classification, and motivated by specific portions of [\(4.17\)](#), proceed to prescribe constitutive relations pertinent to the mechanics and biochemistry of growing biological tissue for each of these species groups.

4.2.3 Energy-dependent mass source terms

We first focus on the following term of the Clausius-Duhem form [\(4.17\)](#),

$$\sum_{\iota=c,f,s} \pi^\iota \left(\psi^\iota + \frac{1}{2} \|\mathbf{v}^\iota\|^2 \right) \leq 0.$$

Recall that the extra-cellular fluid species, f, consists primarily of water and does not take part in reactions, i.e., $\pi^f = 0$. Therefore, from the summation relation for mass sources and sinks (4.4), we have that $\pi^s = -\pi^c$. Using this fact, the inequality above reads,

$$\pi^c \left(\psi^c + \frac{1}{2} \|\mathbf{v}^c\|^2 \right) + (-\pi^c) \left(\psi^s + \frac{1}{2} \|\mathbf{v}^s\|^2 \right) \leq 0.$$

The above relation provides a broad guideline that allows for the specification of a very general class of source terms for collagen. An obvious form that it suggests is linear in terms of the energy (Helmholtz free energy plus the kinetic energy) difference between the collagen phase and the solute phase:

$$(4.19) \quad \pi^c = -\kappa^c \left(\psi^c + \frac{1}{2} \|\mathbf{v}^c\|^2 - \psi^s - \frac{1}{2} \|\mathbf{v}^s\|^2 \right),$$

where κ^c is a non-negative rate constant.

Thus, the thermodynamics suggests that it is an energetic difference between the reactants and products of a chemical reaction that drive the reaction forward; a well-established concept in chemistry. More interestingly, since all that the thermodynamics requires is that the source term for collagen be positive (negative) when the solute is more (less) energetic than collagen, this opens up the selection to a variety of forms, such as the nonlinear (in terms of the energy difference) example shown below,

$$(4.20) \quad \pi^c = \epsilon \kappa^c \left(\exp \left[-\epsilon U \left(\psi^c + \frac{1}{2} \|\mathbf{v}^c\|^2 - \psi^s - \frac{1}{2} \|\mathbf{v}^s\|^2 \right) \right] - 1 \right)$$

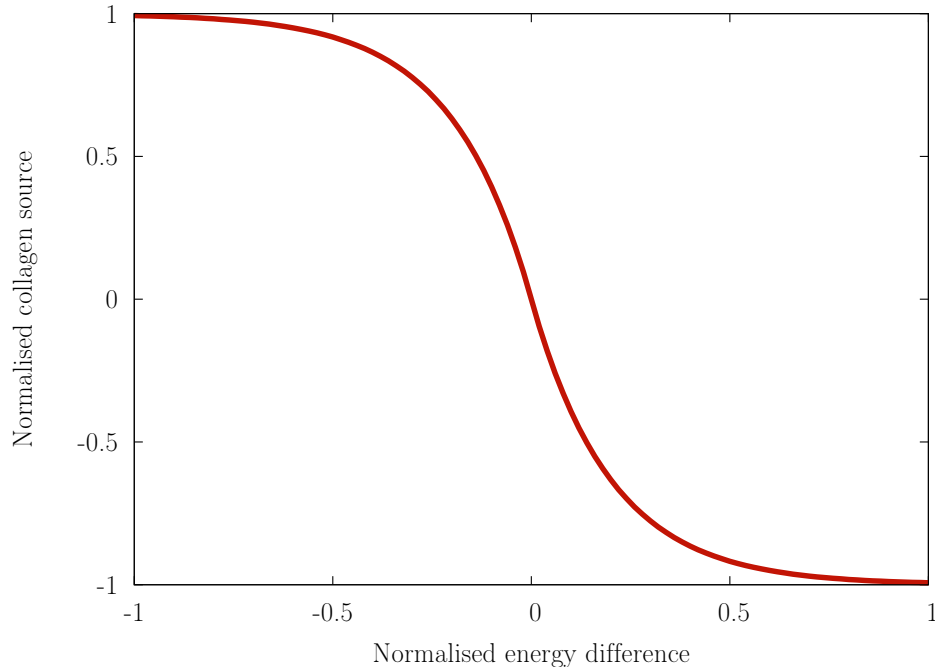


Figure 4.2: A thermodynamically-motivated collagen source.

(where $\epsilon = \text{sign}(\psi^c + \frac{1}{2}\|\mathbf{v}^c\|^2 - \psi^s - \frac{1}{2}\|\mathbf{v}^s\|^2)$, $U > 0$ and $\kappa^c \geq 0$), and can be tailored to represent different sorts of biochemistry. The evolution of this nonlinear collagen source term with the energy difference between the collagen and solute phases is shown in Figure 4.2; which clearly shows the source for collagen having a sign opposite to that of the energy difference between collagen and the solute.

With the introduction of an energy-dependent mass source (such as (4.19) or (4.20)), and drawing upon the assumption that the temperature field is uniform and constant⁷ during the course of a biological experiment, a portion of the Clausius-Duhem form (4.17) is satisfied a priori. The remainder now reads:

$$(4.21) \quad \sum_{\iota=c,f,s} \left(\rho^\iota \dot{\psi}^\iota - \boldsymbol{\sigma}^\iota : \text{grad}(\mathbf{v}^\iota) + \rho^\iota (\mathbf{q}^\iota + \text{grad}(\psi^\iota)) \cdot \mathbf{v}^\iota \right) \leq 0.$$

In the treatment that follows, recognising that the fluid, solid and solute are fun-

⁷Which allows one to write $\dot{e}^\iota - \dot{\eta}^\iota \theta = \dot{\psi}^\iota$ and $\text{grad}(e^\iota) - \text{grad}(\eta^\iota) \theta = \text{grad}(\psi^\iota)$.

damentally different substances, we turn to the specification of different constitutive independent variables most suited to each of them in deriving relevant constitutive relationships. Since our primary interest lies in the mechanics response of soft collagenous tissues, we will be paying particular attention to the constitutive forms of the solid collagen and fluid stress tensors, as well as the interaction forces between the collagen and fluid phases.

It is well established that collagenous tissues demonstrate a rate-dependent response to applied loads (see, for e.g., [Provenzano et al. \(2001\)](#)). This behaviour may be attributed to the viscoelastic deformation of the collagen network (which is the focus of [Section 4.2.4](#)), the viscosity of the extra-cellular fluid (as seen in [Section 4.2.6](#)), frictional effects arising from stress-driven fluid flow through the network (as discussed in [Section 4.2.7](#)), or combinations thereof. In order to be able to model each of these cases, the following sections derive the relevant constitutive relations entirely from thermodynamic considerations.

4.2.4 A viscoelastic solid

For the terms arising from the solid collagen phase, the reduced dissipation inequality ([4.21](#)) requires that,

$$\rho^c \dot{\psi}^c - \boldsymbol{\sigma}^c : \text{grad}(\mathbf{v}^c) + \rho^c \text{grad}(\psi^c) \cdot \mathbf{v}^c + \rho^c \mathbf{q}^c \cdot \mathbf{v}^c \leq 0.$$

We will return to the last term, $\rho^c \mathbf{q}^c \cdot \mathbf{v}^c$ when discussing interaction forces between the solid and fluid phases in [Section \(4.2.7\)](#). Currently, we turn our attention to the remaining terms in the inequality above:

$$(4.22) \quad \rho^c \dot{\psi}^c - \boldsymbol{\sigma}^c : \text{grad}(\mathbf{v}^c) + \rho^c \text{grad}(\psi^c) \cdot \mathbf{v}^c \leq 0.$$

Looking ahead to the numerical examples presented in Chapter 5, and noting that they solve the momentum balance equation (2.7) for the solid phase in the reference configuration,⁸ we deduce the constitutive response of the solid phase in terms of its partial first and second Piola-Kirchhoff stress tensors, \mathbf{P}^c and \mathbf{S}^c , respectively.

From the balance of angular momentum for the solid (4.10), we know that its partial Cauchy stress is symmetric and thus, $\boldsymbol{\sigma}^c : \text{grad}(\mathbf{v}^c) = \boldsymbol{\sigma}^c : (\dot{\mathbf{F}}\mathbf{F}^{-1}) = \frac{1}{J}\mathbf{P}^c : \dot{\mathbf{F}}$. Substituting this in (4.22) above, recalling that $\rho^c J = \rho_0^c$ and $\rho^c \dot{\psi}^c + \rho^c \text{grad}(\psi^c) \cdot \mathbf{v}^c$ provides the material time derivative of ψ^c , we have,

$$\rho_0^c \dot{\psi}^c - \mathbf{P}^c : \dot{\mathbf{F}} \leq 0, \text{ in } \Omega_0.$$

Introducing the elasto-growth kinematic split $\mathbf{F} = \mathbf{F}^e \mathbf{F}^g$ discussed in Section 2.2 for the solid phase, c, and applying the properties of the contraction operation, the above inequality reads,

$$\rho_0^c \dot{\psi}^c - \mathbf{P}^c \mathbf{F}^{gT} : \dot{\mathbf{F}}^e - \mathbf{F}^{eT} \mathbf{P}^c : \dot{\mathbf{F}}^g \leq 0.$$

The term $-\mathbf{F}^{eT} \mathbf{P}^c : \dot{\mathbf{F}}^g$ is the focus of the following section on stress-dependent growth deformation gradients (4.2.5). Currently, we consider only the following two terms,

$$(4.23) \quad \rho_0^c \dot{\psi}^c - \mathbf{P}^c \mathbf{F}^{gT} : \dot{\mathbf{F}}^e \leq 0.$$

As in Section 2.3.1, if we were to assume at this point that the Helmholtz free energy of the solid had the form, $\psi^c = \frac{1}{\rho_0^c} \hat{\psi}^c(\mathbf{F}^e)$, where $\tilde{\rho}_0^c$ is the intrinsic density

⁸It is instructive to note here that since Ω_t is constructed to coincide with the current position of the solid component of the tissue (see Section 4.1), we are aware of the deformation gradient $\mathbf{F}^c = \mathbf{F} = \frac{\partial \boldsymbol{\varphi}_t}{\partial \mathbf{X}}$ of this phase. This allows us to consistently pose the balance laws in either configuration.

of the solid collagen in the reference configuration, i.e., the free energy depends only upon the elastic portion of the deformation gradient, then a sufficient condition to satisfy the inequality above is to assume a hyperelastic model of the form:

$$(4.24) \quad \mathbf{P}^c = \frac{\rho_0^c}{\tilde{\rho}_0^c} \frac{\partial \hat{\psi}^c}{\partial \mathbf{F}^e} \mathbf{F}^{g^{-T}}.$$

We have already seen one specific form of this model used in the computations in Section 2.3.1.

However, we are currently interested in allowing for an inelastic response in the solid, and for this, we turn to a body of established work on continuum formulations for viscoelastic materials undergoing finite strains (see, for e.g., [Simo \(1987\)](#), [Holzapfel \(1996\)](#), and [Simo and Hughes \(1998\)](#)). The treatment below follows in the same vein.

We begin by assuming a Helmholtz free energy for the solid collagen of the form: $\psi^c = \frac{1}{\rho_0^c} \hat{\psi}^c(\mathbf{C}^e, \mathbf{\Gamma}_1, \dots, \mathbf{\Gamma}_m)$, where $\mathbf{C}^e = \mathbf{F}^{eT} \mathbf{F}^e$ is the elastic right Cauchy-Green tensor and $\mathbf{\Gamma}_1, \dots, \mathbf{\Gamma}_m$ are a set of second order tensorial internal history variables. Substituting this form into (4.23), and rewriting the partial first Piola-Kirchhoff stress tensor in terms of the partial second Piola-Kirchhoff stress tensor using the relation $\mathbf{P}^c = \mathbf{F} \mathbf{S}^c$, we have,⁹

$$(4.25) \quad \frac{\rho_0^c}{\tilde{\rho}_0^c} \frac{\partial \hat{\psi}^c}{\partial \mathbf{C}^e} : (2\mathbf{F}^{eT} \dot{\mathbf{F}}^e) + \sum_{\alpha=1}^m \frac{\rho_0^c}{\tilde{\rho}_0^c} \frac{\partial \hat{\psi}^c}{\partial \mathbf{\Gamma}_\alpha} : \dot{\mathbf{\Gamma}}_\alpha - (\mathbf{F}^e \mathbf{F}^g) \mathbf{S}^c \mathbf{F}^{gT} : \dot{\mathbf{F}}^e \leq 0.$$

A sufficient condition to satisfy (4.25) is to specify that the partial second Piola-Kirchhoff stress tensor has the form,

⁹The computations presented in Chapter 5 use the second partial Piola-Kirchhoff stress tensor, \mathbf{S}^c , since it is a symmetric quantity, and thus requires less memory for storage.

$$(4.26) \quad \mathbf{S}^c = \mathbf{F}^{\text{g}}^{-1} \frac{\rho_0^c}{\tilde{\rho}_0^c} 2 \frac{\partial \hat{\psi}^c}{\partial \mathbf{C}^e} \mathbf{F}^{\text{g}-\text{T}},$$

and provide a suitable evolution equation for the internal variables, Γ_α . Motivated by the fact that some compressible materials exhibit dissimilar bulk and shear response, we proceed to decompose the free energy function into volumetric and isochoric parts:

$$(4.27) \quad \hat{\psi}^c(\mathbf{C}^e, \Gamma_1, \dots, \Gamma_m) = \mathcal{W}_{\text{vol}}(J^e) + \mathcal{W}_{\text{iso}}(\bar{\mathbf{C}}^e) + \sum_{\alpha=1}^m \gamma_\alpha(\bar{\mathbf{C}}^e, \Gamma_\alpha),$$

where J^e is the determinant of the elastic portion of the deformation gradient tensor and $\bar{\mathbf{C}}^e = J^{e-2/3} \mathbf{C}^e$. The first two terms in the decomposition above characterise the volumetric and isochoric equilibrium response of the solid phase, and the last term is the dissipative potential which contributes to the viscoelastic response. The equilibrium response (that of a purely-elastic material) is recovered during infinitely slow processes.

Using the decomposition (4.27) in the stress constitutive relation (4.26), we see that the solid stress takes the form,

$$(4.28) \quad \mathbf{S}^c = \mathbf{F}^{\text{g}-1} \frac{\rho_0^c}{\tilde{\rho}_0^c} \left(\mathbf{S}_{\text{vol}}^c + \mathbf{S}_{\text{iso}}^c + \sum_{\alpha=1}^m \mathbf{Q}_\alpha \right) \mathbf{F}^{\text{g}-\text{T}},$$

where, denoting by \mathbb{I} the fourth order unit tensor,

$$\mathbf{S}_{\text{vol}}^c = J^e \frac{\partial \mathcal{W}_{\text{vol}}(J^e)}{\partial J^e} \quad \text{and} \quad \mathbf{S}_{\text{iso}}^c = J^{e-2/3} \left(\mathbb{I} - \frac{1}{3} \mathbf{C}^{-1} \otimes \mathbf{C} \right) : 2 \frac{\partial \mathcal{W}_{\text{iso}}(\bar{\mathbf{C}}^e)}{\partial \bar{\mathbf{C}}^e}.$$

Equation (4.28), along with the following evolution equations for the *non-equilibrium stresses*, \mathbf{Q}_α ,¹⁰ in agreement with the dissipation inequality motivated by a generalised Maxwell model,

¹⁰Which are work-conjugate variables to Γ_α .

$$(4.29) \quad \dot{\mathbf{Q}}_\alpha + \frac{\mathbf{Q}_\alpha}{\tau_\alpha} = \dot{\mathbf{S}}_{\text{iso}\alpha}^c, \quad \alpha = 1, \dots, m,$$

where each τ_α is a characteristic relaxation time and $\mathbf{S}_{\text{iso}\alpha}^c = \beta_\alpha \mathbf{S}_{\text{iso}}^c(\bar{\mathbf{C}}^e)$, where β_α is a non-negative strain-energy factor associated with τ_α , completes the specification of a linear viscoelastic solid. This can be extended in a straightforward manner to a nonlinear model by introducing the notion of a *modified relaxation time* (Eyring, 1936).

4.2.5 Effects of the stress state on tissue growth

One important influence that the local stress state has on tissue growth directly relates to its regulation of species production (and consumption) rates. An example of this fact lies in oft-cited work of Wolff (1892) who found that bone is deposited and resorbed in accordance with the stresses placed upon it. In this formulation, this effect is modelled through the use of the strain-energy dependent source terms (2.39) introduced in Section 2.3.7.

There is experimental evidence to suggest that there is another important influence of the stress state on the development of tissues, relating to the spatial alignment of deposited matter. An example of this is found in Provenzano et al. (2003), where it is observed that during wound healing, newly-deposited collagen fibres are found to align with the applied stress, whereas under unstressed conditions, they are deposited isotropically. Momentarily, will see that the thermodynamics naturally motivates a form for the rate of change of the growth deformation gradient tensor that reflects this observation.

During the derivation of the constitutive relationship for the solid stress in the preceding section, the implication of the following inequality,

$$-\mathbf{F}^{\text{eT}} \mathbf{P}^{\text{c}} : \dot{\mathbf{F}}^{\text{g}} \leq 0,$$

had not been explored. Turning our attention to it now, it is clear that a sufficient condition to satisfy this inequality is,

$$(4.30) \quad \dot{\mathbf{F}}^{\text{g}} = \lambda \mathbf{F}^{\text{eT}} \mathbf{P}^{\text{c}},$$

where λ is a non-negative scalar.

Equation (4.30) specifies that incremental changes in the growth deformation gradient in time have to be aligned along the partial first Piola-Kirchhoff stress tensor, suitably transformed by the elastic portion of the deformation gradient.

The treatment presented in Sections 4.2.4 and 4.2.5 involve the notion of deformation gradients and are thus only applicable to the solid collagen phase for reasons discussed. In contrast, the analyses for the fluid and solute phases below are carried out in Ω_t , and we work with their respective velocities as primitive variables characterising their motion.

4.2.6 A Newtonian fluid

As alluded to toward the end of Section 4.2.3, one of the mechanisms underlying the rate-dependent behaviour of soft collagenous tissues is the inherent viscosity of the extra-cellular fluid. In this section, we derive the constitutive relationship for a Newtonian (viscous) fluid from thermodynamic considerations.

For the terms arising from the fluid phase, the reduced dissipation inequality (4.21) requires that,

$$\rho^{\text{f}} \dot{\psi}^{\text{f}} - \boldsymbol{\sigma}^{\text{f}} : \text{grad}(\mathbf{v}^{\text{f}}) + \rho^{\text{f}} \text{grad}(\psi^{\text{f}}) \cdot \mathbf{v}^{\text{f}} + \rho^{\text{f}} \mathbf{q}^{\text{f}} \cdot \mathbf{v}^{\text{f}} \leq 0.$$

We will return to the last term, $\rho^f \mathbf{q}^f \cdot \mathbf{v}^f$, when considering interaction forces between the solid and fluid phases in Section (4.2.7). Now, we turn our attention to the remaining portion of the dissipation inequality for the fluid:

$$(4.31) \quad \rho^f \dot{\psi}^f - \boldsymbol{\sigma}^f : \text{grad}(\mathbf{v}^f) + \rho^f \text{grad}(\psi^f) \cdot \mathbf{v}^f \leq 0.$$

Assuming that the Helmholtz free energy of the fluid depends only on its current concentration, i.e., $\psi^f = \frac{1}{\tilde{\rho}^f} \hat{\psi}^f(\rho^f)$, where $\tilde{\rho}^f$ is the intrinsic density of the fluid, and substituting this form into (4.31), we have,

$$\frac{\rho^f}{\tilde{\rho}^f} \frac{\partial \hat{\psi}^f}{\partial \rho^f} \dot{\rho}^f - \boldsymbol{\sigma}^f : \text{grad}(\mathbf{v}^f) + \frac{\rho^f}{\tilde{\rho}^f} \frac{\partial \hat{\psi}^f}{\partial \rho^f} \text{grad}(\rho^f) \cdot \mathbf{v}^f \leq 0.$$

Invoking the balance of mass (4.2) for the fluid, with $\pi^f = 0$, we obtain,

$$\frac{\rho^f}{\tilde{\rho}^f} \frac{\partial \hat{\psi}^f}{\partial \rho^f} (-\rho^f \text{div}(\mathbf{v}^f)) - \boldsymbol{\sigma}^f : \text{grad}(\mathbf{v}^f) \leq 0.$$

Finally, recalling the definition of pressure in terms of the Helmholtz free energy at fixed temperature from classical thermodynamics, we have the following form of the reduced dissipation inequality for the fluid,

$$\left(-\frac{(\rho^f)^2}{\tilde{\rho}^f} \frac{\partial \hat{\psi}^f}{\partial \rho^f} \mathbf{1} - \boldsymbol{\sigma}^f \right) : \text{grad}(\mathbf{v}^f) \leq 0,$$

since $\text{div}(\bullet) = \mathbf{1} : \text{grad}(\bullet)$, where $\mathbf{1}$ is the second order identity tensor.

A suitable form for the partial Cauchy stress tensor of the fluid phase motivated by the above inequality is: $\boldsymbol{\sigma}^f = -p^f \mathbf{1} + 2\mu^f \text{grad}(\mathbf{v}^f)$, where μ^f , the viscosity of the fluid, is a non-negative scalar. Setting it to zero results in the case of an ideal fluid. Furthermore, recognising from the balance of angular momentum that $\boldsymbol{\sigma}^f$ is

symmetric, we rewrite the above constitutive relationship in terms of the fluid rate of deformation tensor, \mathbf{d}^f :

$$(4.32) \quad \boldsymbol{\sigma}^f = -p^f \mathbf{1} + 2\mu^f \mathbf{d}^f,$$

which defines the behaviour of a classical Newtonian fluid.

4.2.7 Frictional interaction forces

We now focus our attention on the following two terms that were left unaccounted for when exploring the implications of the terms arising from the solid and fluid phases in the reduced dissipation inequality (4.21) in Sections 4.2.4 and 4.2.6:

$$(4.33) \quad \rho^c \mathbf{q}^c \cdot \mathbf{v}^c + \rho^f \mathbf{q}^f \cdot \mathbf{v}^f \leq 0.$$

In the time-scales of experiments studying the mechanical response of tissues, growth is not usually significant, i.e. $\pi^c = \pi^f = 0$. Applying this simplification to the summation relationship between the interaction forces (4.8), we see that,

$$(4.34) \quad \rho^c \mathbf{q}^c = -\rho^f \mathbf{q}^f.$$

Substituting Equation (4.34) in (4.33), we obtain,

$$(4.35) \quad \rho^c \mathbf{q}^c \cdot (\mathbf{v}^c - \mathbf{v}^f) \leq 0.$$

Relationships (4.34) and (4.35) indicate that a suitable form for the interaction forces between the solid collagen and fluid phases are:

$$(4.36) \quad \rho^c \mathbf{q}^c = -\rho^f \mathbf{q}^f = -\mathbf{D}^{fc} (\mathbf{v}^c - \mathbf{v}^f),$$

where \mathbf{D}^{fc} is a positive semi-definite frictional coefficient tensor.¹¹ This frictional interaction between the phases is the basis for the time-dependent mechanical response observed in the biphasic computations presented in Section 5.3.

4.2.8 Diffusive solute fluxes

Since the solute species are present only in low concentrations in solution, they are not capable of exerting significant forces upon other phases, and do not bear appreciable stress. Consequently, for the solutes, the reduced dissipation inequality (4.21) requires only that,

$$\sum \left(\rho^s \dot{\psi}^s + \rho^s \text{grad}(\psi^s) \cdot \mathbf{v}^s \right) \leq 0,$$

where the summation above is carried out over all solute species. A sufficient condition to satisfy the above inequality is to specify the following form for the mass flux of each species s ,

$$(4.37) \quad \rho^s \mathbf{v}^s = -\mathbf{D}^s \text{grad}(\psi^s)$$

and only allow for solute interactions which decrease their overall free energy density. Here, \mathbf{D}^s is a positive semi-definite mobility, and Equation (4.37) results in classical diffusive flux of the solute species when their Helmholtz free energies are purely functions of their concentrations.

¹¹This is only the simplest form possible. See Massoudi (2003) for a thorough review of various thermodynamically and phenomenologically motivated forms for this interaction force.

CHAPTER 5

Representative numerical simulations – II

The theoretical framework developed in the preceding chapter resulted in a set of coupled partial differential equations governing the interrelated mechanics, mass transport and biochemistry pertinent to biological tissue growth. In order to demonstrate the applicability of the theory, this chapter presents the results of several illustrative numerical experiments posed within a corresponding computational framework retaining all aspects of the coupling between the equations.

The chapter begins by providing some insight into the numerical methods used to solve the coupled equations in Section 5.1. The first set of examples, presented in Section 5.2, serve to illustrate basic aspects of the coupled physics underlying biphasic models for tissue mechanics. In Section 5.3, the biphasic model parameters are tailored to be more representative of experimental studies on the mechanics of engineered ligaments, and aspects of the time- and rate-dependent behaviour of the model are explored. The final example presented in this chapter provides a straightforward extension of the theory to model the effects of the mechanical environment on growing tumours (Section 5.4), evidencing the generality of the proposed formulation.

5.1 Introducing the computational model

The mathematical formulation developed in Chapter 4 has been implemented in a finite element setting using COMSOL Multiphysics,¹ a computational environment for solving coupled systems of partial differential equations. For simplicity, the numerical implementation is in two spatial dimensions assuming a state of plane strain, and it uses triangular elements of order 2 (quadratic elements) to approximate the displacement field of the solid phase, and triangular elements of order 1 (linear elements) to approximate all other field variables, including the fluid velocity and concentration. A representative unstructured mesh, used in the computations on a unit square domain in Section 5.2, is shown in Figure 5.1 and consists of 3267 elements.

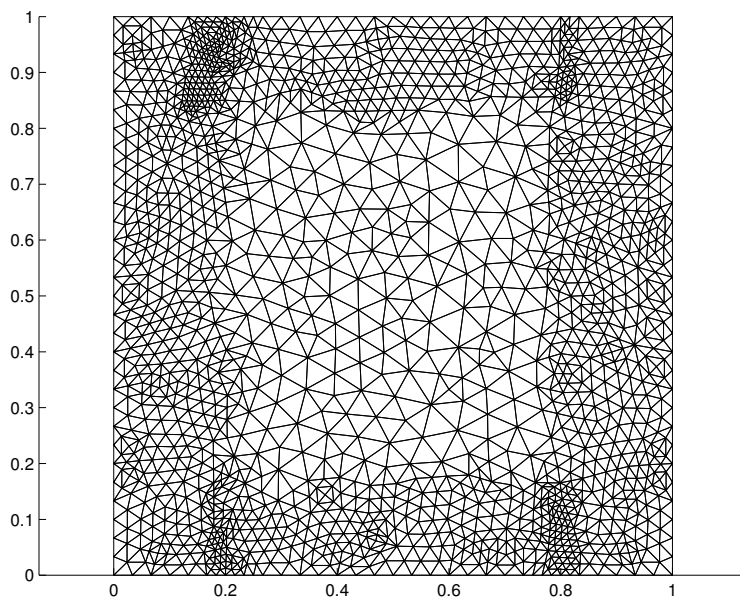


Figure 5.1: A representative finite element mesh used in the computations.

In the numerical implementation presented in Chapter 3, a simplified form of the

¹<http://www.comsol.com/>

balance of momentum was imposed by treating the tissue as a whole and solving a summation of Equation (2.7) over all species. This simplification necessitated additional assumptions on the underlying micro-mechanics, and these were discussed in Section 3.3.1. In contrast, the implementation used in this chapter solves the *detailed* momentum balance equations; enforcing the balance of momentum for each species separately. The coupling between the mechanics equations of the individual species is introduced by specifying momentum transfer terms, \mathbf{q}^ι , arising from frictional interaction as discussed in Section 4.2.7.

The balance of mass (2.2) and momentum (2.7) equations for the solid collagen are solved in the reference configuration of the tissue, Ω_0 , and the balance of mass (4.2) and momentum (4.6) equations for the fluid phase are solved in the current configuration, Ω_t . Recall that this choice is justified because we know the reference configuration of the solid phase of the tissue. These equations, along with the saturation constraint discussed below, are solved simultaneously for the solid concentration, ρ_0^c , and displacement, \mathbf{u}^c ; and the fluid concentration, ρ^f , velocity, \mathbf{v}^f , and pressure, p^f . Variable-order backward difference formulae (LeVeque, 2007) are used for forwarding the equations through time.

In the interest of generality, the formulation and corresponding implementation presented in Chapters 2 and 3 allowed for the possibility of cavitation in tissues under certain ex vivo/in vitro conditions. However, since it is well established that under normal physiological conditions soft tissues are fully saturated by the fluid, this condition will be imposed in the following calculations.

The concentration of each species ι can be expressed as the product of two non-negative scalar fields: $\rho^\iota = \phi^\iota \tilde{\rho}^\iota$, where ϕ^ι is the volume fraction and $\tilde{\rho}^\iota$ is the intrinsic density of species ι in Ω_t . The mixture is said to be saturated if the total

volume fraction, $\phi = \sum_t \phi^t = 1$ (Passman et al., 1984). Since the solute species are present only in very low concentrations, the preceding condition can be suitably approximated by:²

$$(5.1) \quad \frac{(\rho_0^c/J)}{\tilde{\rho}^c} + \frac{\rho^f}{\tilde{\rho}^f} = 1.$$

In this computational implementation, the fluid pressure, p^f , is not constitutively specified in terms of the current concentration of the fluid, and instead serves as a Lagrange multiplier to impose the saturation constraint (5.1).

For simplicity, in the calculations that follow, the strain energy function used for the elastic portion of the response of the solid collagen is the model of Mooney and Rivlin (Mooney, 1940):

$$(5.2) \quad \hat{\psi}^c(\mathbf{C}^e) = \sum_{i,j=0}^n C_{ij}(I_1 - 3)^i(I_2 - 3)^j$$

(where I_1 and I_2 are the first and second principal invariants of the elastic right Cauchy-Green tensor, \mathbf{C}^e), suitably decomposed into volumetric and isochoric parts. A mixed displacement-pressure (Zienkiewicz and Taylor, 1989) formulation is used to treat the near-incompressibility of the solid phase. Also for simplicity, the fluid is assumed to be ideal, i.e. the fluid viscosity, $\mu^f = 0$ Pa.s.

5.2 Some simple physical tests

The preliminary calculations presented in this section aim to illustrate basic aspects of the coupled physics that arise in mixture models that include only two

²The saturation condition, as stated in Equation (5.1), incorporates an implicit assumption that the solid and fluid phases of the tissue are individually *intrinsically* incompressible. This means that their intrinsic densities, $\tilde{\rho}^t$, do not change under load, and this is a common assumption employed in the soft tissue mechanics literature. (See, for e.g., Mow et al. (1980) and Ateshian (2007).)

non-reacting phases: a solid and a fluid. In these calculations, the tissue is assumed to be 1 mm thick and the material model for the solid phase uses the Mooney-Rivlin strain energy function (5.2) with just one term (i.e., it is neo-Hookean) having the material constant $C_{10} = 0.8$ MPa.

5.2.1 An inflating balloon

This example studies the inflation of the tissue as a result of pressure-gradient driven influx of fluid. The total duration of the test is 3 s. The initial concentrations of the solid collagen and fluid phases at all points in a unit square domain (1 mm \times 1 mm) are 500 kg.m⁻³, and their intrinsic densities are 1000 kg.m⁻³. Thus, each phase has an initial volume fraction of 0.5. At the initial time, the solid displacement and velocity fields, and the fluid velocity and pressure fields are each 0 in their respective units at all points in the domain.

In this example, the frictional coefficient tensor, $\mathbf{D}^{\text{fc}} = 1e^{-5} \mathbf{1}$ MPa.s.mm⁻², is assumed to have a relatively small magnitude because we are currently more interested in observing the swelling of the domain due to fluid influx rather than the frictional interaction between the phases.

The boundary conditions for this problem correspond to holding the bottom edge of the tissue fixed to prevent rigid body motion, and forcing inflow of the fluid at this bottom edge while disallowing outflow at any of the other edges, simulating an inflating balloon. In particular:

- For the fluid, the boundary condition on the bottom edge specifies that its pressure increases linearly in time from 0 MPa to 0.3 MPa during the duration of this test. The boundary condition for the fluid on the other three edges specifies that its velocity field is the same as that of the solid, $\mathbf{v}^{\text{f}} = \mathbf{v}^{\text{c}}$, disallowing outflow

of fluid.

- For the solid, the boundary condition on the bottom edge fixes the components of the solid displacement to 0 mm for the entire duration of the test. On the other three edges, following literature on fluid-structure interaction (Donea et al., 2004), there is a traction boundary condition on the solid that reads, $\mathbf{t}^c = \boldsymbol{\sigma}^c \mathbf{n} = -p^f \mathbf{n}$, suitably pulled-back to the reference configuration. Here, \mathbf{n} is the normal to Ω_t , and this condition relates the stress in the solid to the pressure in the fluid along the edges where there is no relative motion between the solid and the fluid.³

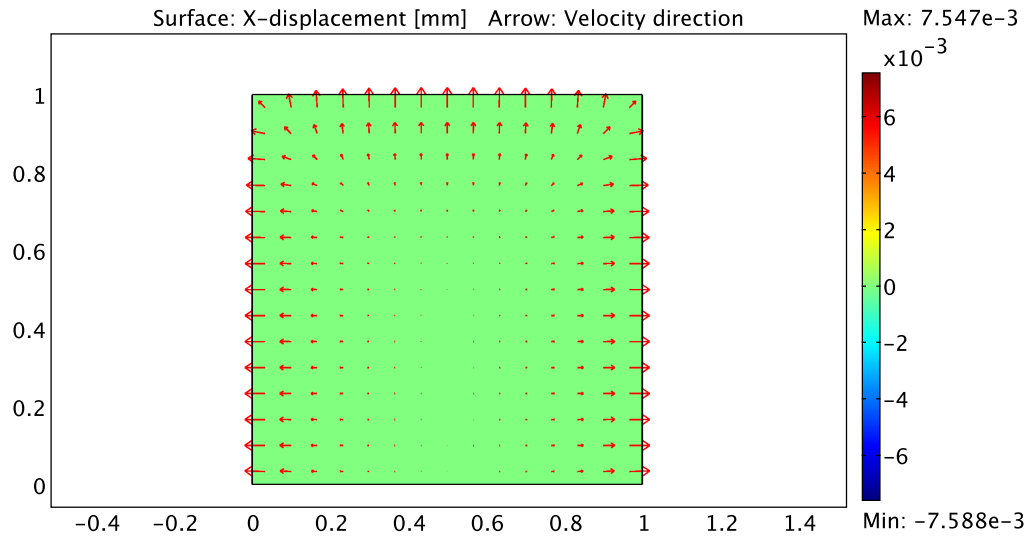
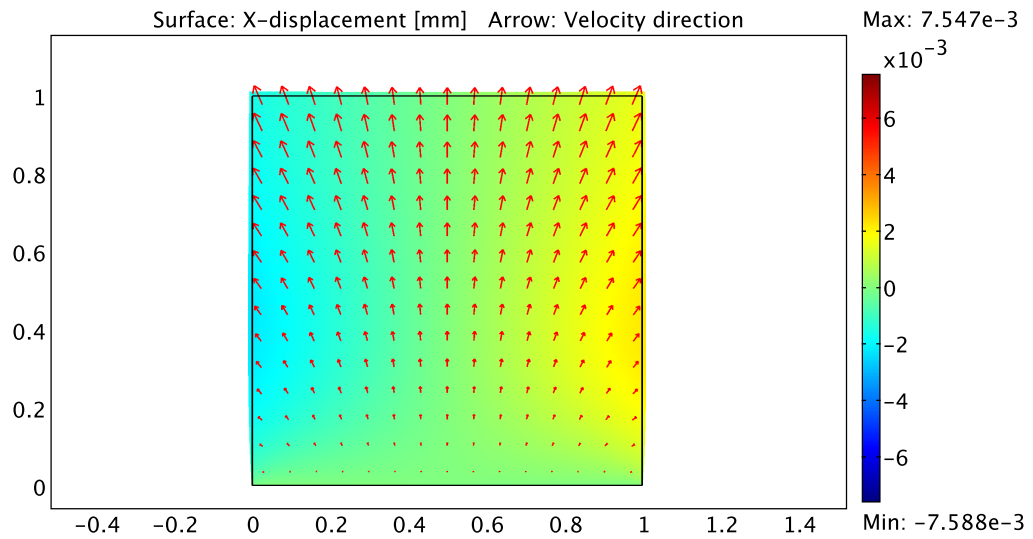
The above boundary condition—relating the stresses in the solid and fluid phases at the free surfaces of the tissue—is a statement that supplements the condition that there is the no relative velocity between the phases along these surfaces. Providing just the velocity condition is insufficient, as the set of solid displacement fields which can satisfy the no relative velocity condition is infinite.

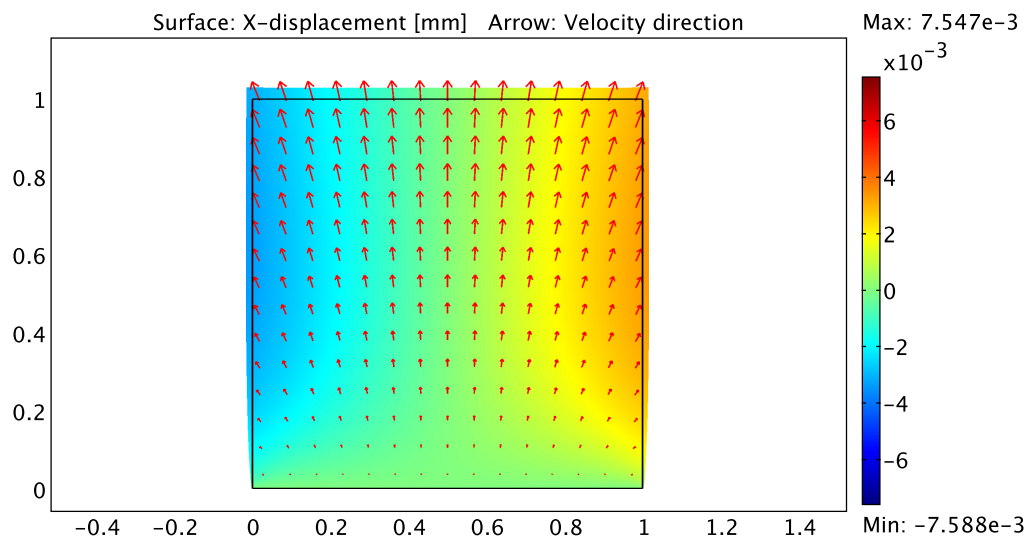
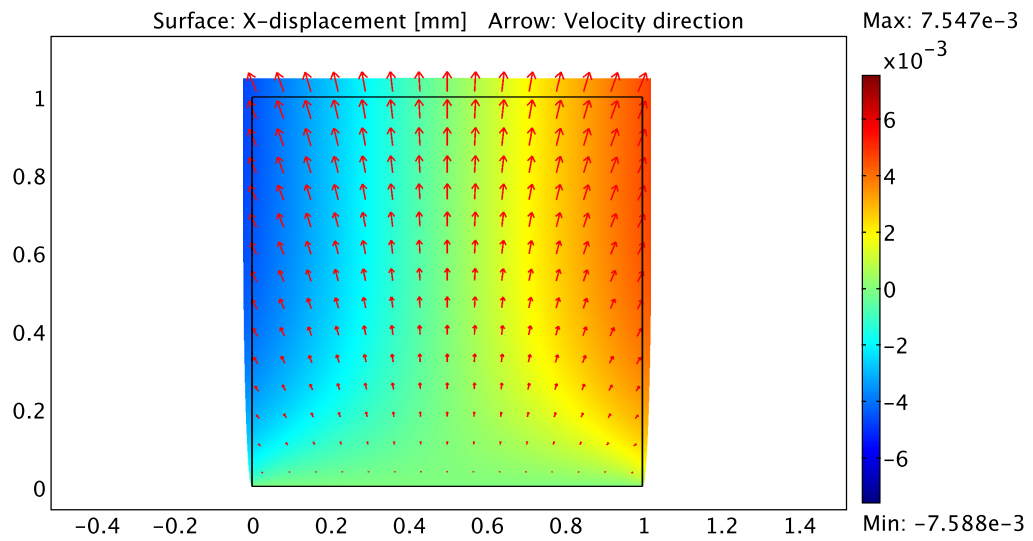
While the use of this stress-equilibration condition is common in the ALE literature for interactions between a fluid and a rigid body (see, for e.g., Nomura and Hughes (1992) and Sarrate et al. (2001)), I am not aware of its use in the context of biomechanics. The use of biphasic models in biomechanics literature tends to focus on cases where the mechanics of the problem is driven by displacement (or stress) boundary conditions imposed on the solid phase of the tissue (such as Spilker and Suh (1990) and DiSilvestro et al. (2001)). Unlike the current example, where the mechanics of the problem is driven by an inflow of fluid, these cases do not require

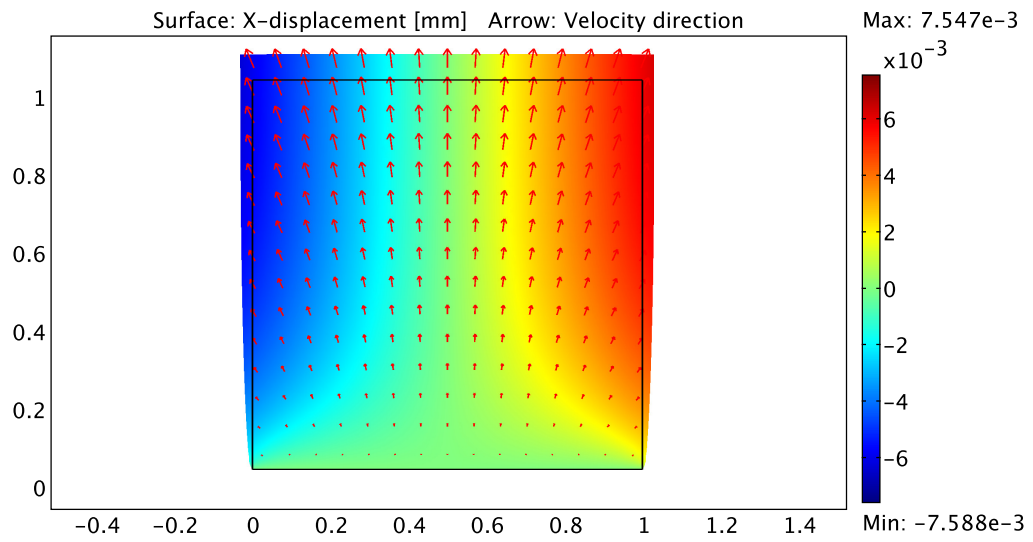
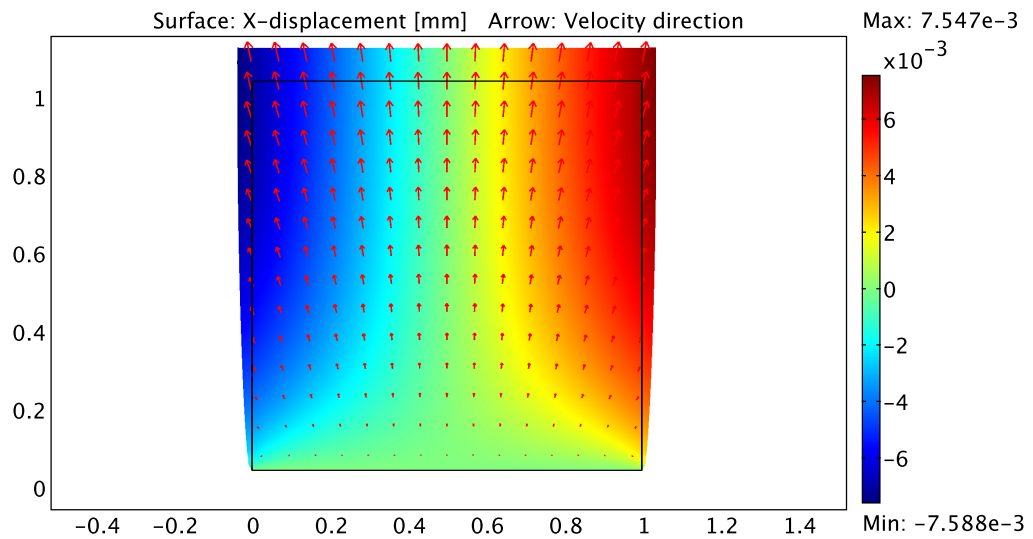
³In contrast to the swelling example discussed in Section 3.3.2, which used the notion of the growth portion of the deformation gradient of the fluid, \mathbf{F}^{g^f} , to cause kinematic swelling of the domain with an increase in fluid concentration, in this example, it is primarily this interaction between the solid and fluid stresses on the boundary that causes the domain to swell.

additional boundary conditions such as the one above.

Figures 5.2–5.7 show snapshots of the swelling domain during the course of the test. The colour contours provide the horizontal displacement field of the solid (in mm) and the arrows provide the direction of the solid velocity field. The pressure gradient induced by the increasing fluid pressure boundary condition on the bottom edge causes an inflow of fluid. The inability of the fluid to flow out of other boundaries manifests itself as an outward boundary traction on the solid, causing the domain to swell as seen in the figures. Because the computation was run with dynamics, there is initially a small oscillation in the fluid and solid velocity fields due to wave propagation in the fluid (not apparent in the plots) which fade in the first 0.4 s.

Figure 5.2: The inflating balloon at time $t = 0$ s.Figure 5.3: The inflating balloon at time $t = 0.6$ s.

Figure 5.4: The inflating balloon at time $t = 1.2$ s.Figure 5.5: The inflating balloon at time $t = 1.8$ s.

Figure 5.6: The inflating balloon at time $t = 2.4$ s.Figure 5.7: The inflating balloon at time $t = 3.0$ s.

5.2.2 The tissue under constriction

In the previous numerical experiment, we studied the deformation of the tissue under an influx of fluid. In this example, we turn our attention to fluid flow fields induced by the deformation of the solid phase and frictional interactions between the phases. The initial condition for this problem is identical to the previous case, i.e., the tissue is at rest initially and the initial concentrations of the solid collagen and fluid phases at all points in the unit square domain ($1 \text{ mm} \times 1 \text{ mm}$) are 500 kg.m^{-3} . As before, the total duration of the test is 3 s.

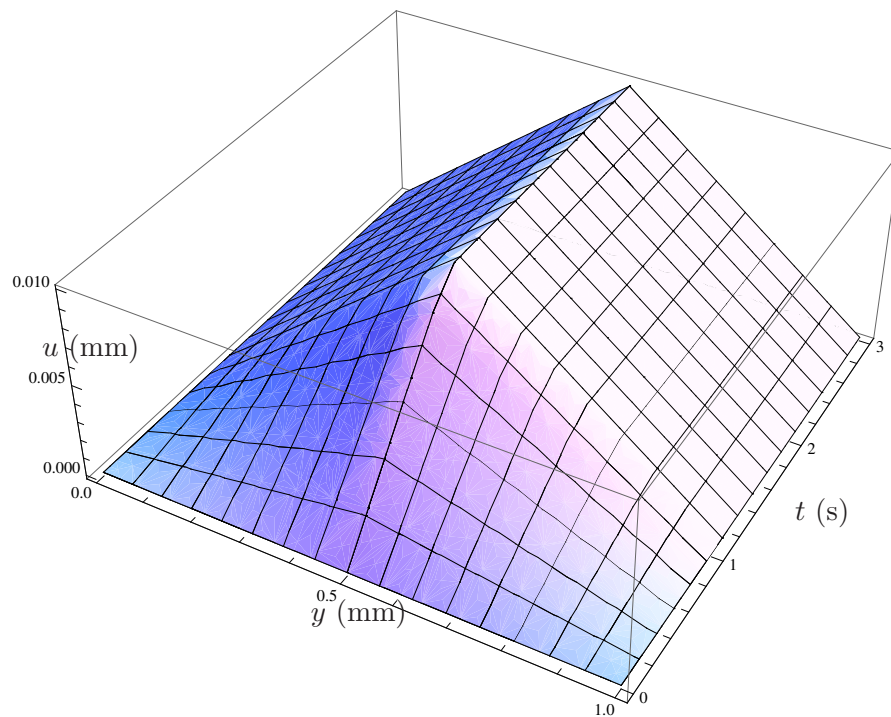


Figure 5.8: The displacement condition on the vertical edges of the tissue.

The boundary conditions for this problem correspond to immersing the tissue in a bath and applying a displacement load on the vertical edges so as to constrict the tissue in order to observe the resulting fluid flow. In particular, the fluid is subjected to a pressure boundary condition on all four edges; where the pressure of the fluid is equated to that of the bath, 0 MPa. For the solid, the bottom edge is held fixed and

the top edge is traction free. The left edge is subjected to the temporally-varying constrictive horizontal displacement (in mm) visualised in Figure 5.8. The figure shows the horizontal displacement being increased linearly in time for the first 1 s and then held fixed for the remainder of the test. The right edge is subjected to the negative of this load. In this example, the magnitude of the frictional coefficient tensor, $\mathbf{D}^{\text{fc}} = \mathbf{1} \text{ MPa}\cdot\text{s}\cdot\text{mm}^{-2}$, is significantly greater than in the previous case, and the effects of the frictional interaction between the phases are manifest in the results.

Figures 5.9–5.14 show snapshots of the constricted tissue during the course of the test. The colour contours provide the horizontal displacement field of the solid (in mm) which remains fixed after the first 1 s of the test. The arrows provide the direction and magnitude of the fluid velocity field. Their lengths scale linearly with the magnitude of the fluid velocity field and the longest arrow corresponds to a fluid velocity magnitude of $7.03\text{e-}3 \text{ mm}\cdot\text{s}^{-1}$. This fluid flow is mainly driven by a combination of frictional interaction with the solid phase and the saturation condition. The plots are asymmetrical in the vertical direction because the bottom edge is held fixed. Observe that the fluid velocity grows with increasing constriction of the solid for the first 1 s and gradually decays after the solid phase is held fixed (this is clearly seen in seen in Figure 5.15). There is also a nominal relaxation of the top edge after the constriction phase, as observed in the example in Section 3.3.1.

As in the previous example, effects from the dynamics were observed in this case as well, and an equivalent quasistatic calculation was performed for comparison. When the vertical fluid velocity is tracked at the centre of the top edge for the duration of the test in both these cases, it is observed that the dynamic case decays gradually and has oscillations (Figure 5.15) while the quasistatic case reaches a higher magnitude, and decays nearly instantaneously without manifesting oscillations (Figure 5.16).

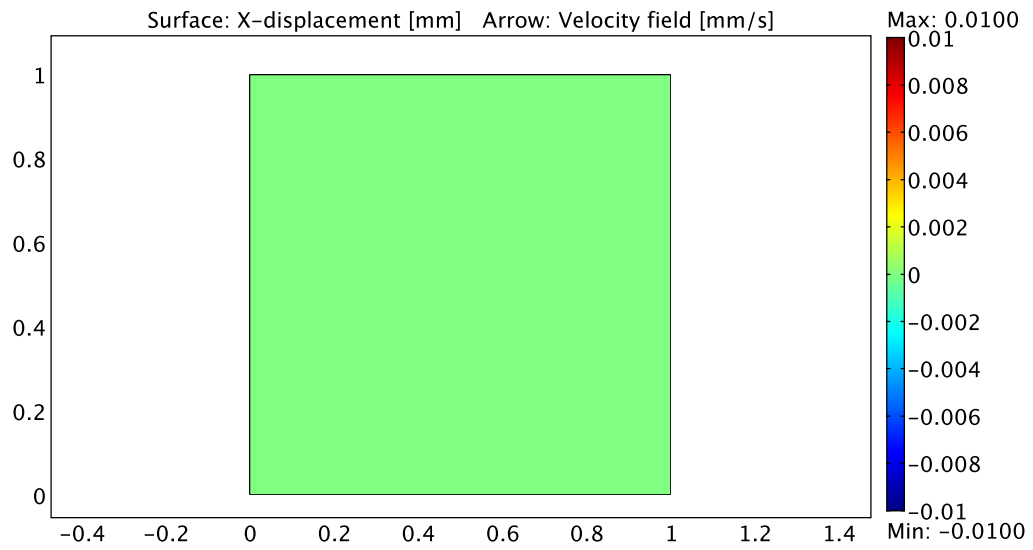


Figure 5.9: The constricted tissue at time $t = 0$ s.

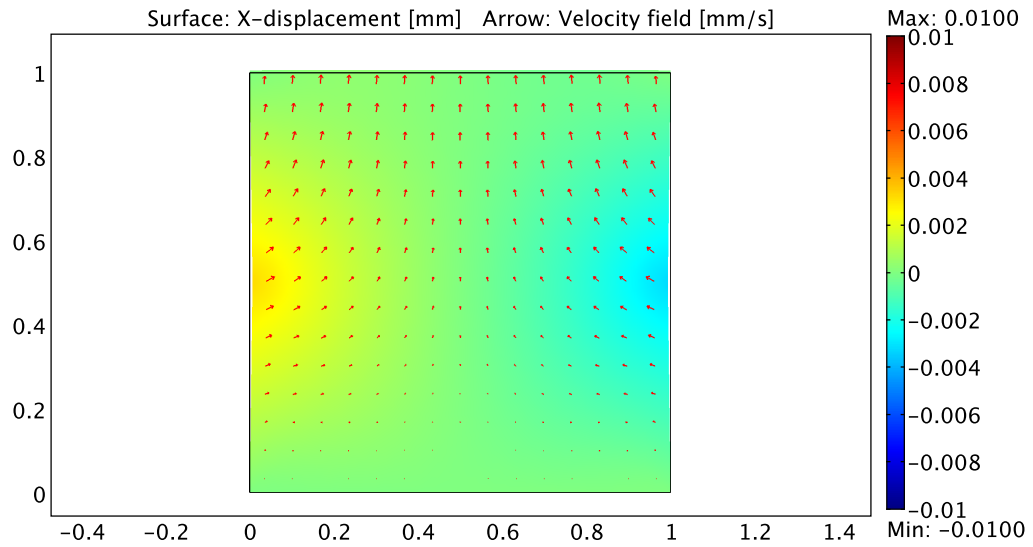


Figure 5.10: The constricted tissue at time $t = 0.32$ s.

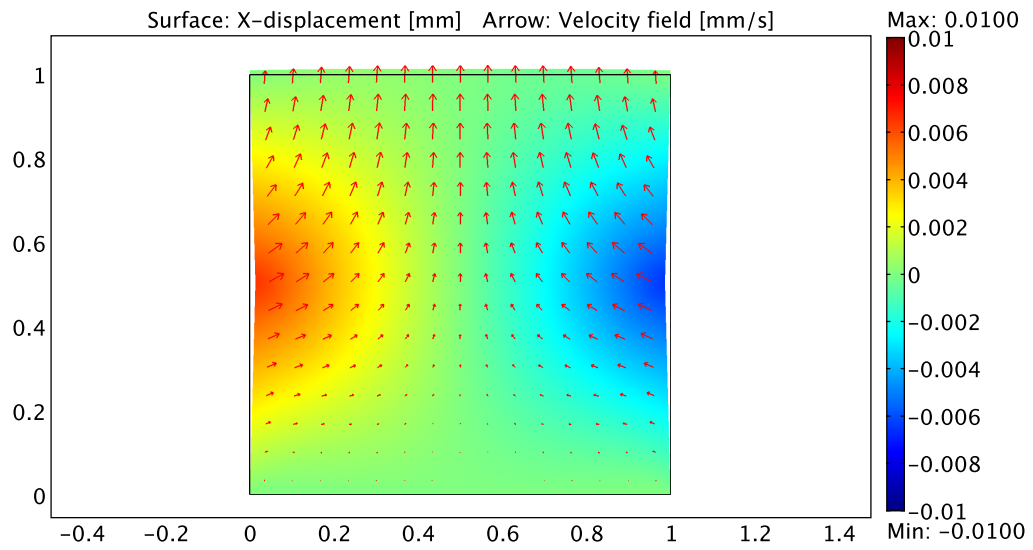


Figure 5.11: The constricted tissue at time $t = 0.66$ s.

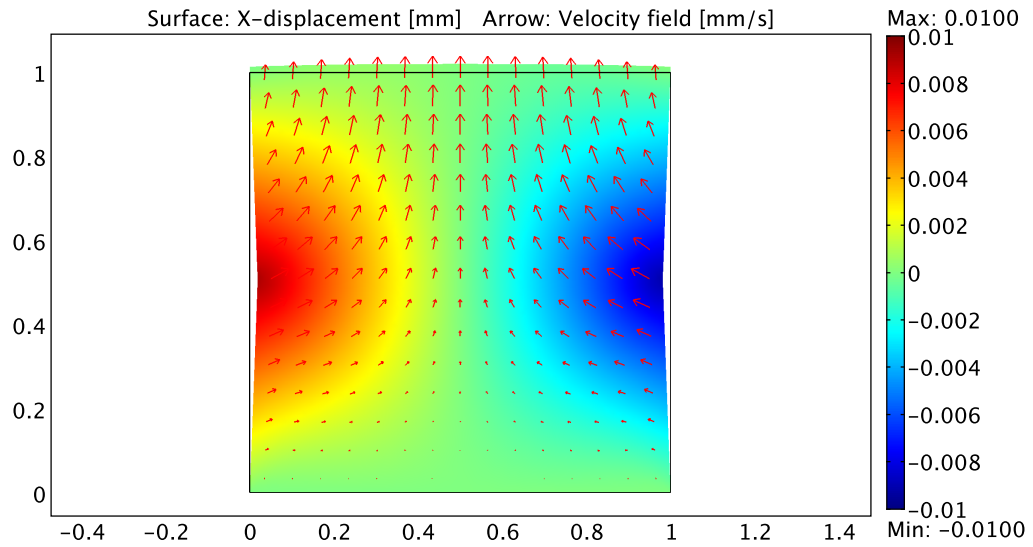


Figure 5.12: The constricted tissue at time $t = 1.0$ s.

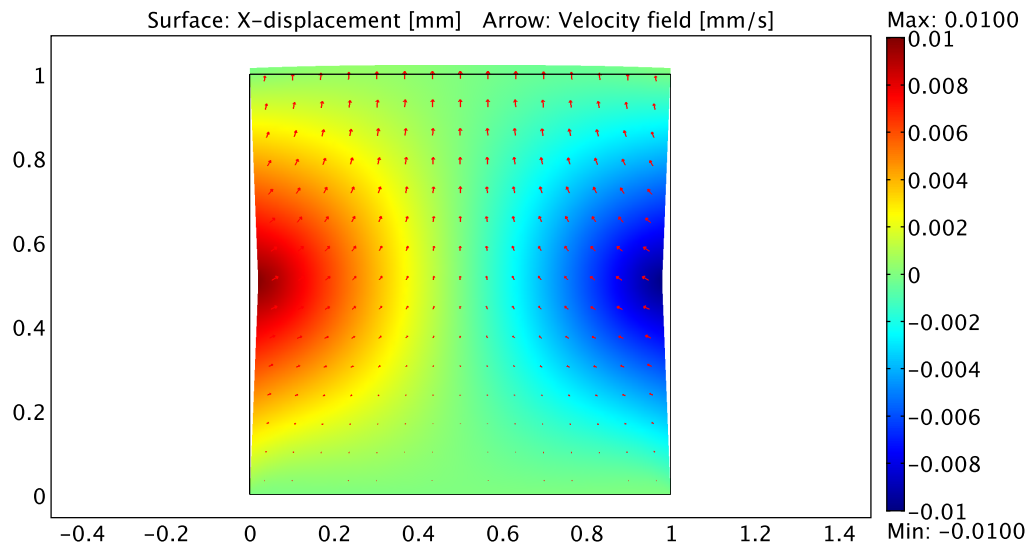


Figure 5.13: The constricted tissue at time $t = 2.0$ s.

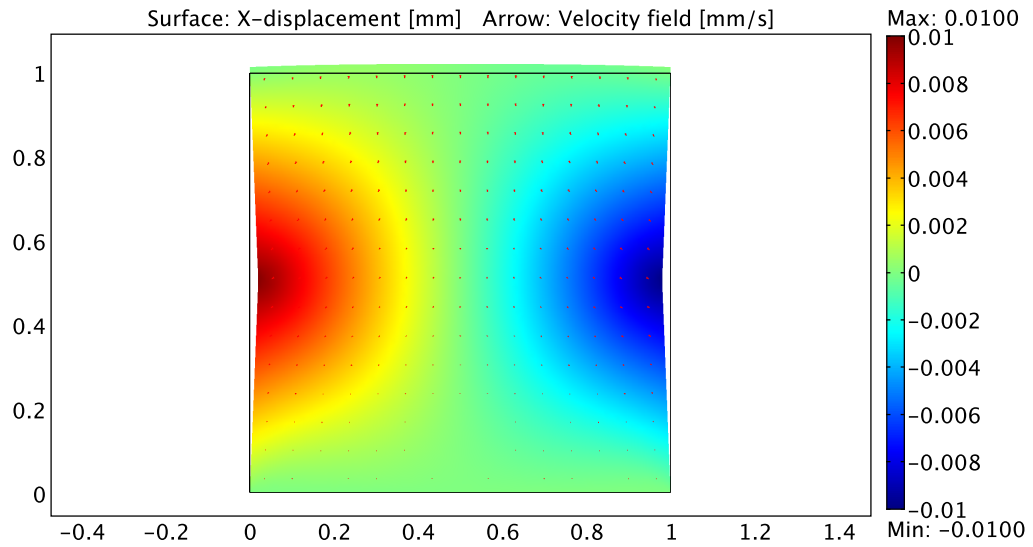


Figure 5.14: The constricted tissue at time $t = 3.0$ s.

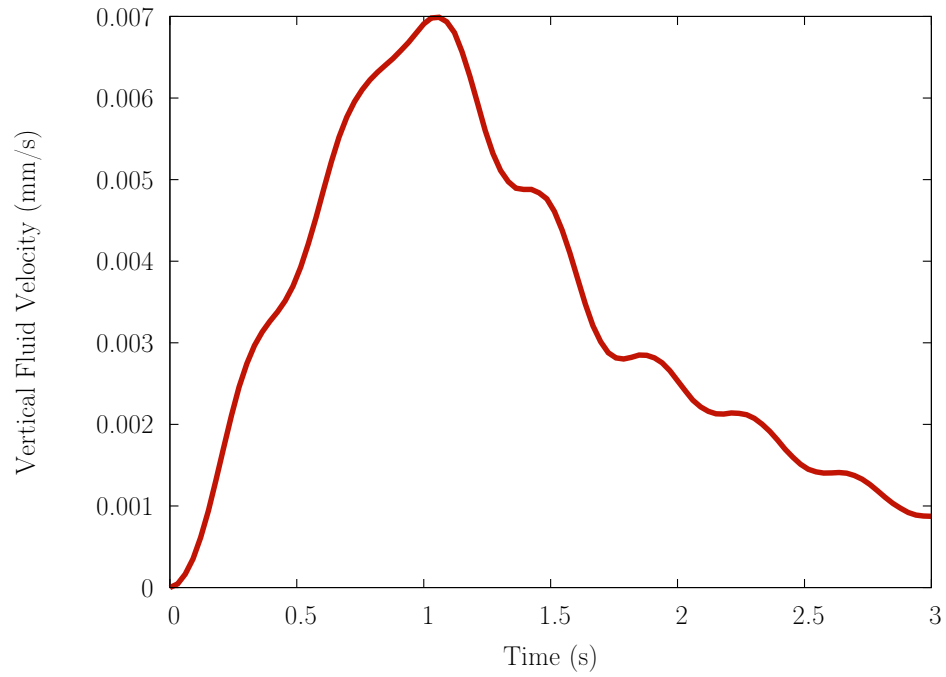


Figure 5.15: Dynamic evolution of the vertical fluid velocity.

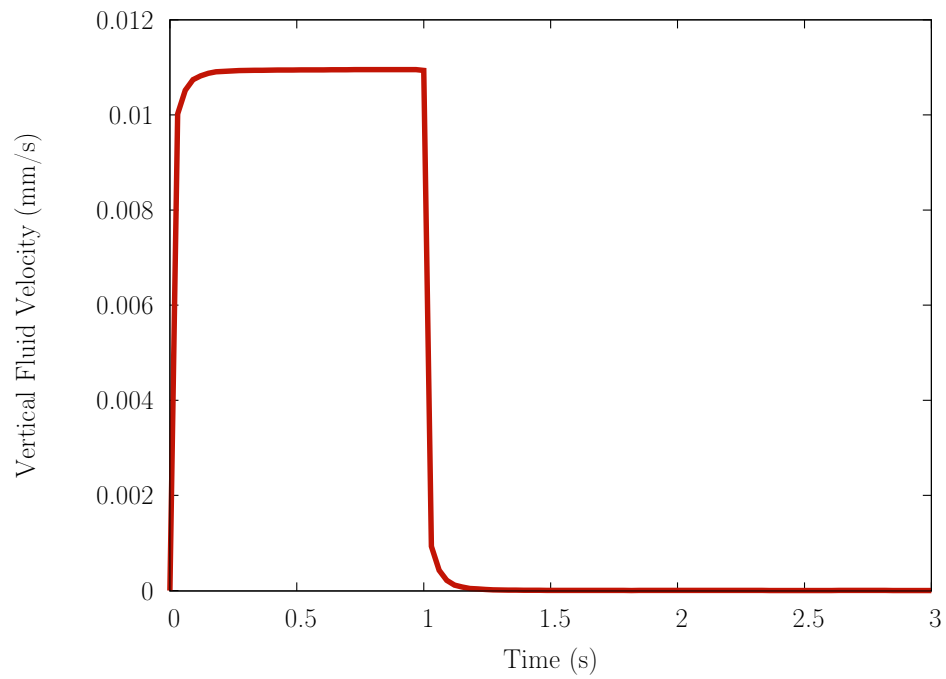


Figure 5.16: Quasistatic evolution of the vertical fluid velocity.

5.3 Examples exploring the biphasic nature of porous soft tissues

The introductory examples presented in the preceding section illustrated basic aspects of the coupled physics exhibited by non-reacting two-phase mixtures. The computational formulation thus provides a means for determining the evolution of fluid flow fields under varying physically-relevant boundary conditions, and allows us to study their effects on the mechanics of tissues. With this established, we now turn our attention to a more realistic application—studying aspects of the time- and rate-dependent behaviour of ligaments.

In the following examples, the material parameters and model geometry are tailored to more closely represent experimental studies on the mechanics of engineered ligaments (Ma, 2007). The examples focus on the viscoelastic behaviour of these tissues arising primarily from frictional interaction between two purely elastic phases: an ideal fluid perfusing a porous, hyperelastic solid (as in the preceding section). In particular cases, this *poroelastic* response is compared to analogous results obtained using a single-phase linear viscoelastic solid model (discussed in Section 4.2.4).

Motivated by the experimental work, the model geometry is initially 12 mm in length and 1.128 mm in width, and has a uniform thickness of 1.128 mm. The initial concentration of the solid collagen is $300 \text{ kg}\cdot\text{m}^{-3}$ and the initial fluid concentration is $700 \text{ kg}\cdot\text{m}^{-3}$ at all points in the domain. The intrinsic densities of the solid collagen and fluid phases are both $1000 \text{ kg}\cdot\text{m}^{-3}$, as before. The hyperelastic model for the solid phase uses the Mooney-Rivlin strain energy function (5.2) with 9 terms, and the values of the corresponding parameters used in the analysis are reported in Table 5.1.

The initial solid and fluid concentrations, and the Mooney-Rivlin parameters chosen, approximate the collagen content and the tensile response of the explanted

Parameter	Value (GPa)
C_{10}	0
C_{01}	0
C_{20}	0.54434
C_{11}	0
C_{02}	0.54714
C_{30}	1.83688
C_{21}	1.19985
C_{12}	10.6863
C_{03}	38.3875

Table 5.1: Material parameters used in the analysis.

ligament⁴ whose mechanical response under repeated cyclic loading is shown in Figure 5.17. In particular, the hyperelastic material parameters are chosen to approximate the stress-strain response corresponding to the first load excursion (denoted by the blue points).

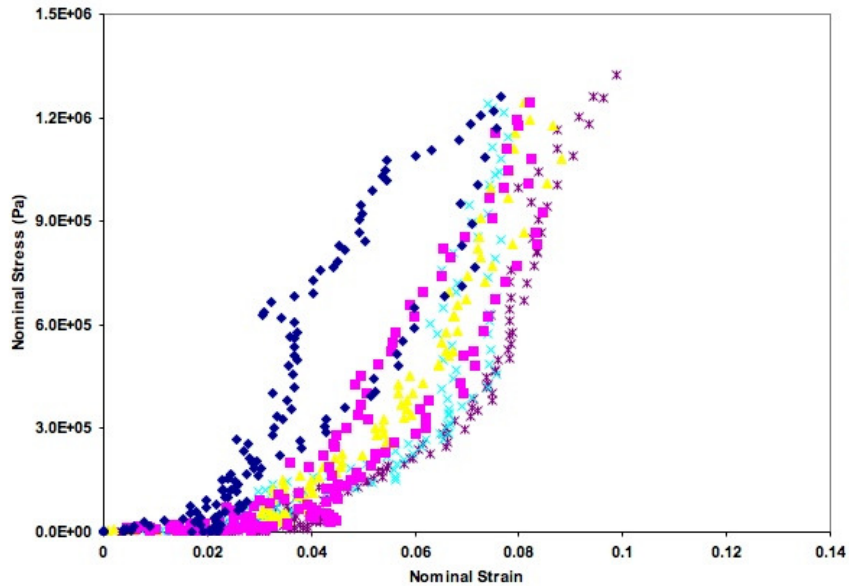


Figure 5.17: Mechanical response of an explanted ligament (Ma, 2007).

The basal magnitude of the frictional coefficient tensor used in following calculations is fit to the experimental work of Swartz et al. (1999) on fluid transport

⁴This tissue is from a batch of engineered ligaments explanted after implantation for one month as medial collateral ligament replacements in live rats (Ma, 2007).

through mouse tails. This was achieved by subjecting the computational model to a fluid pressure gradient identical to that in their experiment, and the frictional coefficient tensor magnitude was modified until the until the steady-state flow velocity in the computations matched those reported in the experiment. The resulting frictional coefficient tensor is: $\mathbf{D}^{\text{fc}} = 1.037 \mathbf{1} \text{ MPa}\cdot\text{s}\cdot\text{mm}^{-2}$. In what follows, this isotropic tensor will be characterised by its scalar magnitude, D .

5.3.1 Stress relaxation

In these tests, the boundary conditions correspond to gripping the tissue at its longitudinal ends, loading it at a constant strain rate to a specific strain, and holding the tissue fixed at that strain for the remainder of the test. For the solid phase, this translates to holding one of the longitudinal edges fixed while subjecting the other to the suitable displacement load. The lateral edges of the solid remain traction free. For the fluid, there is no flow relative to the solid at the longitudinal edges, i.e., $\mathbf{v}^{\text{f}} = \mathbf{v}^{\text{c}}$. Since we are simulating the tissue being held by grips at the longitudinal edges, this boundary condition ensures that there is no outflow or inflow along those edges. The lateral edges expose the fluid to the bath, and therefore the fluid pressure is equated to that of the bath, 0 MPa, along those edges.

Figure 5.18 shows the stress relaxation in a quasistatic calculation⁵ where the tissue is loaded at a strain rate of $\dot{\epsilon} = 0.01 \text{ Hz}$ to a maximum strain of 0.085 in 8.5 s, and then held fixed at that strain for the remainder of the test. A large portion of the tensile response is furnished by the hyperelastic solid collagen, and the decaying peak in the stress is due to the decaying relative velocity between the two phases.

⁵Since the displacement condition applied to the solid is not smooth in time, the corresponding velocity boundary condition on the fluid is discontinuous in time. Consequently, the poroelastic calculations presented in this section assume that the process is quasistatic; only requiring that the velocity fields be integrable in time.

Notice that this peak in stress decays rapidly, corresponding to the rapidly decaying velocity field in the quasistatic result shown in Figure 5.16.

In order to study the effects of the load rate on the mechanical response, the next test doubles the strain rate to $\dot{\epsilon} = 0.02$ Hz. The tissue is subjected to the same maximum strain of 0.085, now in 4.25 s, and is held fixed for the remainder of the test. The stress relaxation resulting from this test is shown in Figure 5.19. The initial peak stress is now increased; an observation which is in agreement with classical results in viscoelasticity theory. This is because the increased strain rate results in an increased relative velocity between the phases initially, which correspondingly increases the frictional interaction between the phases.

Finally, the biphasic poroelastic response is compared to the response of a model comprising of only one phase: linear viscoelastic solid collagen. In this computation, the elastic portion of the response of the solid collagen has the same form (5.2) and material properties (Table 5.1) as the poroelastic case, and has a characteristic relaxation time, $\tau = 0.3$ s, and strain-energy factor, $\beta = 0.5$.⁶ This test is carried out at a strain rate of $\dot{\epsilon} = 0.02$ Hz for 4.25 s, at which point the tissue is held fixed. Figure 5.20 shows the corresponding stress relaxation, and there are two noticeable differences in the results from the poroelastic calculation performed at the same strain rate (Figure 5.19). Firstly, stemming from the initially-high relative velocity between the phases, the poroelastic curve starts with a higher stiffness than the viscoelastic case. And secondly, the quasistatic nature of the poroelastic calculation results in a sharper, more rapidly-decaying peak in stress.

⁶Refer Section 4.2.4 for details.

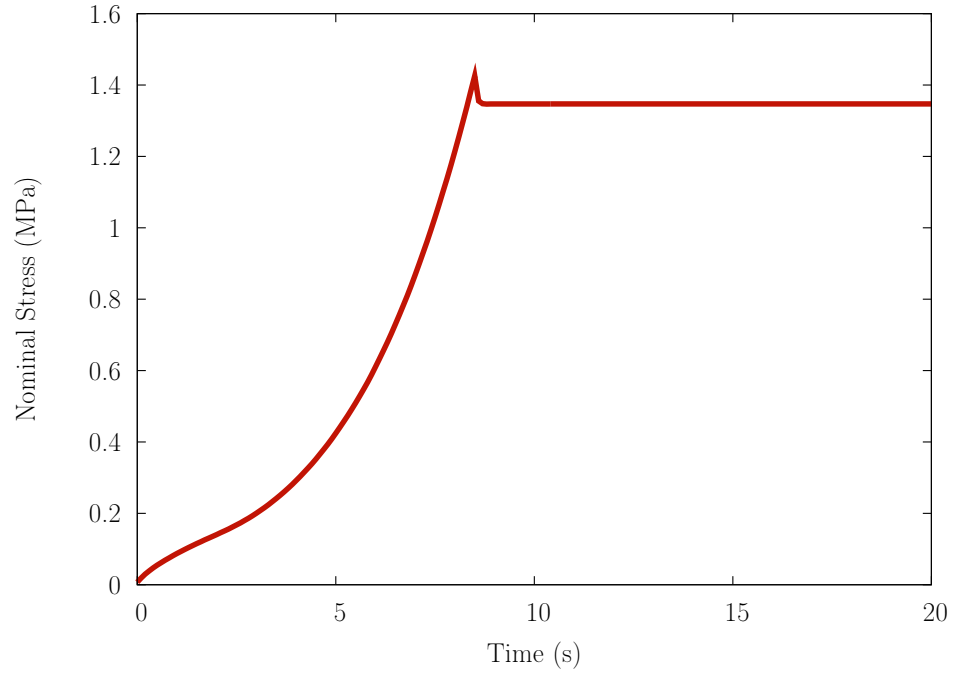


Figure 5.18: Quasistatic poroelastic model, $\dot{\epsilon} = 0.01$ Hz, $D = 1.037$ MPa.s.mm⁻².

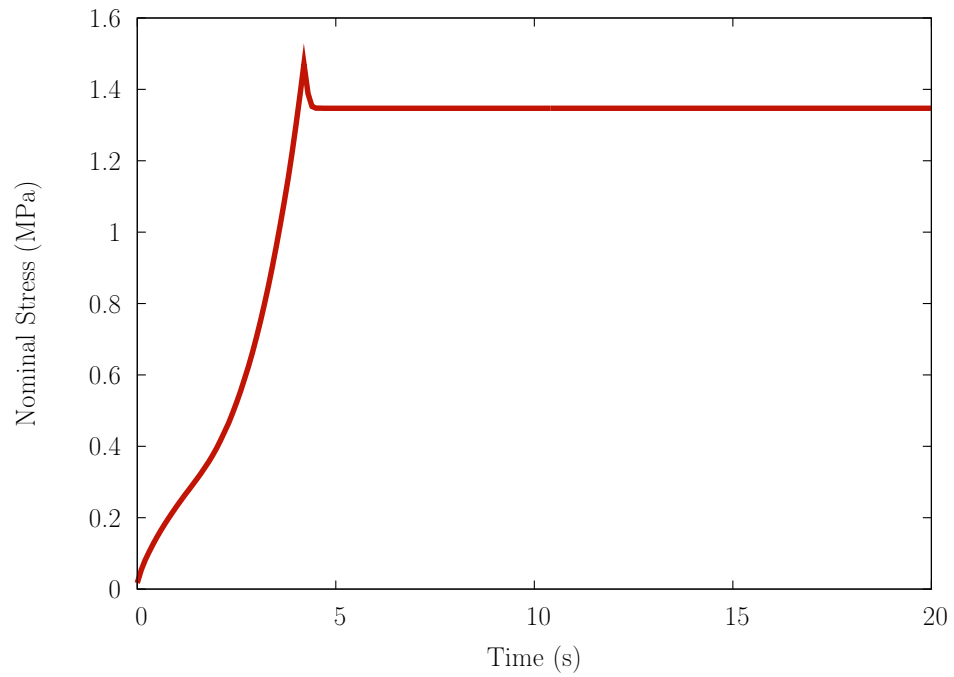


Figure 5.19: Quasistatic poroelastic model, $\dot{\epsilon} = 0.02$ Hz, $D = 1.037$ MPa.s.mm⁻².

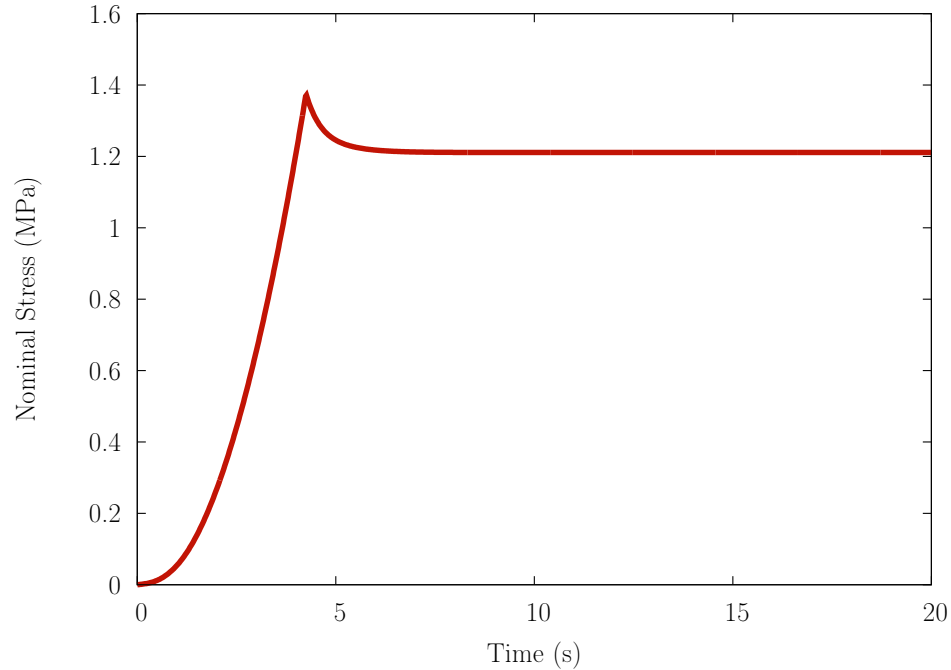


Figure 5.20: Dynamic viscoelastic model, $\dot{\epsilon} = 0.02$ Hz, $\tau = 0.3$ s.

5.3.2 Hysteresis in the cyclic stress-strain response

The examples in this section study the hysteresis in the stress-strain response when the model is subjected to a complete load-unload cycle. As before, for the solid phase, the boundary conditions specify that one of the longitudinal edges of the tissue is held fixed, while subjecting the other to the suitable displacement condition. The lateral edges of the solid remain traction free. For the fluid, there is no flow relative to the solid at the longitudinal edges, i.e., $\mathbf{v}^f = \mathbf{v}^c$. The lateral edges expose the fluid to the bath, and therefore the fluid pressure is equated to that of the bath, 0 MPa, along those edges.

In all these tests, the model was first loaded to a maximum strain of 0.085 (to match the experimental data presented in Figure 5.17) and subsequently unloaded to no strain. Since the numerical experiments so far have suggested conspicuous differences between the quasistatic and dynamic solutions, both these cases have

been explored in this section. When the fluid flow fields are observed during the course of these load-unload tests, it is found that they constantly lag behind the motion of the solid; and it is this relative velocity, and the corresponding frictional interaction between the phases, that leads to energy dissipation manifesting itself as the hysteresis loop.

For the quasistatic hysteresis curve presented in Figure 5.21, the model was loaded at a rate of $\dot{\epsilon} = 0.01$ Hz for 8.5 s to a total strain of 0.085, and then subsequently unloaded at the same rate back to 0 strain in another 8.5 s. This discontinuous (in time) velocity boundary condition for the fluid is acceptable for the quasistatic calculation. When compared to the hysteresis result arising from the dynamic calculation loaded and unloaded at the same *average* strain rate (Figure 5.22),⁷ it is clear once more that the quasistatic calculation lacks the characteristic oscillations arising from pressure wave propagation in the fluid observed in the dynamic calculation. It is also interesting to note that beyond a certain strain (~ 0.06), the solid is stiff enough to overcome the oscillatory effects arising from the fluid flow.

When this average strain rate is decreased to $\bar{\epsilon} = 0.001$ Hz, ($1/10^{\text{th}}$ the rate of the preceding calculation), the relative velocity between the phases correspondingly decreases, resulting in reduced dissipation and area of the hysteresis loop (see Figure 5.23). In other words, this slower process proceeds closer to thermodynamic equilibrium. In an analogous comparison, when the average strain rate is maintained at $\bar{\epsilon} = 0.01$ Hz, but the magnitude of the frictional coefficient tensor is increased by a factor of 10 to $D = 10.37$ MPa.s.mm⁻², it is observed that the dynamic effects of the

⁷Since the uniform strain rate load-unload displacement condition prescribed for the quasistatic calculation (termed the *triangular load*) is insufficiently smooth in time, the dynamic calculations are instead subjected to a load-unload displacement that takes the shape of a cosine curve. This displacement condition reaches the same maximum strain and unloads to no strain at the same times as the triangular load, but maintains the necessary smoothness in the velocity fields to allow for the dynamic calculations.

fluid flow are much more prominent (as observed in Figure 5.24). This is because the comparable strain rates ensure similar relative velocities between the phases (in the calculations corresponding to Figures 5.22 and 5.24), but the frictional interaction between the fluid and solid phases has now increased by an order of magnitude.

The results presented in this section demonstrate aspects of the experimentally observed mechanical response of ligaments seen in Figure 5.17. Finally, the biphasic poroelastic results presented thus far are compared to the response of the purely linear viscoelastic model introduced in the preceding section. This model was loaded at a strain rate of $\dot{\epsilon} = 0.01$ Hz for 8.5 s to a total strain of 0.085, and then subsequently unloaded at the same rate back to 0 strain in another 8.5 s. The resulting stress-strain curve is shown in Figure 5.25. Upon comparing it with Figure 5.22, we find as we did before, that, stemming from the initial frictional interaction between the phases, the poroelastic case starts out stiffer, and the viscoelastic model fails to capture any of the dynamic effects arising from the fluid flow.

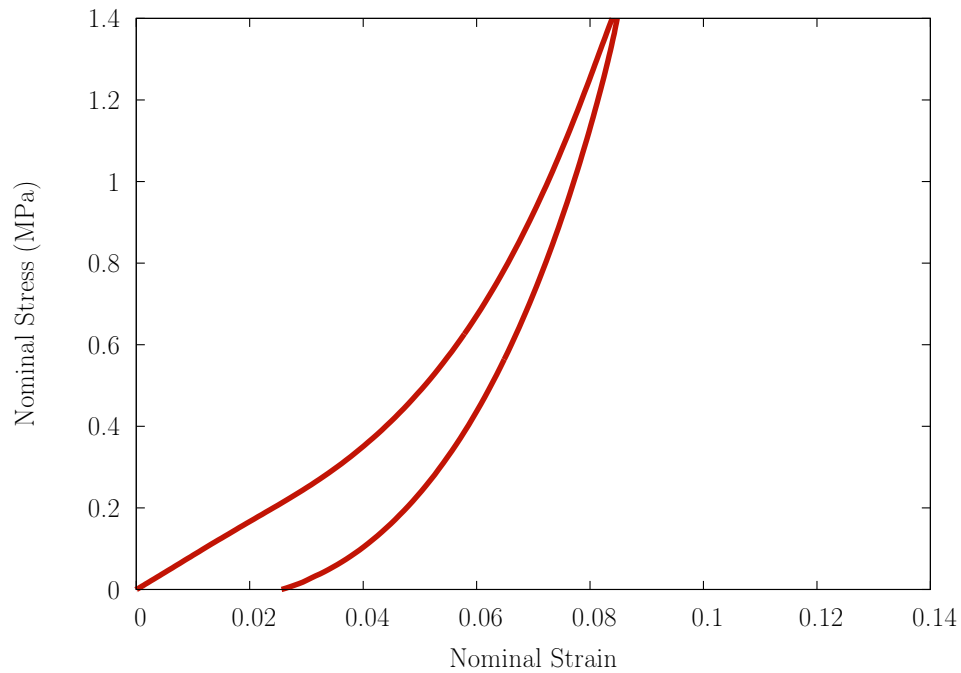


Figure 5.21: Quasistatic poroelastic model, $\dot{\epsilon} = 0.01$ Hz, $D = 1.037$ MPa.s.mm⁻².

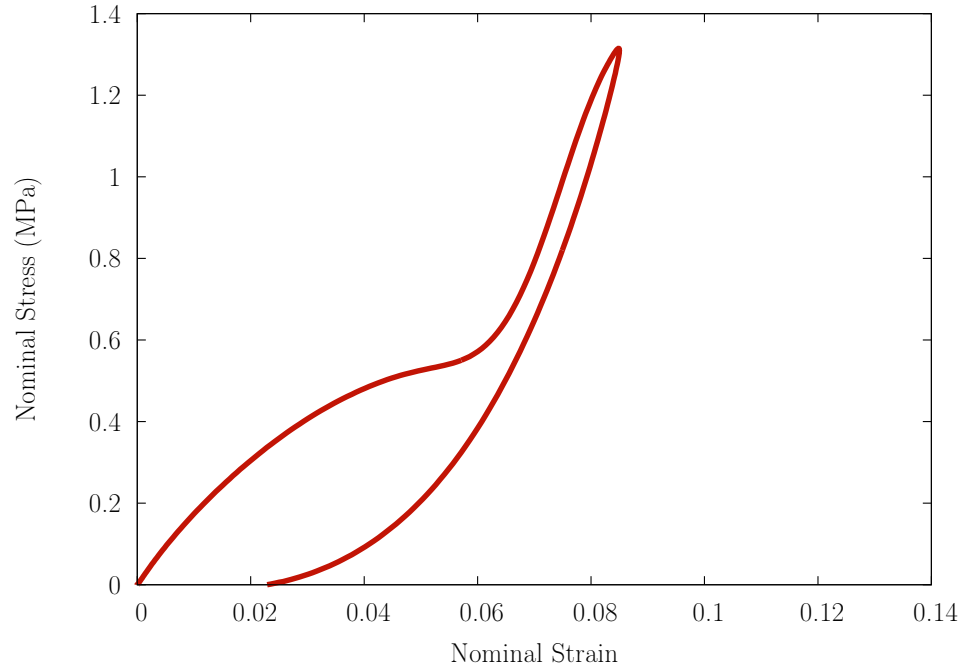


Figure 5.22: Dynamic poroelastic model, $\bar{\epsilon} = 0.01$ Hz, $D = 1.037$ MPa.s.mm⁻².

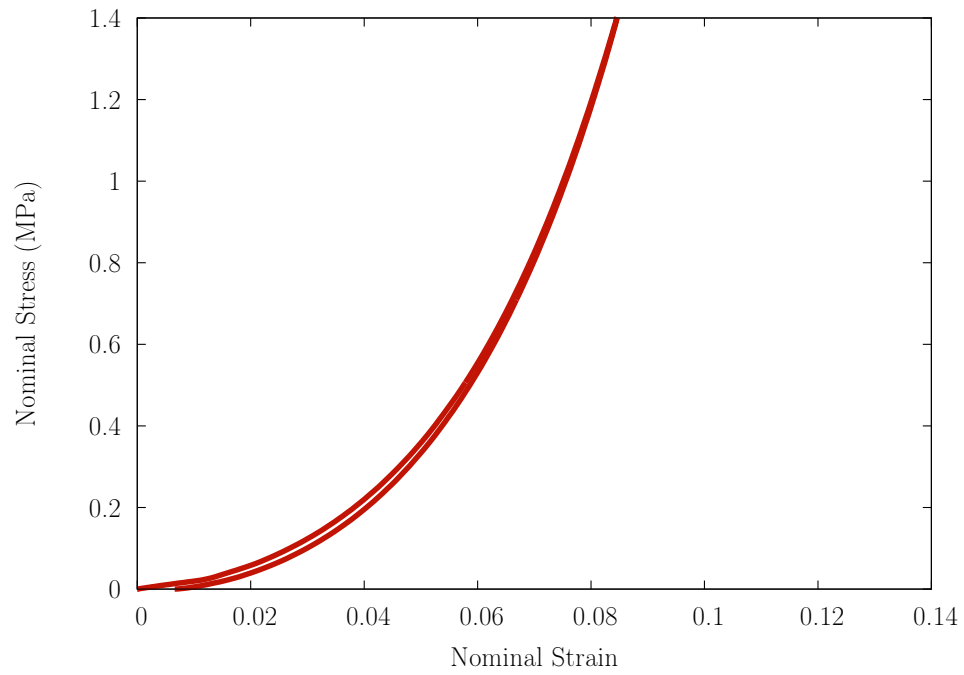


Figure 5.23: Dynamic poroelastic model, $\bar{\epsilon} = 0.001$ Hz, $D = 1.037$ MPa.s.mm⁻².

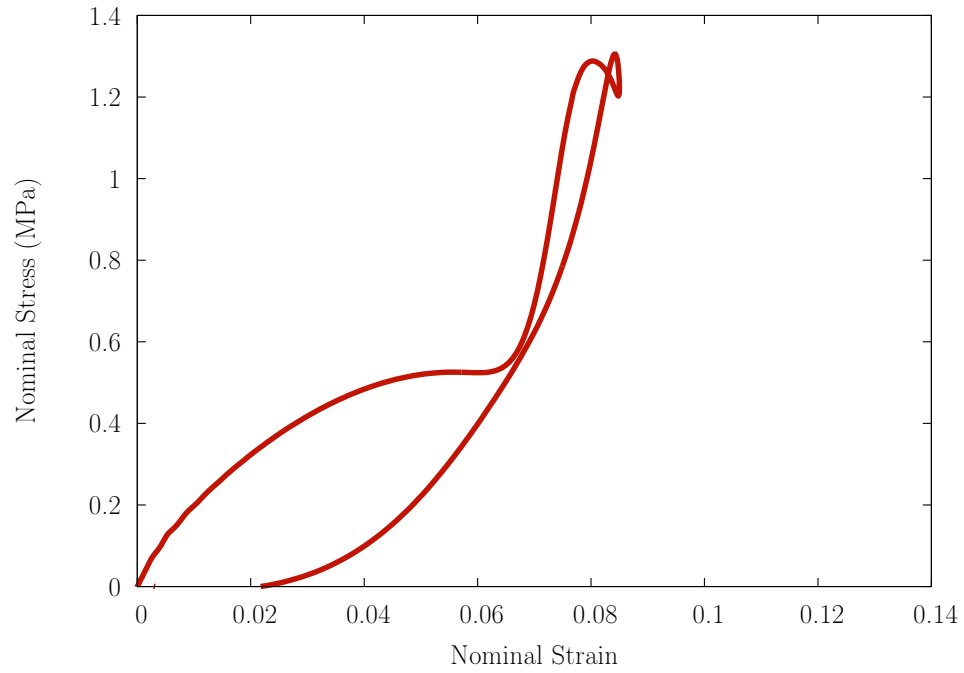


Figure 5.24: Dynamic poroelastic model, $\bar{\epsilon} = 0.01$ Hz, $D = 10.37$ MPa.s.mm⁻².

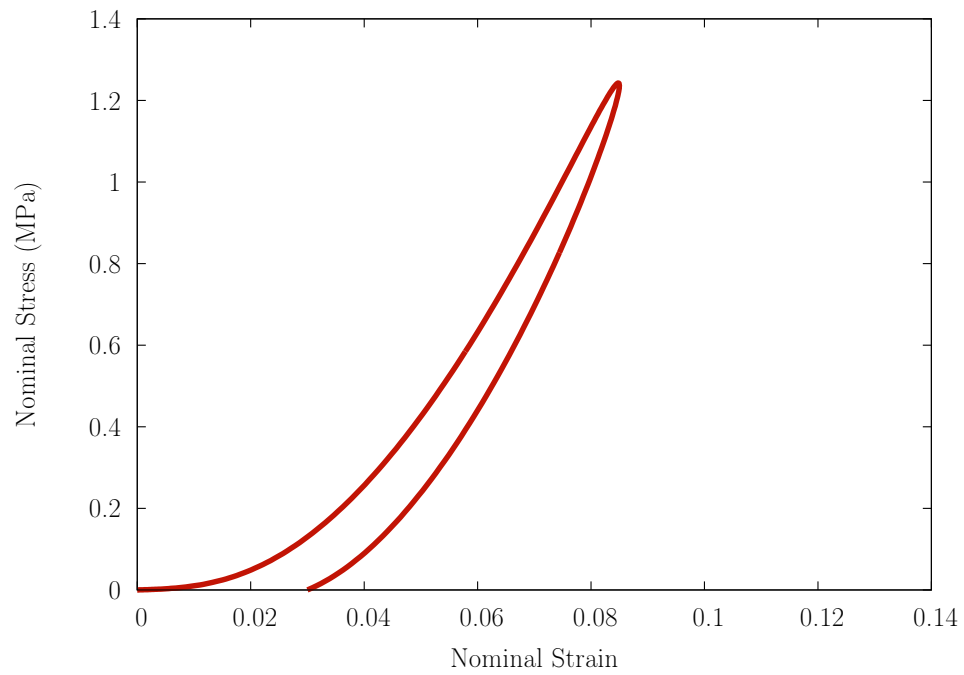


Figure 5.25: Dynamic viscoelastic model, $\dot{\epsilon} = 0.01$ Hz, $\tau = 0.3$ s.

5.4 Mechanics and the growing tumour

This final section presents a preliminary foray into tailoring the mathematical formulation developed in Chapter 4 to studying the mechanics of growing tumours. Unlike the computations presented in the preceding sections, which principally focused on the biphasic mechanics of soft tissues in the absence of biochemical interactions between the phases (tissue growth), in examples that follow, we will turn our attention to an idealisation of growing tumours, and examine the role of the mechanical environment on its growth.

Similar to the approach followed in Section 5.2, the computations presented below serve only to demonstrate aspects of the coupled physics underlying the problem, and the actual constitutive modelling choices made (and the corresponding numerical parameters used) are not intended for direct comparison with experiment. Incorporating more realistic modelling choices (such as the use of more sophisticated biochemistry involving additional species ([Jackson and Byrne, 2000](#))), and the ascertainment of corresponding parameters, is a direction for future work.

The computations presented in this section are motivated by and aim to replicate a fundamental experimental observation: Compressive solid stress along a given direction restricts the in vitro growth of tumours along that direction ([Helmlinger et al., 1997](#)). The foundational examples discussed in Sections 5.4.1–5.4.4 focus on different aspects of this confined tumour growth problem, and a combination of all these phenomena are manifested in the final computation presented in Section 5.4.5.

The computational model used in this section is primarily a solid comprised of an extra-cellular matrix (ECM) and tumour cells capable of moving with respect to this matrix.⁸ In order to simplify the scenario, it is assumed that the solute phases,

⁸We have already studied the effects of the extra-cellular fluid flow on the mechanics in some

such as the nutrients and enzymes, are present in sufficient amounts to drive the biochemistry that allows the cells to proliferate and produce more ECM. The model geometry, as visualised in Figure 5.26, is semicircular and has a radius of 10 mm initially.

5.4.1 Kinematic swelling concomitant with growth

In this initial calculation, we focus on the kinematic swelling associated with an increase in the mass of the solid tumour. The isotropic swelling tensor introduced in Section 2.2 has been modified to,

$$(5.3) \quad \mathbf{F}^{\text{g}^c} = \begin{pmatrix} \left(\frac{\rho_0^c}{\rho_{0\text{ini}}^c}\right)^{1/2} & 0 & 0 \\ 0 & \left(\frac{\rho_0^c}{\rho_{0\text{ini}}^c}\right)^{1/2} & 0 \\ 0 & 0 & 1 \end{pmatrix},$$

since we are working in two dimensions under a plane strain setting.

This example solves the mass (2.2) and momentum balance (2.7) equations for the solid (comprised at this point of both cells and the matrix) in the reference configuration. The boundary conditions for the momentum balance equations only prevent rigid body motion of the domain, and do not constrain its deformation in any way. The mass balance equation is solved with a uniform source term $\Pi^c = 0.001 \text{ kg}\cdot\text{m}^{-3}/\text{day}$. The initial solid concentration is $\rho_{0\text{ini}}^c = 1 \text{ kg}\cdot\text{m}^{-3}$.

As a result of this uniform mass source, and the increasing solid concentration, the domain begins to swell. Figures 5.26 and 5.27 show the tumour initially, and after 100 days. The colour contours provide the radial displacement of the solid in mm, and the arrows provide the direction of its velocity. Since there are no constraints on

detail in the preceding sections. Since we are currently focusing on other phenomena, we have chosen to ignore the fluid here.

the deformation, this swelling is isotropic. Figure 5.28, shows the area of the domain increasing linearly in time over the duration of the computation. Note that the ratio of the final to initial areas $172.788 \text{ mm}^2/157.08 \text{ mm}^2$ is exactly the same as the ratio of the final to initial concentrations $1.1 \text{ kg}\cdot\text{m}^{-3}/1 \text{ kg}\cdot\text{m}^{-3}$, as one would expect.

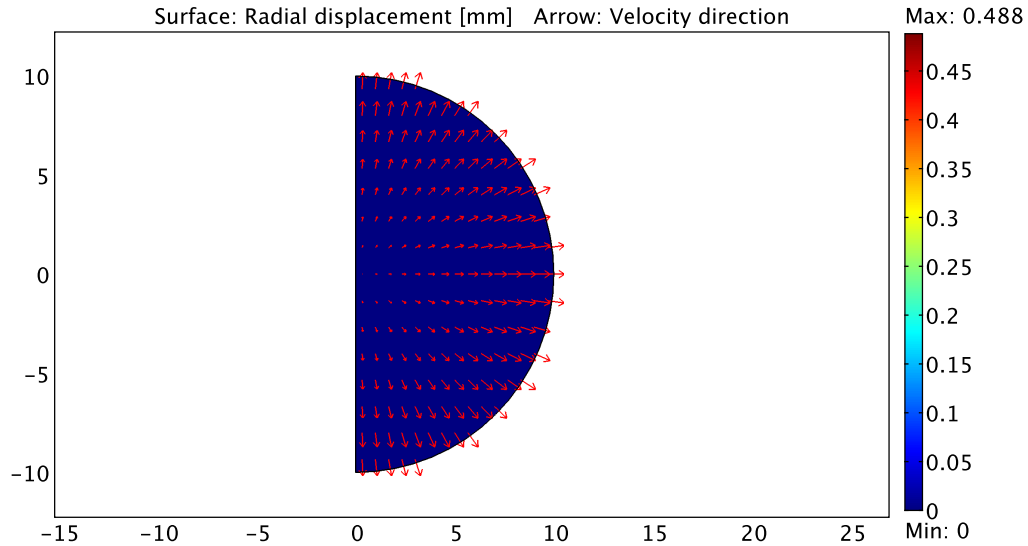


Figure 5.26: A semicircular tumour at time $t = 0$ days.

5.4.2 A constraining wall and soft contact mechanics

We are interested in subjecting this solid tumour model to a compressive stress, and the way we impose this condition is to introduce a rigid wall 10.5 mm to the right of the vertical edge of the domain, and allowing the swelling tumour to impinge upon it. Recall that the initial radius of the semicircular domain is 10 mm, thus giving it 0.5 mm to grow before it contacts the wall.

For this calculation, the solid is assumed to be hyperelastic with the Mooney-Rivlin strain energy function (5.2) with constants $C_{10} = 0.37$ and $C_{10} = 0.11$ MPa. As in the previous calculation, the balance of mass and momentum for this growing

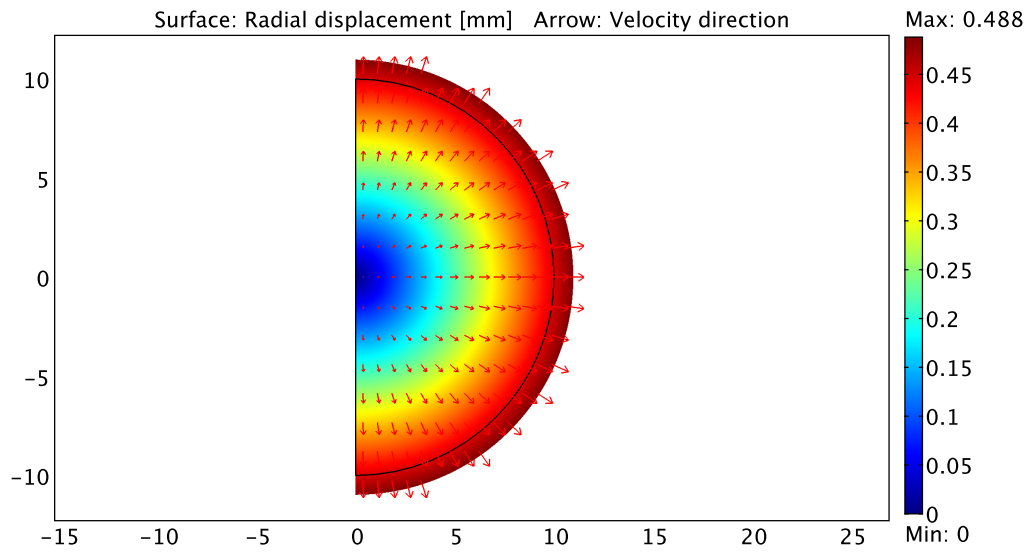


Figure 5.27: A semicircular tumour at time $t = 100$ days.

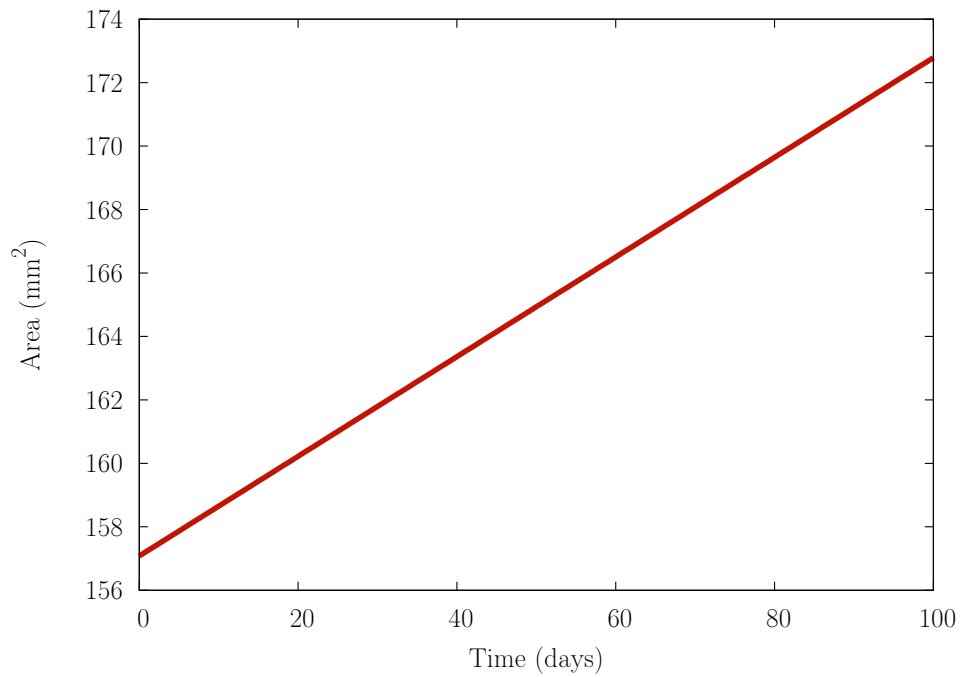


Figure 5.28: The area of the tumour evolving over 100 days.

solid are solved in the reference configuration. Since we are solving the momentum balance with dynamics, we cannot introduce the rigid wall instantaneously, as this results in time-discontinuous solid velocity fields. We instead use the following “soft” contact mechanics model,

$$(5.4) \quad q = -A \exp(-Bg),$$

where q is the horizontal traction force induced by the wall, g is the gap between the wall and the approaching tumour, and A and B are parameters associated with the contact model that control the magnitude of the force, and how sharply the force rises as the tumour approaches the wall, respectively. This model ensures that the velocity fields on the impinging boundary of the tumour remain smooth in time.

Starting with the same initial conditions as the previous test (Figure 5.26), Figure 5.29 depicts the compressive horizontal stress built-up in the solid after 120 days due to the presence of the wall (not visible in the figure). Notice that the velocity vectors are much smaller in the constrained direction. Figure 5.30 shows the time evolution of the compressive horizontal stress at a point near the extreme right of the domain. The stress increases sharply as the point gets close to the wall, but remains smooth in time.

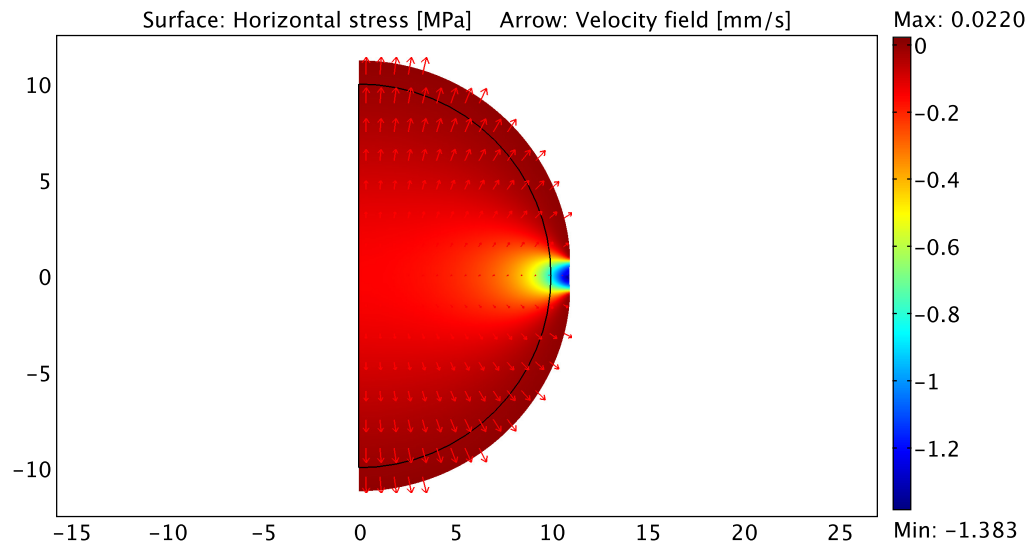


Figure 5.29: The growing tumour constrained by a wall at time $t = 120$ days.

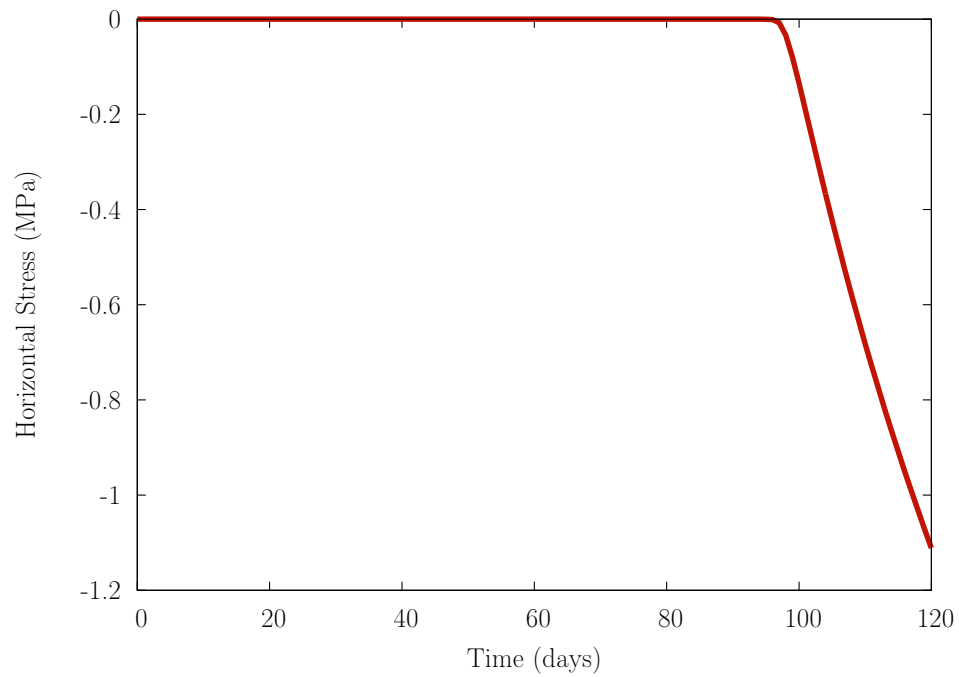


Figure 5.30: The horizontal stress in the tumour evolving over 120 days.

5.4.3 The mechanics of the cells

In order to observe just the gross kinematic swelling associated with an increase in the mass of the tumour, we have treated the tumour thus far as a homogenous solid, not distinguishing between the cells and the ECM. In this section, we turn off the growth process, and begin to differentiate between the species by decomposing the total solid stress into two parts: a “passive” stress associated with the hyperelastic response of the ECM, and an “active” stress, associated with the cellular traction forces on the surrounding medium:

$$(5.5) \quad \boldsymbol{\sigma}^c = \underbrace{\frac{1}{J} \frac{\rho_0^c}{\tilde{\rho}_0^c} \frac{\partial \hat{\psi}^c}{\partial \mathbf{F}} \mathbf{F}^T}_{\text{Passive}} + \underbrace{\tau \rho^c \rho^{\text{cell}} (N - \rho^{\text{cell}})}_{\text{Active}} \mathbf{1}.$$

This decomposition, as well as other modelling choices made in the remaining calculations, is based on the modelling work of [Namy et al. \(2004\)](#). Here, τ is a parameter that monitors the individual cellular traction amplitude, ρ^c and ρ^{cell} are the current concentrations of the ECM and the cells, respectively, and N is a real, positive constant ($N > \rho^{\text{cell}}$) that controls the cell traction inhibition when the cell density increases. The model assumes that the active stresses are proportional to the ECM concentration, and that there is a critical concentration of cells at which this active stress is maximum.

Assuming the following uniform distribution of cells and ECM, $\rho^{\text{cell}} = 0.5 \text{ kg.m}^{-3}$ and $\rho^c = 1 \text{ kg.m}^{-3}$, and the values for the constants $\tau = 1000 \text{ MPa.kg}^{-3}.\text{m}^9$ and $N = 1 \text{ kg.m}^{-3}$, [Figure 5.31](#) shows the cells uniformly pulling the matrix inward. The colour contours provide the radial displacement of the ECM. A similar calculation was performed with the non-uniform distribution of cells (ranging between 1.18 kg.m^{-3} and 4.72 kg.m^{-3}) shown in the colour contours in [Figure 5.32](#), and the deformed

domain shows the corresponding deformation of the ECM. Notice that the regions of higher cell concentrations pull their surrounding ECM neighbourhoods in greater.

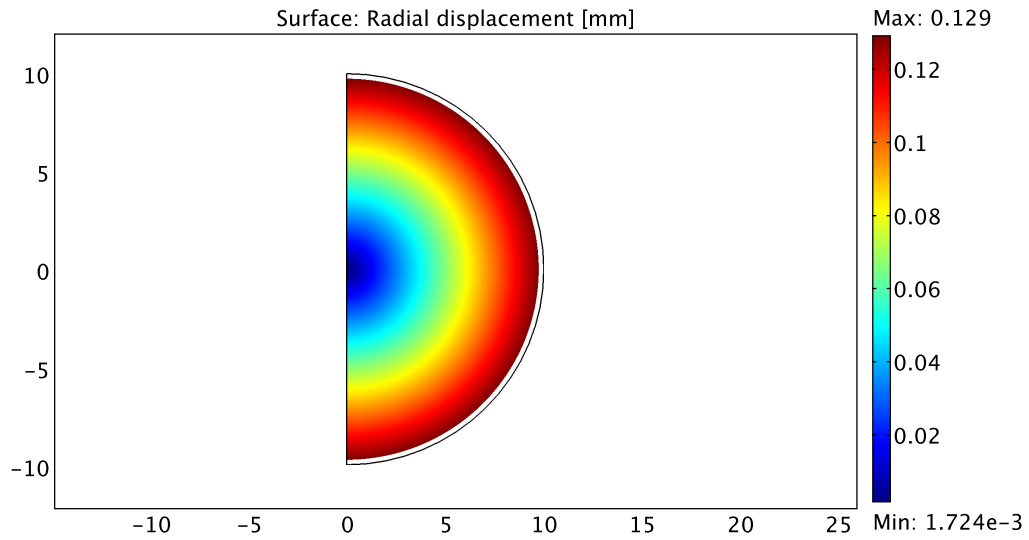


Figure 5.31: Homogeneous inward pull due to a uniform distribution of cells.

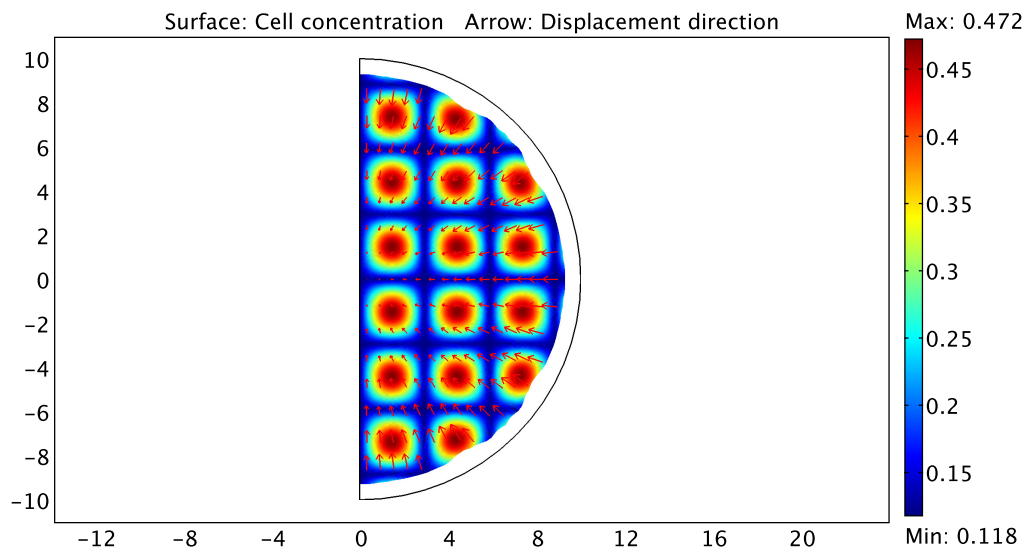


Figure 5.32: Heterogeneous traction due to a non-uniform distribution of cells.

5.4.4 The transport of the cells

In the calculations presented in the preceding section, the cell concentrations were fixed spatially and temporally. In this section, we allow for the cells to proliferate and move via diffusion and haptotaxis (again, following the work of [Namy et al. \(2004\)](#)). We solve the mass transport equation (4.2) for the cells to determine their current concentration fields. In order to account for the aforementioned modes of mass transport, we specify the following constitutive form for the cell mass flux:

$$(5.6) \quad \rho^{\text{cell}} \mathbf{v}^{\text{cell}} = \underbrace{h \rho^{\text{cell}} \text{grad}(\rho^c)}_{\text{Haptotactic flux}} - \underbrace{D^{\text{cell}} \text{grad}(\rho^{\text{cell}})}_{\text{Cell diffusion}},$$

where h is the haptotactic coefficient and D^{cell} is the diffusivity of the cells in the matrix. In this section, we are primarily interested in observing the proliferation and transport of the cells, and so we do not associate any kinematics with the changing cell concentration.

In the first set of results, we look at cell proliferation and diffusion, and observe the effect that this has on the traction that they apply on their ECM neighbourhoods. Starting with a cell-rich circle of radius 5 mm at the centre of the domain (having a uniform cell concentration of 6.266 kg.m^{-3}), and a smaller cell concentration (3.778 kg.m^{-3}) at other points on the domain; and using a uniform cell source $\pi^{\text{cell}} = 0.001 \text{ kg.m}^{-3}/\text{day}$ and a diffusion coefficient of $D^{\text{cell}} = 0.01 \text{ mm}^2/\text{day}$, Figures 5.33–5.36 show the snapshots of the diffusing and proliferating cells during the course of the test. The colour contours provide the evolving cell concentration fields (in kg.m^{-3}) and the arrows provide the deformation direction of the ECM induced by the cell traction.

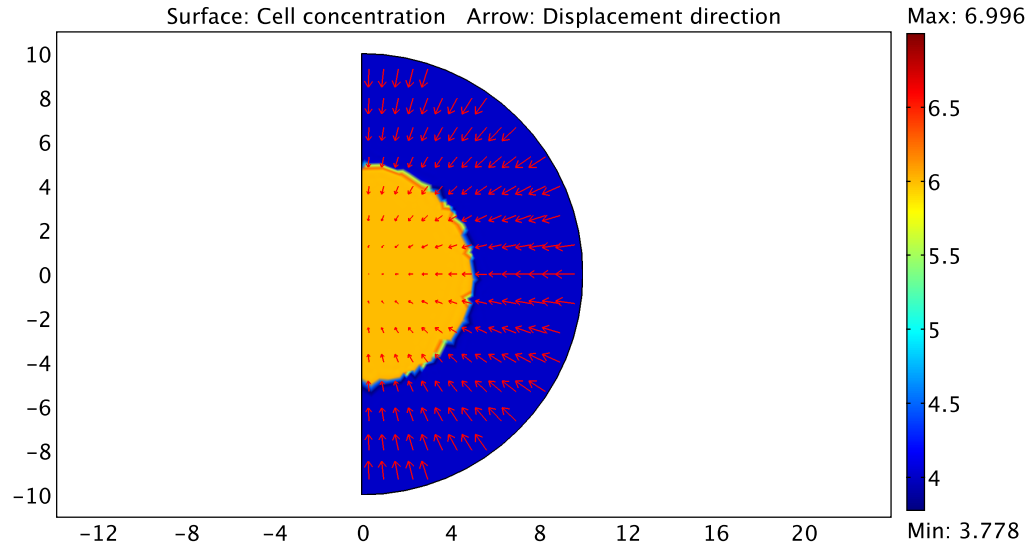


Figure 5.33: The cells diffusing and proliferating at time $t = 0$ days.

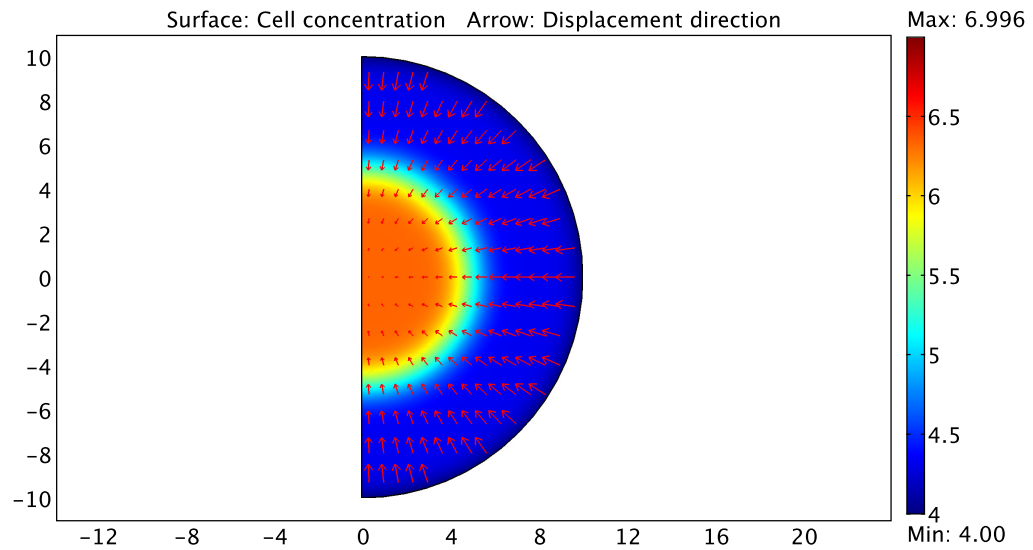


Figure 5.34: The cells diffusing and proliferating at time $t = 33$ days.

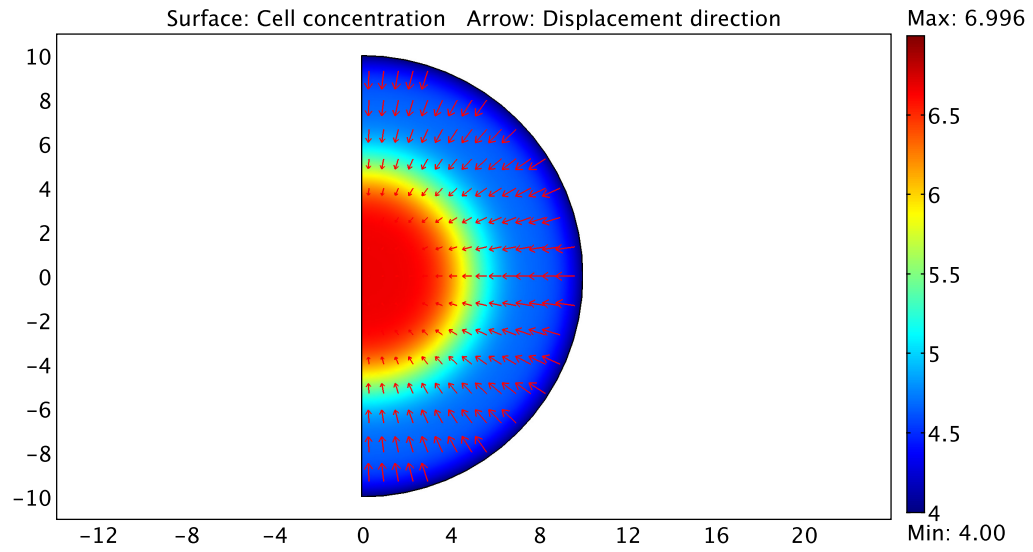


Figure 5.35: The cells diffusing and proliferating at time $t = 67$ days.

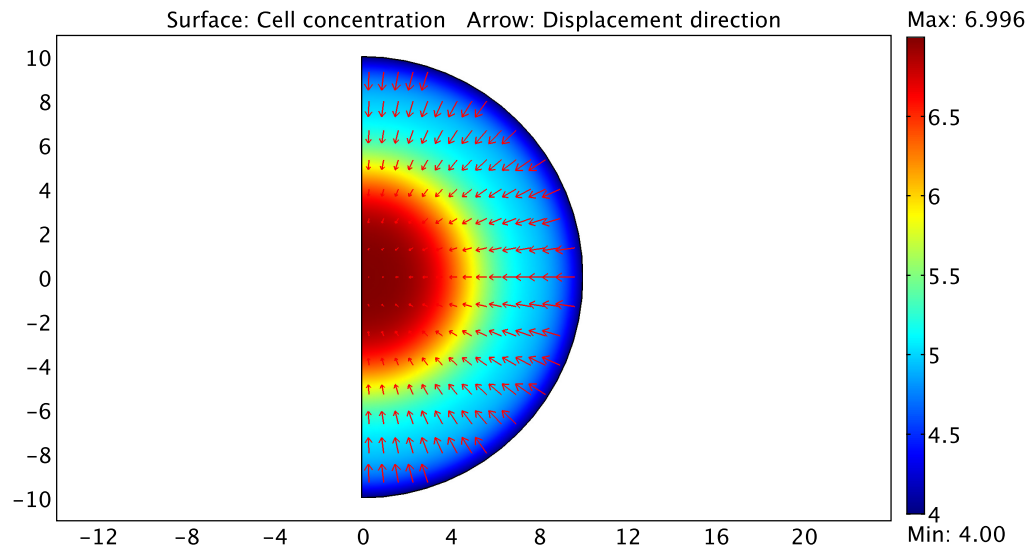


Figure 5.36: The cells diffusing and proliferating at time $t = 100$ days.

In the second set of results, we look at cell proliferation and haptotaxis, and observe the effect that this has on the traction that the cells apply on their ECM neighbourhoods. We start this test with the same initial conditions for the cells as the previous calculation (a cell-rich bulb at the centre of the domain), but in order to induce haptotaxis, we begin with the heterogeneous ECM concentration (varying between $0.5 \text{ kg}\cdot\text{m}^{-3}$ and $1.5 \text{ kg}\cdot\text{m}^{-3}$), seen in Figure 5.37. In these tests, the haptotactic coefficient h is $0.1 \text{ mm}^2\cdot\text{day}^{-1}\cdot\text{mm}^3\cdot\text{kg}^{-1}$. Figures 5.38–5.41 show snapshots of the cells undergoing haptotaxis and proliferating during the course of the test. The colour contours provide the evolving cell concentration fields (in $\text{kg}\cdot\text{m}^{-3}$) and the arrows provide the deformation direction of the ECM, induced by the cell traction. We observe that the cells migrate toward areas of higher ECM while proliferating. Note that the directionality of the cell traction field changes correspondingly with the concentration field, as noted by the lengths and directions of the arrows.

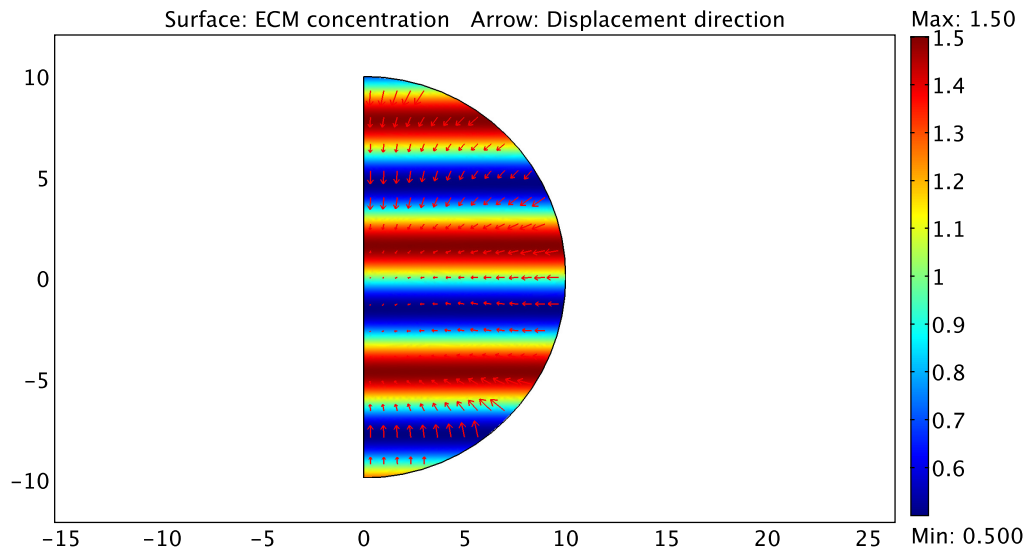


Figure 5.37: Heterogeneous extra-cellular matrix concentration ($\text{kg}\cdot\text{m}^{-3}$).

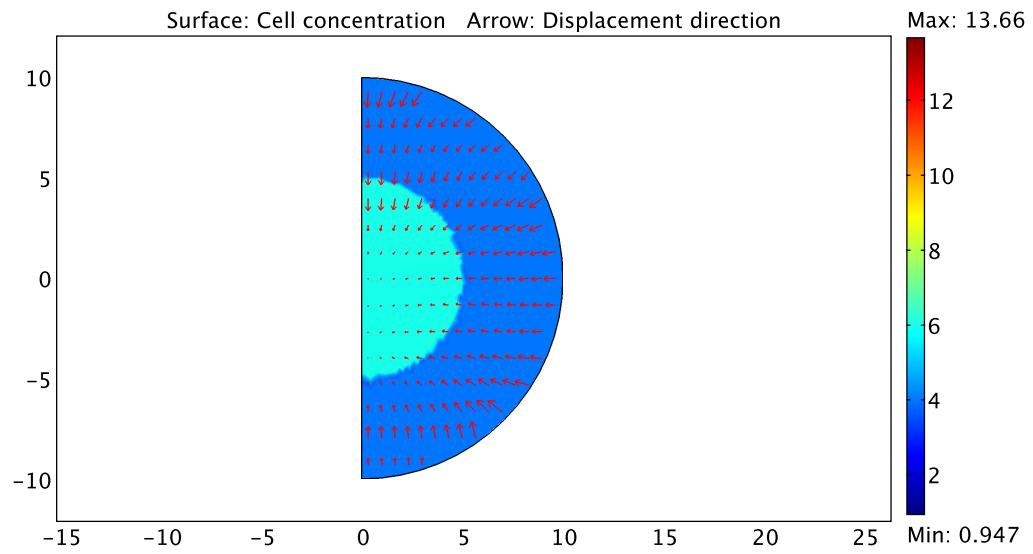


Figure 5.38: Proliferating cells undergoing haptotaxis at time $t = 0$ days.

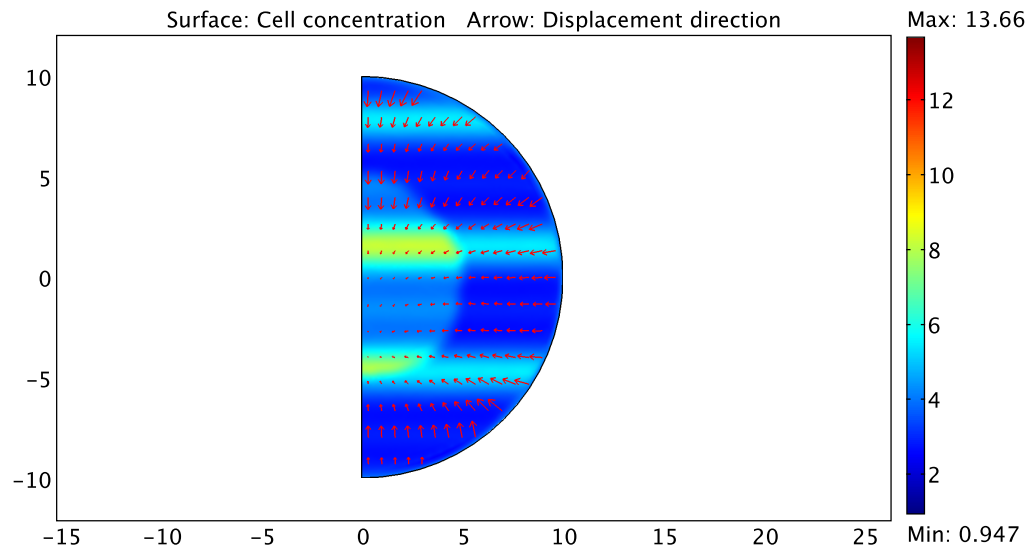


Figure 5.39: Proliferating cells undergoing haptotaxis at time $t = 33$ days.

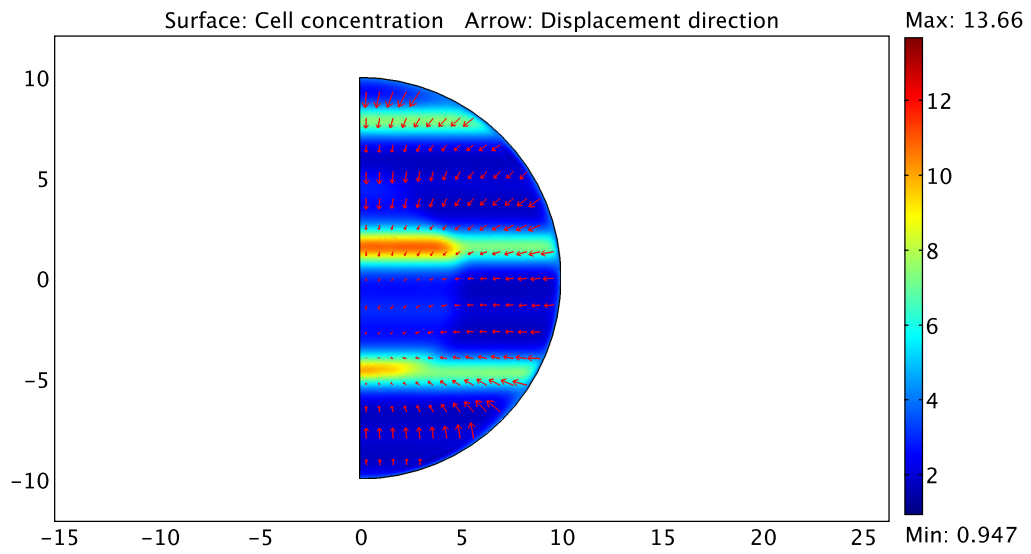


Figure 5.40: Proliferating cells undergoing haptotaxis at time $t = 67$ days.

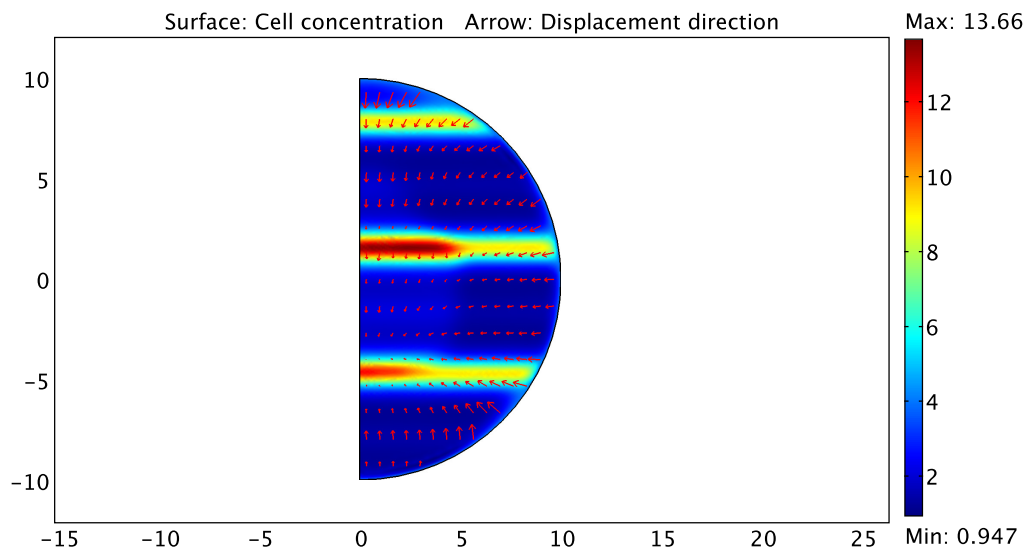


Figure 5.41: Proliferating cells undergoing haptotaxis at time $t = 100$ days.

While the magnitudes for the cell diffusivity, D^{cell} , and haptotactic coefficient, h , are arbitrarily chosen, following the experimental data cited in [Namy et al. \(2004\)](#), the numerical value assumed for h is an order of magnitude greater than that assumed for D^{cell} , which ensures that when the two modes for mass transport are combined, haptotaxis is the dominant mechanism.

5.4.5 Coupling the phenomena

With the individual phenomena explored, we are now ready to solve the coupled problem described initially. The range of physics incorporated into this problem include proliferating cells undergoing both diffusion and haptotaxis, a rate law for the production of additional ECM which scales linearly with the concentration of cells, the stress within the cells induced by their traction, the hyperelastic response of the ECM, isotropic kinematic swelling associated with the increase in tumour mass, and finally, this swelling constrained by the presence of a wall.

Figures [5.42–5.47](#) show snapshots of the growing tumour constrained by the wall. The colour contours provide the x-displacement of the swelling tumour and the arrows provide the direction of the velocity field. Observe that regions having a higher cell concentration due to haptotaxis (refer [Figures 5.38–5.41](#)) tend to swell faster than regions with lower cell concentrations. Also observe that due to the presence of the wall, even as early as 20 days, the velocities are biased toward the vertical direction. Finally, upon comparing these constrained tumour growth snapshots with [Figure 5.48](#), which is a result of a similar calculation without the wall, it is clear that the presence of the compressive stress along a direction inhibits growth along that direction, which is what we were aiming to see.

It must be reiterated here that the results provided in this section are only to demonstrate that varying classes of physics can be incorporated into the existing mathematical and computational formulation. These results have been obtained using an isotropic growth law (5.3), without requiring the stress-dependent time rate of the growth portion of the deformation gradient derived in Section 4.2.5. It is not yet clear whether the constraint from the mechanical loads just deforms the tissue and distorts its shape, or whether the cells have some ability to sense the local stress state and this affects directionality of further growth. More research into experimental literature is needed before a conclusive statement can be made.

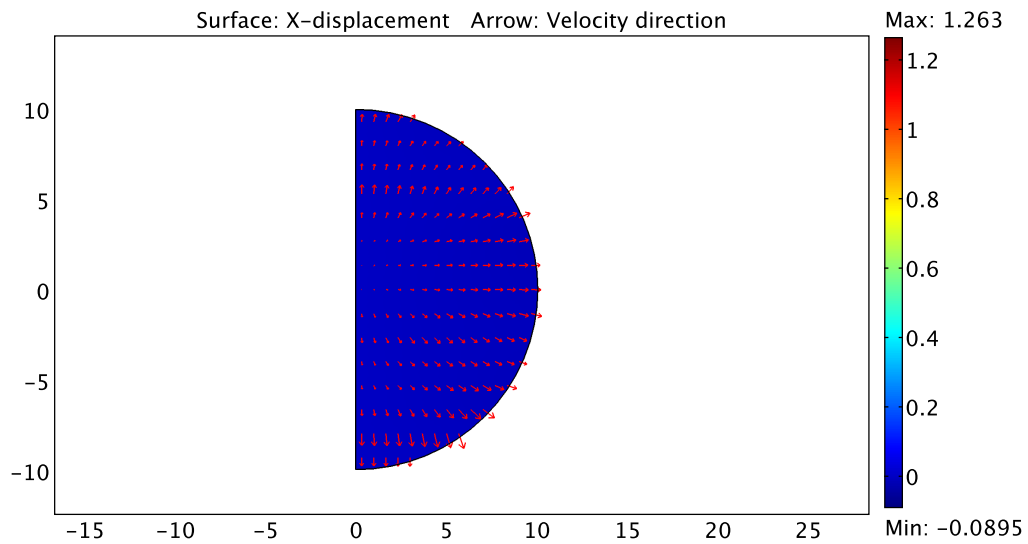


Figure 5.42: A constrained growing tumour at $t = 0$ days.

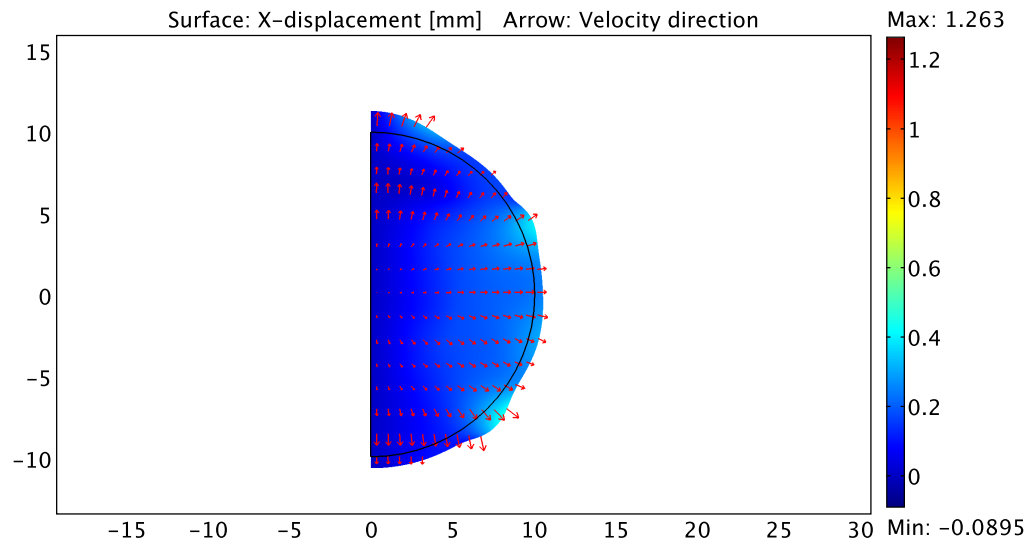


Figure 5.43: A constrained growing tumour at $t = 20$ days.

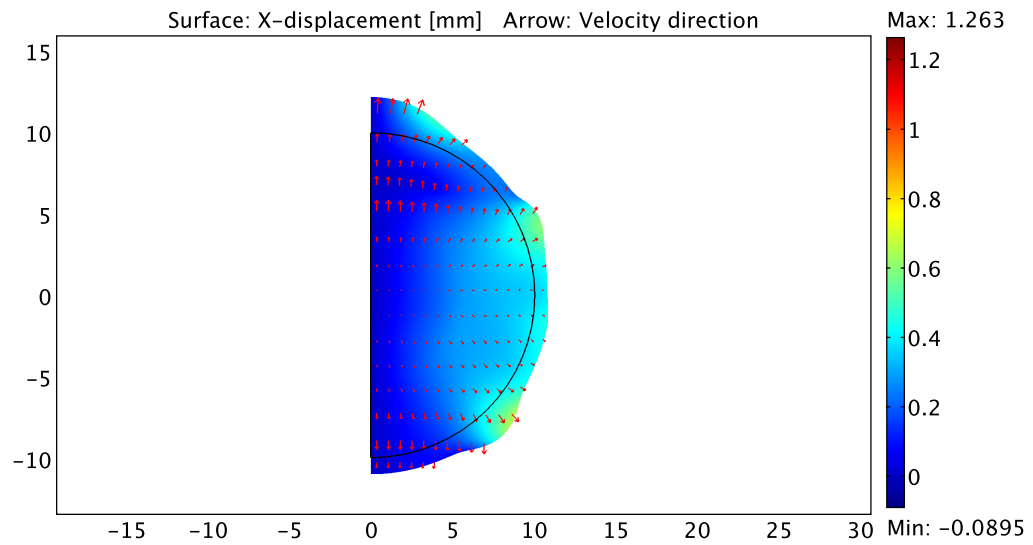


Figure 5.44: A constrained growing tumour at $t = 40$ days.

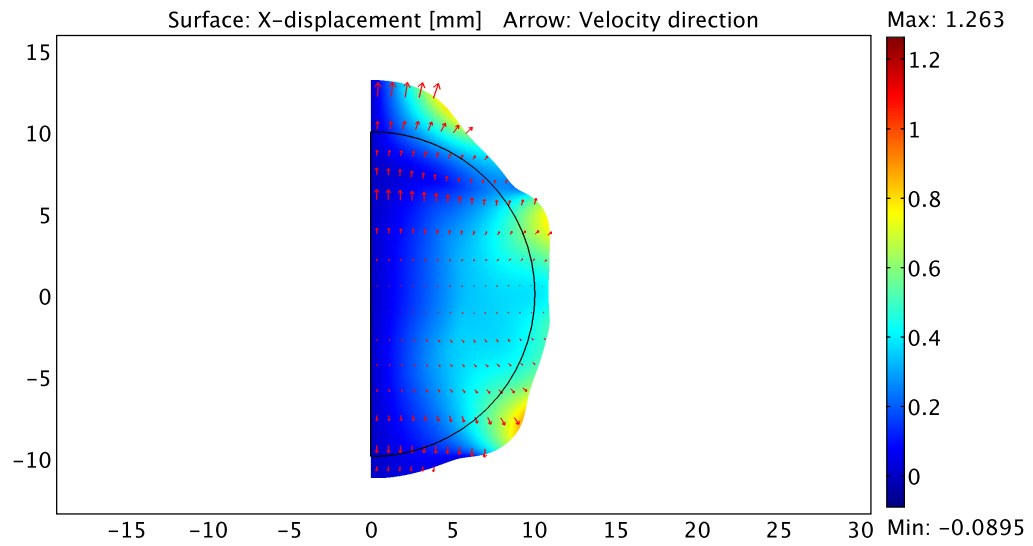


Figure 5.45: A constrained growing tumour at $t = 60$ days.

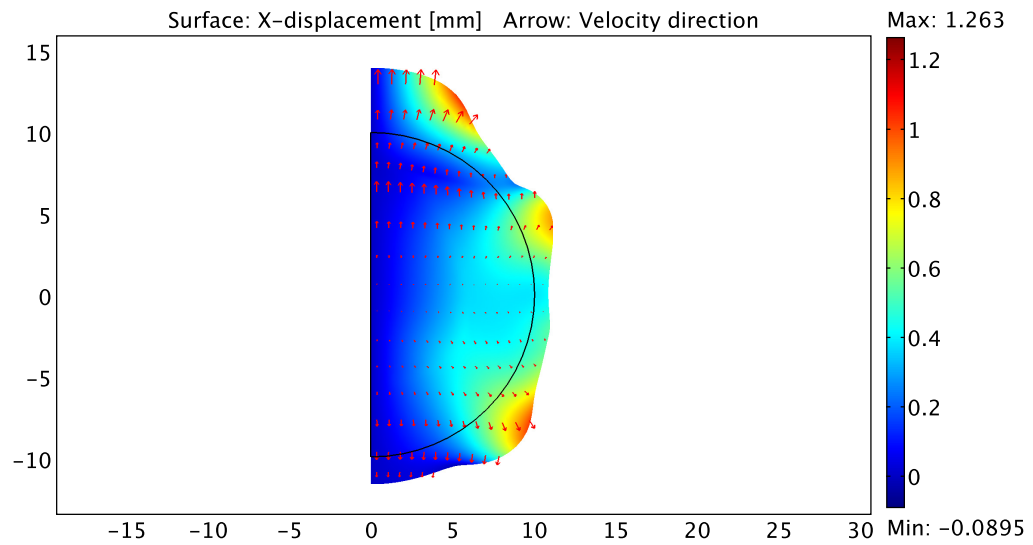


Figure 5.46: A constrained growing tumour at $t = 80$ days.

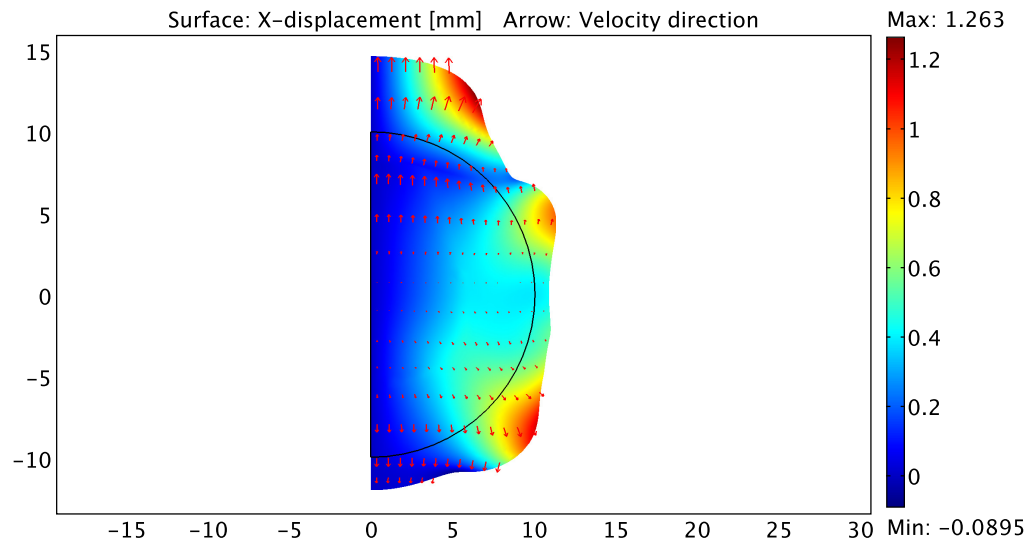


Figure 5.47: A constrained growing tumour at $t = 100$ days.

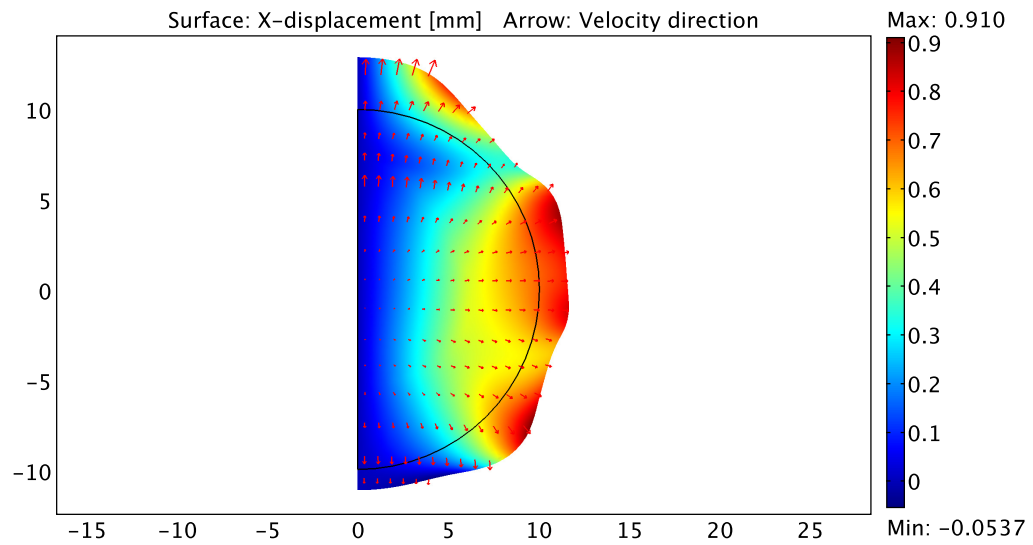


Figure 5.48: An unconstrained growing tumour at $t = 80$ days.

CHAPTER 6

Concluding remarks

This dissertation presented a number of significant enhancements to our original growth formulation presented in [Garikipati et al. \(2004\)](#). With the reformulation of the theory in an Eulerian setting in Chapter 4, the governing equations for the fluid phase are now recast in terms of the fluid concentration, velocity and pressure; primitive variables that are natural to fluid mechanics. This, along with the revised computational formulation that solves the momentum balance equations for each species separately, retaining all aspects of the coupling between the equations, has rapidly led to the establishment of a practical environment to study the biphasic mechanics response of soft tissues. While the computational examples presented in this dissertation focused mostly on the interaction between elastic phases, it has proven straightforward to extend it to more involved cases, such as studying the flow of a viscous fluid through a porous, hyperelastic solid. Thus, the computational formulation potentially provides a means to systematically explore the various sources of rate-dependent behaviour in soft tissues: the viscoelastic deformation of the collagen network, the viscosity of the extra-cellular fluid, frictional effects arising from stress-driven fluid flow through the network, as well as suitable combinations of these effects.

Carefully revisiting the assumptions underlying the behaviour of mixtures, and taking a close look anew at the Dissipation-Inequality, in an attempt at constitu-

tive specification to satisfy it a priori, brought to light some new, key, constitutive relations. This is another significant aspect of this work.

One key relationship was for the mass interconversion terms that suggested that it is the energetic difference between the reactants and the products of a chemical reaction that drive the reaction forward; a well-established concept in chemistry. This broad guideline allows for the specification of a very general class of source terms representing varying kinds of biochemistry, yet retaining consistency with the thermodynamics.

Perhaps the most exciting result that arose from this analysis of the implications of the Dissipation-Inequality was the dissipation-driven growth tensor presented in Section 4.2.5. Experimental work on wound healing in ligaments ([Provenzano et al., 2003](#)) and stress-based inhibition of tumour growth ([Helmlinger et al., 1997](#)) seems to suggest that the processes underlying biological growth are dependent upon the local stress field in a related manner. However, a direct correlation with experiment, if found, will be a manifestation in Biology of a phenomenon that is common in Materials Physics.

APPENDICES

APPENDIX A

A review of mathematical results

The following sections catalogue some classical mathematical results that have been frequently called-upon during the course of the development of the theoretical formulation in Chapters 2 and 4.¹

A.1 Gauss-Green's divergence theorem

Let $\Omega \subset \mathbf{R}^n$ be a bounded open set with a C^1 boundary, let $\boldsymbol{\nu}_\Omega: \partial\Omega \rightarrow \mathbf{R}^n$ be the exterior unit normal vector to Ω at a point x and let $\mathbf{v}: \overline{\Omega} \rightarrow \mathbf{R}^n$ be a vector function in $C^0(\overline{\Omega}, \mathbf{R}^n) \cap C^1(\Omega, \mathbf{R}^n)$. Then,

$$\int_{\Omega} \operatorname{div} \mathbf{v}(x) \, dx = \int_{\partial\Omega} \langle \mathbf{v}(x), \boldsymbol{\nu}_\Omega(x) \rangle \, d\sigma(x).$$

Here, the operator $\operatorname{div} \mathbf{v}$ is the divergence of the vector field \mathbf{v} , and is denoted as $\operatorname{DIV}(\mathbf{v})$ and $\operatorname{div}(\mathbf{v})$ in the reference and current configurations, respectively, in the main body of this dissertation. The term $d\sigma$ in the surface integral on the right hand-side is the area measure corresponding to $\partial\Omega$. In the main body of this dissertation, the scalar product in the second integral is written as $\mathbf{v} \cdot \mathbf{N}$ and $\mathbf{v} \cdot \mathbf{n}$ when

¹The material presented in Appendix A is covered under the GNU Free Documentation License (See <http://www.gnu.org/copyleft/>). This affords the reader the freedom to copy and redistribute the matter with or without modification, either commercially or noncommercially.

working with quantities in the reference and current configurations, respectively, and represents the *normal component* of \mathbf{v} with respect to $\partial\Omega$; hence the whole integral represents the *flux* of the vector \mathbf{v} through $\partial\Omega$.

The theorem as stated for the vector function \mathbf{v} can be extended to the following forms which prove useful in the development of the theory:

$$\int_{\Omega} \operatorname{grad}\mathbf{v}(x) \, dx = \int_{\partial\Omega} \mathbf{v}(x) \otimes \boldsymbol{\nu}_{\Omega}(x) \, d\sigma(x),$$

$$\int_{\Omega} \operatorname{curl}\mathbf{v}(x) \, dx = \int_{\partial\Omega} \mathbf{v}(x) \times \boldsymbol{\nu}_{\Omega}(x) \, d\sigma(x), \text{ and}$$

$$\int_{\Omega} \operatorname{div}\mathbf{T}(x) \, dx = \int_{\partial\Omega} \mathbf{T}(x) \boldsymbol{\nu}_{\Omega}(x) \, d\sigma(x),$$

where $\mathbf{T}: \mathbf{R}^n \rightarrow \mathbf{R}^n$ is a tensor function.

A.2 Reynolds' transport theorem

Introduction *Reynolds' transport theorem* (Reynolds, 1903) is a fundamental theorem used in formulating the basic laws of fluid mechanics. For our purpose, let us consider a fluid flow, characterised by its streamlines, in the Euclidean vector space $(\mathbb{R}^3, \|\cdot\|)$. Embedded in this, we consider a continuum body \mathcal{B} occupying a volume \mathcal{V} whose particles are fixed by their material (Lagrangian) coordinates \mathbf{X} , and a control volume \mathbf{v} , bounded by the control surface $\partial\mathbf{v}$, whose points are fixed by their spatial (Eulerian) coordinates, \mathbf{x} .

Definition 1. *We define an extensive tensor property by the expression*

$$(A.1) \quad \Psi(\mathbf{x}, t) := \int_{\mathbf{v}} \psi(\mathbf{x}, t) \rho(\mathbf{x}, t) \, dv,$$

where $\psi(\mathbf{x}, t)$ is the respective intensive tensor property.

Theorem's hypothesis The kinematics of the continuum can be described by a diffeomorphism χ which, at any given instant $t \in [0, \infty) \subset \mathbb{R}$, gives the spatial coordinates \mathbf{x} of the material particle \mathbf{X} ,

$$\mathcal{V} \times [0, \infty) \rightarrow \mathbf{v} \times [0, \infty), \quad t \mapsto t, \quad \mathbf{X} \mapsto \mathbf{x} = \chi(\mathbf{X}, t).$$

Indeed the above sentence corresponds to a change of coordinates which must verify

$$J = \left| \frac{\partial x_i}{\partial X_j} \right| \equiv |F_{ij}| \neq 0, \quad F_{ij} := \frac{\partial x_i}{\partial X_j},$$

J being the Jacobian of transformation ($dv = JdV$) and F_{ij} , the Cartesian components of the *deformation gradient tensor* \mathbf{F} .

Theorem The material rate of an extensive tensor property associated with a continuum body \mathcal{B} is equal to the local rate of the property in a control volume \mathbf{v} plus the efflux of the respective intensive property across its control surface $\partial\mathbf{v}$.

Proof. By taking on Equation (A.1) the material time derivative, and applying Gauss-Green's Divergence Theorem, we have,

$$\begin{aligned} \frac{D\Psi}{Dt} &= \overline{\int_{\mathbf{v}} \dot{\psi\rho} dv} = \overline{\int_{\mathcal{V}} \dot{\psi\rho} J dV} = \int_{\mathcal{V}} \overline{\dot{\psi\rho} J} dV = \int_{\mathcal{V}} (\overline{\dot{\psi\rho} J} + \psi\rho \dot{J}) dV = \\ &= \int_{\mathcal{V}} \left\{ J \left[\frac{\partial}{\partial t}(\psi\rho) + \mathbf{v} \cdot \nabla_x(\psi\rho) \right] + \psi\rho (J \nabla_x \cdot \mathbf{v}) \right\} dV = \\ &= \int_{\mathcal{V}} \left\{ \left[\frac{\partial}{\partial t}(\psi\rho) \right] + [\mathbf{v} \cdot \nabla_x(\psi\rho) + (\psi\rho) \nabla_x \cdot \mathbf{v}] \right\} (J dV) \\ &= \int_{\mathbf{v}} \frac{\partial}{\partial t}(\psi\rho) dv + \int_{\mathbf{v}} \nabla_x \cdot (\psi\rho \mathbf{v}) dv = \frac{\partial}{\partial t} \int_{\mathbf{v}} \psi\rho dv + \int_{\partial\mathbf{v}} \psi\rho \mathbf{v} \cdot \mathbf{n} da, \end{aligned}$$

Finally, by using Equation (A.1) on the first integral in the right hand-side of the last line, we obtain

$$(A.2) \quad \dot{\Psi} = \frac{\partial \Psi}{\partial t} + \int_{\partial v} \psi \rho \mathbf{v} \cdot \mathbf{n} da,$$

endorsing the theorem statement.

□

APPENDIX B

Supplementary topics

B.1 Frame invariance and flux contribution from acceleration

In our earlier treatment ([Garikipati et al., 2004](#)), the constitutive relation for the fluid flux had a driving force contribution arising from the acceleration of the solid phase, $-\rho_0^f \mathbf{F}^T \frac{\partial \mathbf{V}}{\partial t}$. This term, being motivated by the reduced dissipation inequality, does not violate the Second Law and supports an intuitive understanding that the acceleration of the solid skeleton in one direction must result in an inertial driving force on the fluid in the opposite direction. However, as defined, this acceleration is obtained by the time differentiation of kinematic quantities,¹ and does not transform in a frame-indifferent manner. Unlike the superficially similar term arising from the gravity vector,² the acceleration term presents an improper dependence on the frame of the observer. Thus, its use in constitutive relations is inappropriate, and the term has been dropped in Equation (2.33).

¹And not in terms of acceleration *relative to fixed stars* for e.g., as discussed in ([Truesdell and Noll, 1965](#), Page 43).

²Where every observer has an implicit knowledge of the directionality of the field relative to a fixed frame, allowing it to transform objectively. Specifically, under a time-dependent rigid body motion imposed on the current configuration carrying \mathbf{x} to $\mathbf{x}^+ = \mathbf{c}(t) + \mathbf{Q}(t)\mathbf{x}$, where $\mathbf{c}(t) \in \mathbb{R}^3$ and $\mathbf{Q}(t) \in \text{SO}(3)$, it is understood that the acceleration due to gravity in the transformed frame is $\mathbf{g}^+ = \mathbf{Q}^T \mathbf{g}$ and is therefore frame-invariant. However, $\mathbf{a}^+ = \ddot{\mathbf{c}} + 2\dot{\mathbf{Q}}\mathbf{v} + \ddot{\mathbf{Q}}\mathbf{x} + \mathbf{Q}\mathbf{a}$, and is therefore not frame-invariant.

B.2 Stabilisation of the simplified solute transport equation

In weak form, the SUPG-stabilised method (Hughes et al., 1987) for Equation (2.48) is,

$$\begin{aligned}
 & \int_{\Omega} w^h \left(\frac{d\rho^{sh}}{dt} + \mathbf{m}^f \cdot \text{grad} \left[\frac{\rho^{sh}}{\rho^f} \right] \right) d\Omega \\
 & + \int_{\Omega} \left(\text{grad} [w^h] \cdot \bar{\mathbf{D}}^s \text{grad} \left[\rho^{sh} \right] \right) d\Omega \\
 \text{(B.1)} \quad & + \sum_{e=1}^{n_{el}} \int_{\Omega_e} \tau \frac{\mathbf{m}^f}{\rho^f} \cdot \text{grad} [w^h] \left(\frac{d\rho^{sh}}{dt} + \mathbf{m}^f \cdot \text{grad} \left[\frac{\rho^{sh}}{\rho^f} \right] \right) d\Omega \\
 & - \sum_{e=1}^{n_{el}} \int_{\Omega_e} \tau \frac{\mathbf{m}^f}{\rho^f} \cdot \text{grad} [w^h] \left(\text{div} \left[\bar{\mathbf{D}}^s \text{grad} \left[\rho^{sh} \right] \right] \right) d\Omega \\
 & = \int_{\Omega} w^h \pi^s d\Omega + \int_{\Gamma_h} w^h h d\Gamma \\
 & + \sum_{e=1}^{n_{el}} \int_{\Omega_e} \tau \frac{\mathbf{m}^f}{\rho^f} \cdot \text{grad} [w^h] \pi^s d\Omega,
 \end{aligned}$$

where quantities with the superscript h represent finite-dimensional approximations of infinite-dimensional field variables, Γ_h is the Neumann boundary, and this equation introduces a numerical stabilisation parameter, τ , which we calculate from the L_2 norms of element level matrices, as described in Tezduyar and Sathe (2003).

BIBLIOGRAPHY

BIBLIOGRAPHY

- Alberts, B., Johnson, A., Lewis, J., Raff, M., Roberts, K., Walter, P., 2002. *Molecular Biology of the Cell*. Garland Science, Oxford. 38, 52
- Ambrosi, D., Mollica, F., 2002. On the mechanics of a growing tumor. *Int. J. Engr. Sci.* 40, 1297–1316. 2, 21, 38
- Armero, F., 1999. Formulation and finite element implementation of a multiplicative model of coupled poro-plasticity at finite strains under fully-saturated conditions. *Comp. Methods in Applied Mech. Engrg.* 171, 205–241. 49
- Arruda, E. M., Calve, S. C., Garikipati, K., Gosh, K., Narayanan, H., 2005. Characterization and Modeling of Growth and Remodeling in Tendon and Soft Tissue Constructs. In: *Proceedings of the IUTAM symposium on Mechanics of Biological Tissue*. iv, 66, 67
- Ateshian, G. A., 2007. On the theory of reactive mixtures for modeling biological growth. *Biomechanics and Modeling in Mechanobiology* . 3, 83, 99
- Bedford, A., Drumheller, D., 1983. Theories of immiscible and structured mixtures. *International Journal of Engineering Science* 21 (8), 863 – 960. 2, 80
- Bilby, B., Smith, E., 1956. Continuous distributions of dislocations. iii. *Proceedings of the Royal Society of London, Series A (Mathematical and Physical Sciences)* 236 (1207), 481 – 505. 21
- Bischoff, J. E., Arruda, E. M., Gosh, K., 2002a. A microstructurally based orthotropic hyperelastic constitutive law. *J. Applied Mechanics* 69, 570–579. 30
- Bischoff, J. E., Arruda, E. M., Gosh, K., 2002b. Orthotropic elasticity in terms of an arbitrary molecular chain model. *J. Applied Mechanics* 69, 198–201. 30
- Bowen, R. M., 1976. Theory of mixtures. In: Eringen, A. E. (Ed.), *Continuum Physics*. Vol. 3. Academic, New York., pp. 1–127. 73
- Brennen, C. E., 1995. *Cavitation and Bubble Dynamics*. Oxford University Press. 33
- Bromberg, S., Dill, K. A., 2002. *Molecular Driving Forces: Statistical Thermodynamics in Chemistry and Biology*. Garland. 40

- Brooks, A., Hughes, T., 1982. Streamline upwind/Petrov-Galerkin formulations for convection dominated flows with particular emphasis on the incompressible Navier-Stokes equations. *Comp. Methods in Applied Mech. Engrg.* 32, 199–259. [43](#)
- Bustamante, C., Bryant, Z., Smith, S. B., 2003. Ten years of tension: Single-molecule DNA mechanics. *Nature* 421, 423–427. [30](#)
- Byrne, H. M., Alarcon, T., Owen, M. R., Webb, S. D., Maini, P. K., 2006. Modelling aspects of cancer dynamics: a review. *Philosophical Transactions of the Royal Society of London. Series A* 364, 1563–1578. [3](#)
- Calve, S., Dennis, R., Kosnik, P., Baar, K., Grosh, K., Arruda, E., 2004. Engineering of functional tendon. *Tissue Engineering* 10, 755–761. [iv](#), [3](#), [50](#), [51](#)
- Calve, S., Lytle, I. F., Ma, J., Grosh, K., Brown, D. L., Arruda, E. M., 2007. In vivo conditioning increases tensile strength and collagen content of self-assembled tendon constructs. *In preparation* . [38](#), [40](#)
- Cowin, S. C., Hegedus, D. H., 1976. Bone remodeling I: Theory of adaptive elasticity. *J. Elast.* 6, 313–326. [2](#), [4](#), [38](#)
- DiSilvestro, M. R., Zhu, Q., Wong, M., Jurvelin, J. S., Suh, J.-K. F., 2001. Biphasic poroviscoelastic simulation of the unconfined compression of articular cartilage: I- Simultaneous prediction of reaction force and lateral displacement. *J. Bio. Mech. Engrg.* 123, 191–197. [101](#)
- Donea, J., Huerta, A., Ponthot, J.-P., Rodríguez-Ferran, A., 2004. Arbitrary Lagrangian-Eulerian Methods. In: Stein, E., de Borst, R., Hughes, T. J. (Eds.), *Encyclopedia of Computational Mechanics. Volume 1: Fundamentals*. John Wiley & Sons, Ltd. [101](#)
- Epstein, M., Maugin, G. A., 2000. Thermomechanics of volumetric growth in uniform bodies. *International Journal of Plasticity* 16, 951–978. [2](#), [4](#), [16](#), [38](#)
- Eyring, H., 1936. Viscosity, plasticity, and diffusion as examples as absolute reaction rates. *J. Chem. Phys.* 4, 283–291. [91](#)
- Garikipati, K., Arruda, E. M., Grosh, K., Narayanan, H., Calve, S., 2004. A continuum treatment of growth in biological tissue: Mass transport coupled with mechanics. *Journal of Mechanics and Physics of Solids* 52 (7), 1595–1625. [3](#), [4](#), [141](#), [148](#)
- Garikipati, K., Bassman, L. C., Deal, M. D., 2001. A lattice-based micromechanical continuum formulation for stress-driven mass transport in polycrystalline solids. *Journal of Mechanics and Physics of Solids* 49, 1209–1237. [49](#)
- Garikipati, K., Rao, V. S., 2001. Recent advances in models for thermal oxidation of silicon. *jcp* 174, 138–170. [49](#)

- Graham, J. S., Vomund, A. N., Phillips, C. L., Grandbois, M., 2004. Structural changes in human type I collagen fibrils investigated by force spectroscopy. *Experimental Cell Research* 299, 335–342. [30](#)
- Han, S., Gemmell, S. J., Helmer, K. G., Grigg, P., Wellen, J. W., Hoffman, A. H., Sotak, C. H., 2000. Changes in ADC caused by tensile loading of rabbit achilles tendon: Evidence for water transport. *Journal of Magnetic Resonance* 144, 217–227. [35](#), [51](#)
- Harrigan, T. P., Hamilton, J. J., 1993. Finite element simulation of adaptive bone remodelling: A stability criterion and a time stepping method. *Int. J. Numer. Methods Engrg.* 36, 837–854. [40](#)
- Helmlinger, G., Netti, P. A., Lichtenbeld, H. C., Melder, R. J., Jain, R. K., 1997. Solid stress inhibits the growth of multicellular tumor spheroids. *Nature Biotechnology* 15, 778–783. [122](#), [142](#)
- Holzappel, G., 1996. On large strain viscoelasticity: continuum formulation and finite element applications to elastomeric structures. *International Journal for Numerical Methods in Engineering* 39 (22), 3903 – 26. [89](#)
- Hughes, T., Franca, L., Mallet, M., 1987. A new finite element formulation for computational fluid dynamics: VII. Convergence analysis of the generalized SUPG formulation for linear time-dependent multidimensional advective-diffusive systems. *Comp. Methods in Applied Mech. Engrg.* 63 (1), 97–112. [43](#), [47](#), [149](#)
- Humphrey, J. D., Rajagopal, 2002. A constrained mixture model for growth and remodeling of soft tissues. *Math. Meth. Mod. App. Sci.* 12 (3), 407–430. [2](#)
- Idiart, M., Castaneda, P. P., 2003. Field fluctuations and macroscopic properties for nonlinear composites. *Int. J. Solids and Structures* 40, 7015–7033. [5](#)
- Jackson, T. L., Byrne, H. M., 2000. Mathematical model to study the effects of drug resistance and vasculature on the response of solid tumors to chemotherapy. *Mathematical Biosciences* 164 (1), 17 – 38. [122](#)
- Jackson, T. L., Byrne, H. M., 2002. A mechanical model of tumor encapsulation and transcapsular spread. *Mathematical Biosciences* 180, 307–328. [3](#)
- Klisch, S. M., van Dyke, T. J., Hoger, A., 2001. A theory of volumetric growth for compressible elastic biological materials. *Math. Mech. Solids* 6, 551–575. [2](#), [20](#)
- Kratky, O., Porod, G., 1949. Röntgenuntersuchungen gelöster Fadenmoleküle. *Recueil Trav. Chim* 68, 1106–1122. [30](#)
- Landau, L. D., Lifshitz, E. M., 1951. *A Course on Theoretical Physics, Volume 5, Statistical Physics, Part I.* Butterworth Heinemann (reprint). [30](#)
- Lee, E. H., 1969. Elastic-Plastic Deformation at Finite Strains. *J. Applied Mechanics* 36, 1–6. [21](#)

- LeVeque, R. J., 2007. Finite Difference Methods for Ordinary and Partial Differential Equations: Steady State and Time Dependent Problems. Society for Industrial and Applied Mathematics (SIAM), Philadelphia. 98
- Loret, B., Simões, F. M. F., 2005. A framework for deformation, generalized diffusion, mass transfer and growth in multi-species multi-phase biological tissues. *European Journal of Mechanics A/Solids* 24, 757–781. 3, 83
- Lubarda, V. A., Hoger, A., 2002. On the mechanics of solids with a growing mass. *Int. J. Solids and Structures* 29, 4627–4664. 2, 21
- Ma, J., 2007. Development and characterization of engineered, scaffold-less bone and ligament tissues. *In preparation* . v, 3, 112, 113
- Marko, J. F., Siggia, E. D., 1995. Stretching DNA. *Macromolecules* 28, 8759–8770. 30
- Massoudi, M., 2003. Constitutive relations for the interaction force in multi-component particulate flows. *International Journal of Non-Linear Mechanics* 38, 313–336. 95
- Mooney, M., 1940. A theory of large elastic deformation. *Journal of Applied Physics* 11, 582–592. 99
- Mow, V., Kuei, S., Lai, W., Armstrong, C., 1980. Biphasic creep and stress relaxation of articular cartilage in compression: Theory and experiments. *Journal of Biomechanical Engineering* 102(1), 73–84. 99
- Namy, P., Ohayon, J., Tracqui, P., 2004. Critical conditions for pattern formation and in vitro tubulogenesis driven by cellular traction fields. *Journal of Theoretical Biology* 227, 103–120. 8, 128, 130, 136
- Newton, I., 1726. Sir Isaac Newton’s Mathematical Principles of Natural Philosophy and his System of the World. Edited by Florian Cajori. Translated by Andrew Motte. Berkeley. University of California Press, 1962. 70
- Nomura, T., Hughes, T., 1992. An arbitrary Lagrangian-Eulerian finite element method for interaction of fluid and a rigid body. *Computer Methods in Applied Mechanics and Engineering* 95 (1), 115–38. 101
- Nordin, M., Lorenz, T., Campello, M., 2001. Biomechanics of tendons and ligaments. In: Nordin, M., Frankel, V. H. (Eds.), *Basic Biomechanics of the Musculoskeletal System*. Lippincott Williams and Wilkins, N.Y., pp. 102–125. 8
- Passman, S. L., Nunziato, J. W., Walsh, E. K., 1984. A theory of multiphase mixtures. In: Truedell, C. (Ed.), *Rational Thermodynamics*. Springer-Verlag, New York., pp. 286–325. 73, 99
- Preziosi, L., Farina, A., 2002. On Darcy’s Law for growing porous media. *Int. J. Non-linear Mech.* 37, 485–491. 2

- Provenzano, P., Lakes, R., Keenan, T., Vanderby, R., 2001. Nonlinear ligament viscoelasticity. *Annals Biomed. Engr.* 29, 908–914. 87
- Provenzano, P. P., Martinez, D. A., Grindeland, R. E., Dwyver, K. W., Turner, J., Vailas, A. C., Vanderby, R., 2003. Hindlimb unloading alters ligament healing. *Journal of Applied Physiology* 94, 314–324. 91, 142
- Reynolds, O., 1903. Papers on mechanical and physical subjects—The sub-mechanics of the universe, Collected works. Vol. 3. Cambridge University Press. 145
- Rief, M., Oesterhelt, F., Heymann, B., Gaub, H. E., 1997. Single Molecule Force Spectroscopy on Polysaccharides by Atomic Force Microscopy. *Science* 275, 1295–1297. 30
- Sarrate, J., Huerta, A., Donea, J., 2001. Arbitrary Lagrangian-Eulerian formulation for fluid-rigid body interaction. *Computer Methods in Applied Mechanics and Engineering* 190 (24–25), 3171–3188. 101
- Sengers, B. G., Oomens, C. W. J., Baaijens, F. P. T., 2004. An integrated finite-element approach to mechanics, transport and biosynthesis in tissue engineering. *J. Bio. Mech. Engrg.* 126, 82–91. 39
- Simo, J. C., 1987. On a fully three-dimensional finite-strain viscoelastic damage model: Formulation and computational aspects. *Computer Methods in Applied Mechanics and Engineering* 60 (2), 153 – 173. 89
- Simo, J. C., Hughes, T. J. R., 1998. *Computational Inelasticity*. Springer Verlag. 89
- Simo, J. C., Taylor, R. L., Pister, K. S., 1985. Variational and projection methods for the volume constraint in finite deformation elasto-plasticity. *Comp. Methods in Applied Mech. Engrg.* 51, 177–208. 49
- Skalak, R. W., 1981. Growth as a finite displacement field. In: Carlson, D. E., Shields, R. T. (Eds.), *Proceedings of the IUTAM Symposium on Finite Elasticity*. Martinus Nijhoff, The Hague, Boston, London, pp. 347–355. 2, 20
- Skalak, R. W., Zargaryan, S., Jain, R. K., Netti, P. A., Hoger, A., 1996. Compatibility and the genesis of residual stress by volumetric growth. *J. Math. Bio.* 34, 889–914. 2, 20
- Spilker, R., Suh, J.-K., 1990. Formulation and evaluation of a finite element model for the biphasic model of hydrated soft tissues. Vol. 35. pp. 425–39. 101
- Sun, Y.-L., Luo, Z.-P., Fertala, A., An, K.-N., 2002. Direct quantification of the flexibility of type I collagen monomer. *Biochemical and Biophysical Research Communications* 295, 382–386. 30
- Swartz, M., Kaipainen, A., Netti, P. E., Brekken, C., Boucher, Y., Grodzinsky, A. J., Jain, R. K., 1999. Mechanics of interstitial-lymphatic fluid transport:

- Theoretical foundation and experimental validation. *J. Bio. Mech.* 32, 1297–1307. 35, 113
- Taber, L. A., Humphrey, J. D., 2001. Stress-modulated growth, residual stress and vascular heterogeneity. *J. Bio. Mech. Engrg.* 123, 528–535. 2, 4, 20
- Taylor, R. L., September 1999. FEAP - A Finite Element Analysis Program. University of California at Berkeley, Berkeley, CA. 48
- Tezduyar, T., Sathe, S., 2003. Stabilization parameters in SUPG and PSPG formulations. *Journal of Computational and Applied Mechanics* 4, 71–88. 149
- Truesdell, C. A., Noll, W., 1965. *The Non-linear Field Theories (Handbuch der Physik, band III)*. Springer, Berlin. 1, 11, 14, 20, 76, 148
- Truesdell, C. A., Toupin, R. A., 1960. *The Classical Field Theories (Handbuch der Physik, band III/1)*. Springer-Verlag, Berlin. 1, 27, 72, 73, 75, 79, 82, 84
- Wolff, J., 1892. *Das Gesetz der Transformation der Knochen*. English translation by P. Maquet and R. Furlong. Belin, Springer-verlag, 1986. 91
- Zienkiewicz, O. C., Taylor, R. L., 1989. *The Finite Element Method: Vol I and II*. McGraw-Hill, London, New York. 99